Stochastic Reconstruction and Morphological Studies of Catalyst Layers of Proton Exchange Membrane Fuel Cells

by

Yixiang Zhang

A thesis
presented to the University of Waterloo
in fulfillment of the
thesis requirement for the degree of
Master of Applied Science
in
Mechanical and Mechatronics Engineering

Waterloo, Ontario, Canada, 2021

Author's Declaration

I hereby declare that I am the sole author of this thesis. This is a true copy of the thesis, including any required final revisions, as accepted by my examiners.

I understand that my thesis may be made electronically available to the public.

Abstract

The microstructure of the CL has a significant impact on the performance, durability and cost of the PEM fuel cells. The CL is a complex and heterogeneous porous material consisting of carbon-supported catalyst, ionomer and pore. An ideal CL microstructure should provide good gas diffusion, water removal, protonic and electronic transport, and close contact for the three-phase boundaries where electrochemical reaction takes place. However, during fuel cell operation, the structure deteriorates, and the performance degrades. The CL microstructure degradation mechanism is still not clear, and the optimal CL structure is unknown.

In order to understand the CL microstructure, extensive studies need to be conducted iteratively on numerous samples to find the optimal microstructure. The utilization of experimental imaging methods like FIB-SEM and X-ray CT offers a realistic microstructure but a trade-off of expensive cost and time, making it impractical for the iterative design process. Therefore, statistical reconstruction of microstructure has become a useful tool to reconstruct the CL microstructure based on statistical information extracted from experimental images in practical time and funding. Additionally, due to the lack of experimental means in examining the CL microstructure real-time during fuel cell operation, it is still unclear how the CL morphology evolves during the fuel cell operation under vehicle.

The objective of this thesis research are (i) to develop an algorithm to reconstruct CL, (ii) to numerically study the CL morphological changes during dynamic fuel cell operation under vehicle driving profile, (iii) to investigate how the CL morphology evolves after cyclic loading.

In the present thesis research, a hybrid CL reconstruction method has been developed and programmed to reconstruct the CL microstructure based on statistical information in experimental images. The statistical correlation functions employed to characterize the experimental images are the two-point correlation function and lineal path function, which are closely related to specific surface area and cluster size in the porous media and to estimate transport properties such as permeability and diffusion coefficient. Then, a three-dimensional numerical model has been developed with the reconstructed geometry to study the morphology variations under different driving profiles. The main features of the numerical models are the inclusion of CZM for interface delamination and the temperature and humidity-dependent viscoplastic material properties. The governing equations are described and solved using a FEM based software, ANSYS Mechanical.

The reconstruction methods are validated against existing analytical solution and the fracture model and viscoplastic model used in the numerical model are validated against experimental solution where good agreements are observed. Subsequently, the numerical

model based on the reconstructed CL structure is developed to investigate the CL morphological evolution under different dynamic fuel cell cyclic operating conditions. The effects of hygrothermal amplitude, fuel cell start-up/shutdown frequency, driving duration and parking length are investigated. It is summarized that (1) the outer regions of the agglomerate where not mechanically supported by other agglomerates are more susceptible to delamination; (2) the agglomerate surface dip where the surface concaves in is more resistant to being damaged; (3) the region where multiple agglomerate surfaces intersect shows better resistance to delamination. Two main structural changes in CL are observed: (i) the ionomer thickening due to the plastic strain accumulation in the ionomer, and (ii) the delamination at the interface between the ionomer and the catalyst agglomerate. A competition has been observed between the ionomer's yield failure and the ionomer/catalyst-agglomerate interface failure. The findings in the thesis research provide insights into CL mechanical degradation mechanism and hence allow the development of methods to the durability of the PEM fuel cells.

Acknowledgements

First and foremost, I would like to express my gratitude to my supervisor Dr. Xianguo Li for his guidance, support, and encouragement throughout my MASc degree. I have had a great opportunity to learn from him about all facets of life. His passion for learning and research is something i hope to acquire myself. Be it the problems in numerical modelling, dealing with work crisis or review of my writings, he has always been very understanding and helpful. Our discussions on technical subjects and on life will be always appreciated in my life.

A sincere thanks to Dr. Jian Zhao and Dr. Song Yang for giving me inspirations on my thesis work and numerous discussions on the technical subjects. Further, I would like to thank Dr. Huiyuan Liu for her patience in teaching me experimental methods that I am not familiar with.

Furthermore, I would like to thank my parents and friends whose support helped me get through the last leg of this journey amidst the COVID-19 pandemic.

Table of Contents

List of Figures

List of Tables

List of Abbreviations

BOL beginning of life 6

CL catalyst layer iii, 2, 13, 19, 37, 38, 44, 45, 92

CSM Computational Solid Mechanics 84

CT Computer Tomography iii, 6, 12

CZM Cohesive Zone Method iii, 92

EOL end of life 6

FEM Finite Element Method iii, 45, 84, 87–89, 91, 120

FIB-SEM Focused Ion Beam Scanning Electron Microscopy iii, 12

FVM Finite Volume Method 15, 120

GDL gas diffusion layer 2

HOR hydrogen oxidation reaction 2

LBM Lattice Boltzmann Method 15, 45

ORR oxygen reduction reaction 3

PEM proton exchange membrane iii, 1, 2, 19

RMS Root Mean Square 90

RMSE Root Mean Square Error 90

RVE Representative Volume Element 69, 70

SA Simulated Annealing 55, 57, 58

TPBs Triple-Phase Boundaries 4

ULM Updated Lagrangian Method 84, 86, 88, 91

Chapter 1

Introduction

1.1 Background

Considering the prevailing energy crisis and increasing global carbon emissions, the soaring demand for clean alternative power sources for stationary, vehicular and portable application put fuel cell under the spotlight. A fuel cell is an energy conversion device converting the chemical energy in fuels and oxidants into electricity directly. PEM fuel cells are one major fuel cell type which primarily uses hydrogen as fuel and features a proton-conducting polymer electrolyte membrane [1]. The PEM fuel cells are more energy efficient thanks to the high power density of hydrogen and do not generate greenhouse gas emissions [2]. In recent years, PEM fuel cells receive enormous attention in vehicular application, especially in commercial vehicles including buses [3] and trucks [4] because they provide the scalability for minimized increased weight, fast fueling and longer range, when compared to battery electric vehicles.

However, the performance (power density), high cost and long term durability are the

main obstacles for the commercialization of PEM fuel cells and fuel cells development is also restricted by hydrogen production, storage and distribution and proper hydrogen infrastructure network [5,6]. This research is motivated by the commercialization of PEM fuel cells.

1.2 Principle of PEM Fuel Cells

The key components of a PEM fuel cell stack consists of a solid polymer membrane, two electrodes, two flow channels and two distribution plates as illustrated in **Fig. 1.1**. Each electrode consists of a GDL and a CL where electrochemical reaction takes place. At the anode side, hydrogen gas is pumped into the flow channels and then diffuse to the anode CL through GDL. At the anode CL, hydrogen is catalytically split into protons (or hydrogen ions) and electrons. The protons permeates through hydrated PEM to the cathode CL while electrons are rejected by high electronic resistance membrane to force to travel through an external circuit to the cathode side, thus powering external load. Simultaneously, oxygen gas is supplied to the cathode CL in a similar fashion. At the cathode CL, the oxygen molecules reacts with the protons just travelled through the PEM and the electrons coming from the external circuit to form water molecules.

At the anode side, the electrochemical reaction where hydrogen molecule spilt into protons and electrons is called the HOR or anode half-cell reaction is represented by

$$\mathrm{H_2} \longrightarrow 2\,\mathrm{H^+} + 2\,\mathrm{e^-}$$

At the cathode side, the electrochemical reaction where protons, electrons and oxygen molecules are combined to form water is called the ORR or cathode half-cell reaction is shown below

$$\frac{1}{2}O_2 + 2\,H^+ + 2\,e^- \longrightarrow H_2O$$

As a result, the overall reaction is obtained by summing up the two half-cell reactions represented below

$$H_2 + \frac{1}{2}O_2 \longrightarrow H_2O + \text{Waste Heat} + \text{Electricity}$$

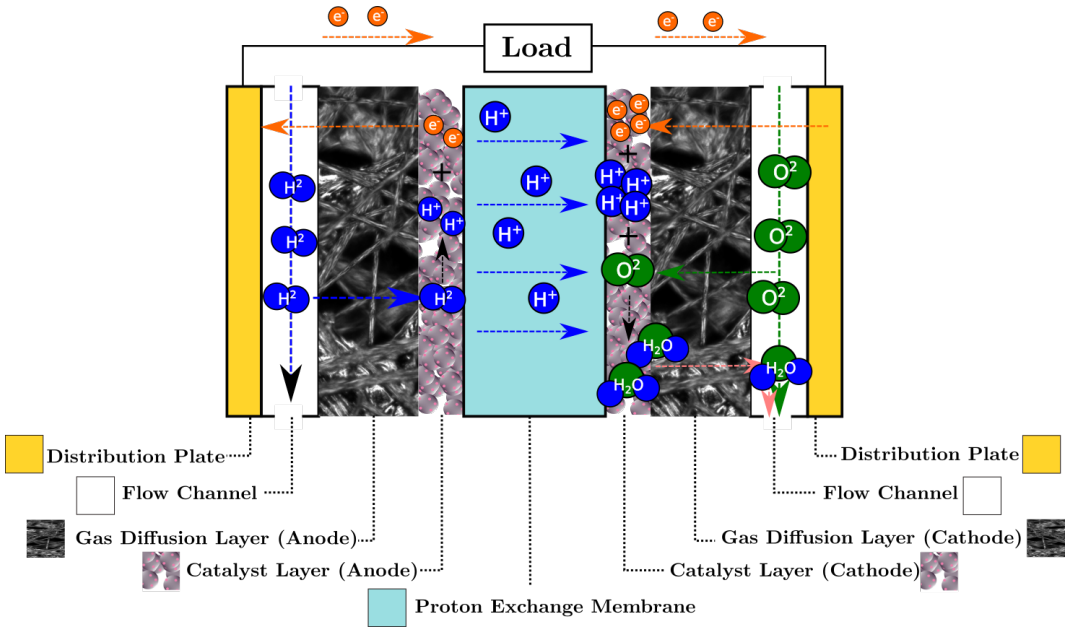

Fig. 1.1: Schematic of a PEM fuel cell unit with principal components identified.

At the cathode CL, water is generated during ORR at the reaction sites and permeates through the cathode GDL into flow channel. In the fuel cell literature, these reaction sites

are typically called TPBs. The TPBs are the interface of the ion conductor (electrolyte), the electron conductor (Pt/C) and the pore providing gaseous fuel molecules. The good contacts at TPBs are strongly correlated with the reaction rate and performance of fuel cell. Therefore, the understanding of CL microstructure and study of its degradation mechanism is extremely pivotal in improving both performance and durability.

1.3 Catalyst Layers of PEM Fuel Cells

The catalyst layer of the PEM fuel cells is a key component as it contains the reaction sites for electrochemical reactions to take place, transfers electrons and protons and provides a pathway for reactant gas supply and product water removal via pore [1, 7–9].

The most popular CL is composed of the carbon-supported catalyst (e.g., Pt/C), the ionomer (e.g., Nafion), and the pore phase. Catalyst used in PEM fuel cells includes platinum, and platinum alloys and other materials such as cobalt and nickle have been implemented in many works. However, platinum still remains the most popular material since it provides the best combination of oxygen binding energy and maximal activity according to Sabatier principle [10]. Since catalysts are often extremely expensive, they are typically decorated onto a high-surface-area supporting materials such as Vulcan XC-72, carbon nanotubes and Ketjan black [11]. The supporting carbon material provides an inexpensive, stable, corrosion-resistant, and electrically conductive porous support structure. Electrolyte material, such as the Nafion, is added to bind carbon-supported catalyst and to provide a protonic pathway for protons to reach reaction sites, namely, TPBs. As shown schematically in **Fig. 1.2**, the electrochemical reactions only take place where electrolyte,

gas, and electrically connected catalyst regions are in contact. In the cathode CL, the carbon-supported catalyst forms agglomerates covered with the ionomer, which is a thin film with a thickness of only a few nanometers [12].

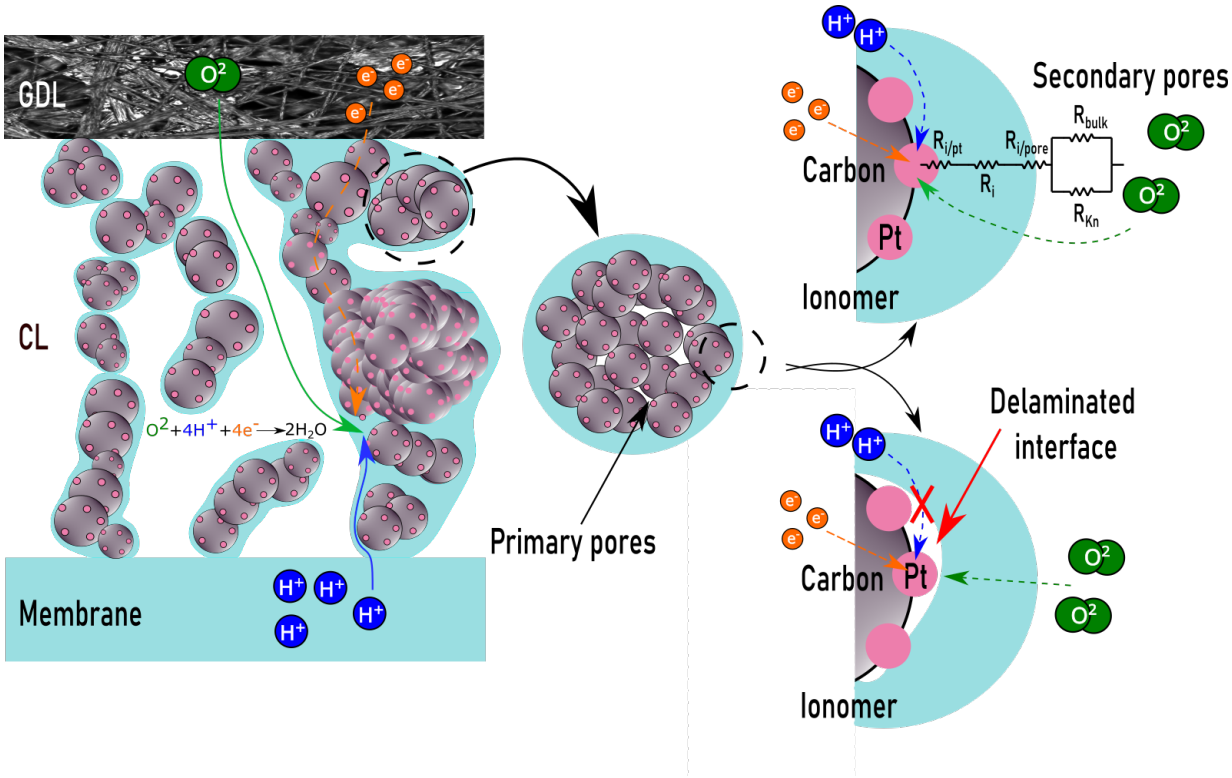

Fig. 1.2: (Left) Schematic of the reactant transport in the cathode catalyst layer; (Center) Zoomed image of the catalyst agglomerate covered by ionomer thin film; (Right) Schematic of O_2 mass transport resistance network of undamaged and delaminated ionomer.

Catalyst Layer Morphology Variations

For a successful cathode half-cell reaction, protons and electrons are required to arrive at the Pt surface via the ionomer network and carbon support to the Pt surface, respectively. Therefore, it is of importance to enhance the proton transfer and oxygen permeation in

the ionomer for better performance. During dynamic fuel cell operation, the catalyst layer microstructure deteriorates. One of the degradation mechanisms is the ionomer thin film is delaminated and peeled away from the catalyst agglomerate during the cyclic loading conditions [13–15]. As illustrated in **Fig. 1.2**, the interface delamination may completely cut off the protonic access to the Pt, and hence performance degrades. The non-uniformity and discontinuity of ionomer coverage on carbon-supported platinum catalysts leads to poor performance [16]. In addition to interface delamination, Pokhrel *et al.* investigates the failure analysis of catalyst layer via X-ray CT and observes that the ionomer phase morphs from a thin film structure at the BOL to a dense structure at the EOL [17]. In their study, the ionomer volume fraction in CL increases in volume fraction from 21 % at BOL to 51 % at EOL while the pore space volume decreases from 54 % to 23 %. The increased ionomer volume fraction at EOL is the result of plastic strain accumulation as the water molecules are trapped in the side groups of the ionomer. The observed morphological variations drastically influences the oxygen permeation in solid ionomer to the Pt reaction sites and oxygen diffusion in secondary pore.

Oxygen O_2 molecules travel via secondary pore, dissolve at ionomer/pore interface, diffuse in the ionomer thin film, and arrive at Pt catalyst surface in the cathode CL. As shown in **Fig. 1.3a**, resistance network theory is often used to characterize the transport process. The effective gas-phase transport resistance ($R_{\text{eff,pore}}$) consists of bulk diffusion resistance (R_{bulk}) and Knudsen diffusion (R_{Kn}) obeying Fick's law. The solid phase transport includes resistance at the interface between the ionomer and pores ($R_{\text{i/pores}}$), the ionomer thin film (R_i), and the interface between the Pt and ionomer ($R_{\text{i/pt}}$). As illustrated in **Fig. 1.3b**, the degraded ionomer with a higher volume fraction at EOL leads

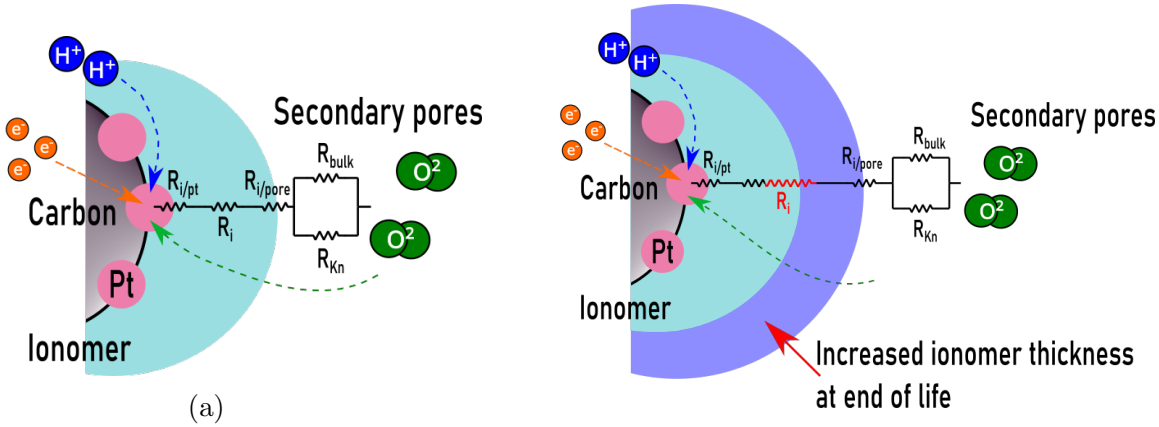

Fig. 1.3: Schematic of resistance network for O_2 transport in cathode catalyst layer at (a) beginning of life; (b) end of life.

to increased diffusion resistance in the solid ionomer (R_i), and hence deteriorates the fuel cell performance. Moreover, the ionomer expansion leads to decreased porosity and causes increased resistance in effective gas-phase transport resistance ($R_{\text{eff,pore}}$). Although both the interface delamination and ionomer expansion degenerate the fuel cell performance, the detailed mechanism on how the CL structural degrades is still not clear. Due to the limitation in experimental apparatus to measure the CL structural variations in real-time during operation, numerical modelling becomes a valuable tool to provide insight into the CL morphological variations under fuel cell dynamic operation. Therefore, a numerical study on CL morphology variations has been conducted to explore the CL structural degradation.

Catalyst Layer Reconstruction

To analyze the morphological variations in CL, an accurate representation of CL microstructure is necessary. In fuel cell literature, CL reconstruction is summarized into

experimental reconstruction and statistical reconstruction. Despite high accuracy, the experimental method's high cost, limited spatial resolution and long time prohibit iterative CL design, including many different fabrication conditions and catalyst layer composition. Hence, it is more practical to employ statistical reconstruction, sub-categorizing into image-based reconstruction and fabrication-based reconstruction. The image-based reconstruction extracts the statistical information from the experimental images. An energy minimization method is often employed to randomly swap the voxels in the reconstructed structure until the difference in statistical information from the experimental images and the reconstructed structure is less than a tolerance value. The fabrication method is generally based on the classic randomly packed spheres model with carbon particles idealized as spheres, platinum uniformly dispersed on the perimeter of carbon sphere, and ionomer assumed to be uniformly covering the carbon-supported platinum. It typically reconstructs the CL based on the order of the fabrication process by seeding the carbon spheres, dispersing the platinum and binding with the ionomer. Different catalyst ink compositions are used to calculate the volume fraction of each phase for the fabrication-based method. The image-based reconstruction offers accurate microstructure reconstruction, but the reconstructed geometry consists of isolated voxel and sharp edges, leading to stress singularity and difficulty in convergence in numerical modelling. The fabrication-based method is easy to implement, but the only statistical information it contains is the volume fraction, which is inadequate to statistically characterize CL microstructure. Therefore, a hybrid reconstruction method is developed to reconstruct an accurate representation of CL based on a randomly penetrable sphere model and statistical information from experimental images. Subsequently, the reconstructed CL is adopted for the delamination model to study the

morphology variation.

1.4 Objectives and Scope of the Thesis

The scope of the thesis research is shown in **Fig. 1.4**. The objective of this thesis research are (i) to develop an algorithm to reconstruct catalyst layer, (ii) to numerically study the CL morphological changes during dynamic fuel cell operation during vehicle driving profile, (iii) to investigate how the CL morphology evolves after cyclic loading.

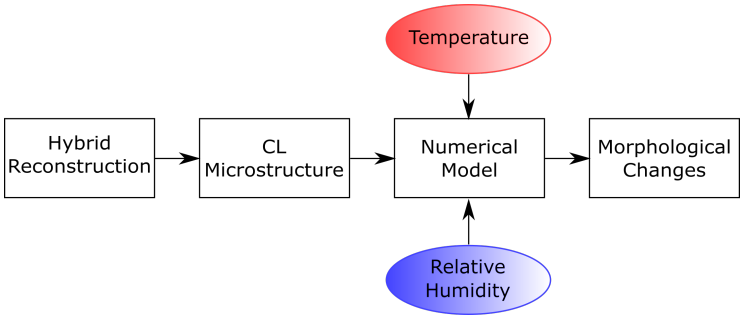

Fig. 1.4: Objectives and scopes of the thesis work.

The thesis is divided into six chapters. The first chapter presents an introduction to the research problem, background information, working principles of PEM fuel cells and CLs, and objective and scope are presented. In chapter 2, a literature review of experimental and numerical studies on CL reconstruction and catalyst layer delamination are presented. Chapter 3 presents the sphere-based CL reconstruction methodology and implementation and its results. Chapter 4 presents the model formulation for the study of morphological changes in CL. Chapter 5 presents the results for morphological changes in CL during dynamic driving cycles. Last but not least, Chapter 6 summarizes the contributions of this

work and recommendation for future work.

Chapter 2

Literature Review

In this chapter, a comprehensive literature review is conducted with an emphasis on (i) catalyst layer reconstruction, and (ii) the catalyst layer degradation.

2.1 Catalyst Layer Reconstruction

A good understanding of the microstructure of CL is essential for estimating macro-properties, structure operational degradation to evaluate the fuel cell performance. As illustrated in **Fig. 2.1**, various approaches have been conducted to reconstruct CL. The following section discusses the methodologies in CL reconstruction in the fuel cell literature.

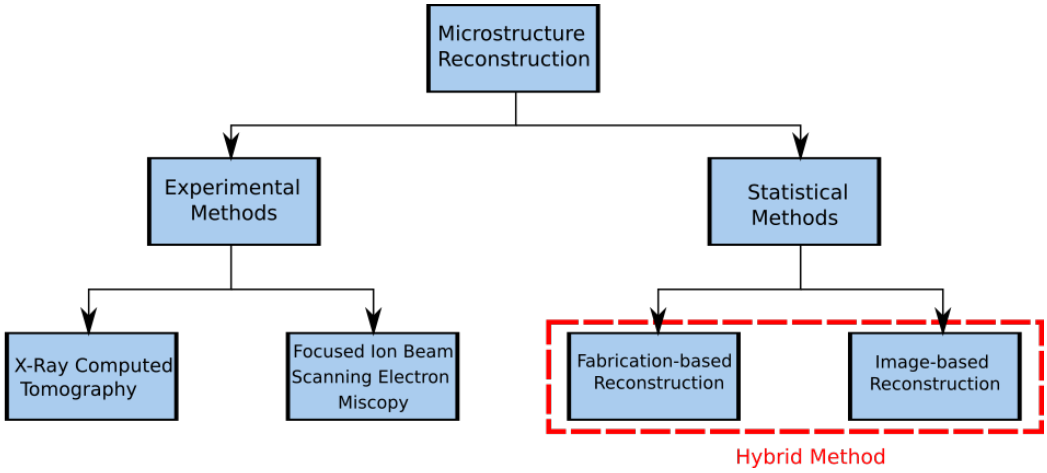

Fig. 2.1: Schematic summary of microstructure reconstruction method.

2.1.1 Experimental Imgaing Techniques

Experimental techniques to characterize and reconstruct CL typically is 3D imaging-based techniques, such as FIB-SEM [18–24], or X-ray CT [25–28].

FIB-SEM is a new approach to investigate and analyze the three-dimensional internal microstructures due to their good performance. The FIB is used for milling the sample material serially, and SEM is responsible for the exposed cross-sectional area of the sample. FIB and SEM beams typically have a coincident angle of 52° to 54°. Then those cross-sections are merged into a three-dimensional structure. FIB-SEM is an invasive technique with a resolution of up to 1 nm in the imaging plane and 10-20 nm in the slicing direction. Its limitation includes the inability to separate the ionomer and carbon phases, 2D/3D distribution of phases, etc [19].

The X-ray CT is a non-invasive technique and has recently shown a bright future for analyzing CL due to its ability to separate different phases [26, 29]. The sample is imaged

from various angles, and projections of the structure in a different plane are generated. Those projections are combined using a computational tomographic reconstruction algorithm to acquire a three-dimensional structure. Conventional Micro-CT has a resolution of around 1 μm, which is not sufficient to resolve the nanoscale morphology of CL. More recent nano-CT has a resolution around 10 nm which provides valuable insights on the size and shape of the CL agglomerates but unfortunately do not resolve features like smaller pores within the agglomerates.

Overall, the experimental methods offer a relatively realistic 3D reconstruction of the structure, but those methods are costly and time-consuming, making it very impractical to perform extensive parametric studies for the CL optimization process.

2.1.2 Fabrication-based Reconstruction

To extensively investigate, manipulate and then optimize the catalyst layer structure, many works focused on the mathematical reconstruction of the CL. One of the most popular approaches in literature is to simulate the reconstruction based on the fabrication process due to its simplicity and robustness [30–36]. Typically, the CL consists of carbon, platinum and ionomer with a proper composition such as Pt loading, Pt/C and Nafion wt.%. Based on the composition information, the volume fraction of each phase is derived as the convergence criteria for the fabrication-based reconstruction methods. The carbon is idealized as spheres and randomly generated until the carbon volume fraction has been met. Then Platinum and Nafion are deposited on carbons to reach satisfied volume fraction to obtain the final structure [30, 32]. Moreover, some spherical agglomerate surrogate model

has been incorporated in the reconstruction process to simulate the aggregation mechanics in ink preparation [34]. In these studies, the reconstructed geometry is generally validated against the pore size distribution of the CL [35, 36].

Despite the popularity of fabrication-based reconstruction method, this methods are not able to capture all the processes of fabrication. The catalyst layer structure is heavily dependent on its fabrication process including mixing, ultrasonic treatment, coating, drying process [37]. The physics of some of fabrication process is neither well understood not modelled in fabrication-based methods which makes the reconstructed structure susceptible. Additionally, the detailed validation against the pore size distribution is rarely reported in the literature and typically involves many parameter tuning resulting in the parameterization of reconstruction process extremely cumbersome.

2.1.3 Image-based Reconstruction

As previously mentioned in **section 2.1.1**, the advancement in imaging techniques offers a more realistic 3D microstructure of the CL, typically costly and time-consuming, making it impractical to extensively explore CL structure in the engineering design process. A more popular way is to characterize the experimental CL images statistically and then stochastically reconstruct a new CL structure that shares the same statistical information with experimental images. Those functions that characterize microstructure are referred to as microstructural correlation function such as two-point correlation function [38], surface correlation function [39], lineal-path function [40], chord length function [41], etc. More information on the correlation function used in the statistical characterization of the porous

medium is available in **section 3.1**.

The image-based reconstruction method extracts the statistical information from 2D or 3D digitized images as a reference state. Voxels are randomly generated until the number of voxels in each phase is the same as those in experimental images. Subsequently, an energy function is defined to quantifies the difference between statistical information of the reference structure and the trial structure. The reconstruction problem turned into an optimization problem to minimize the energy function by randomly swapping the location of voxels in two difference phases. Many different approaches to minimize the energy function has been proposed to reconstruct porous medium, such as filtered gaussian fields [42–44], simulated annealing [45–47] and more recently generative adversarial networks [48, 49]. Those approaches continue to swap the voxel until the difference in statistical information between the image and reconstructed structure (namely energy) is below a tolerance value (convergence criteria).

Although the image-based reconstruction provides reasonable CL microstructure, it suffers from high computational cost compared with fabrication-based method. Some hybrid method has been proposed to combine the merits of both methods [45, 50]. Additionally, there are few studies that focus on using multiple statistical correlation functions to reconstruct the CL [44, 51]. Furthermore, the majority of the reconstruction work has been focused on the accuracy of the void phase during reconstruction because their research focuses on transport phenomena using FVM or LBM requiring the accuracy of the pore phase structure. In this thesis research, a hybrid reconstruction method has been developed and programmed to reconstruct the CL microstructure with an emphasis on solid-phase reconstruction by multiple statistical correlation functions to study the morphological variations

under cyclic loading.

2.1.4 Summary

A summary of some of the most representative research conducted in the CL reconstruction is listed in **Table. 2.1** in chronological order. Among those methods discussed above, experimental reconstruction methods like FIB/SEM and X-ray nano CT offer realistic CL microstructure but are too expensive and time-consuming for conducting parametric studies on CL optimization. The fabrication-based reconstruction method is simple and easy to implement, but reconstructed CL only contains low-order statistical information like volume fraction of different phases. The image-based reconstruction method generates CL microstructure containing high-order statistical information, but the voxelized structure has sharp edges and dead voxel, leading to stress singularity and convergence issues. The hybrid reconstruction method proposed and developed in the present study uses a collection of spheres instead of voxels to ensure smooth edge for subsequent modelling work and generate high accuracy reconstructed CL microstructure containing high-order statistical information like the two-point correlation function and lineal path function.

2.2 Catalyst Layer Degradation

Poor durability is one of the main obstacles in the commercialization of PEM fuel cells. Despite inevitable fuel cell performance degradation, an improved understanding of damage initiation and propagation mechanisms could be employed to constructively control and

Table 2.1: A summary of representative CL reconstruction method in fuel cell literature.

Authors	Reconstruction Method	Data Source	Stat. Info	Ref.
2006 Mukherjee et al.	Filtered Gaussian Fields	2D TEM	Normalized S_2	[43]
2008 Hattori et al.	Fabrication based	Catalyst Composition	ϕ	[30]
2009 Kim et al.	Simulated Annealing	Analytical for overlapping disks	S_2	[45]
2010 Siddique et al.	Fabrication based	Catalyst Composition	ϕ	[32]
2012 Epting et al.	X-ray nano CT	-	-	[29]
2014 Singh et al.	Simulated Annealing	FIB/SEM	S_2	[19]
2015 Pant et al.	Simulated Annealing	2D SEM	S_2, L, C	[51]
2015 Gao et al.	FIB-SEM	-	-	[23]
2016 Inoue et al.	FIB-SEM	-	-	[24]
2021 Hou et al.	Fabrication based	Catalyst Composition	ϕ	[36]
Present study	Hybrid Method	3D CL Microstructure	S_2, L	-

Note: ϕ the volume fraction, S_2 the two-point correlation function, L the lineal path function and C the chord length function. Details on those statistical correlation functions is available in the next chapter.

mitigate the degradation rate to improve long-term durability. The exact degradation mechanism in PEM fuel cells remains unknown, but the deterioration in the fuel cell is a result of interconnected chemical and mechanical degradation, as schematically shown in **Fig. 2.2**.

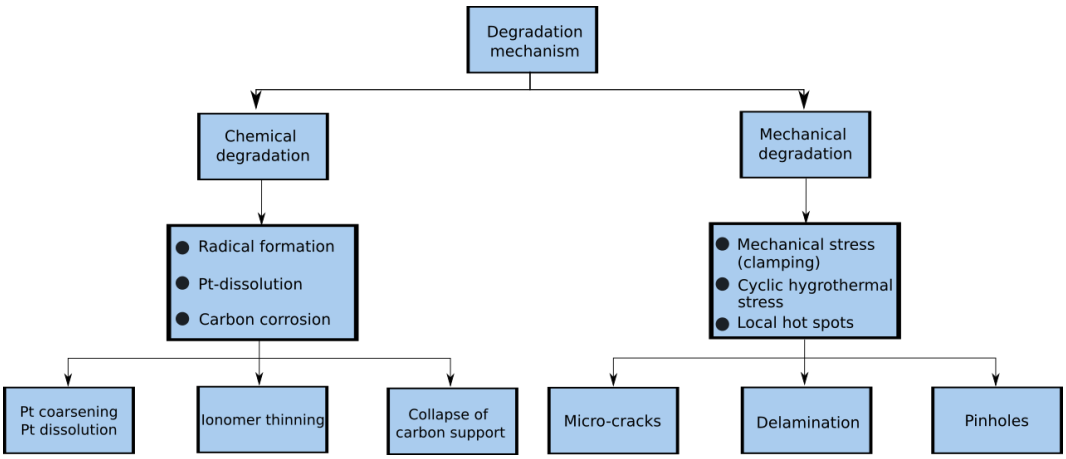

Fig. 2.2: Schematic summary of degradation mechanism in CL.

2.2.1 Chemical Degradation

Chemical degradation is a complicated process, and many researchers have found out that chemical degradation plays a vital role in performance loss [52, 53]. The formation of radicals such as peroxide ($HO\cdot$) and hydroperoxide ($HOO\cdot$) induces many undesirable electrochemical reactions, leading to the degradation of the ionomer molecular structure in both the membrane and CL [54]. There are still debates over whether the degradation initially begins at the anode side and migrates towards the cathode side [55,56] or the other way around [57,58]. The radical is produced by two different pathways including formation of hydrogen peroxide H_2O_2 as intermediate species and a direct reaction of H_2 and O_2 at the platinum surface. The hydrogen peroxide formation mechanism is illustrated in **Fig. 2.3**. The incomplete reaction between electrons and hydrogen protons forms hydrogen peroxide. Hydrogen peroxide formation via a two-electron reduction of oxygen is shown below,

$$\mathrm{O_2 + 2\,H^+ + 2\,e^- \longrightarrow H_2O_2} \qquad E_0 = 0.695\,V\ vs.\ V_{\mathrm{RHE}}$$

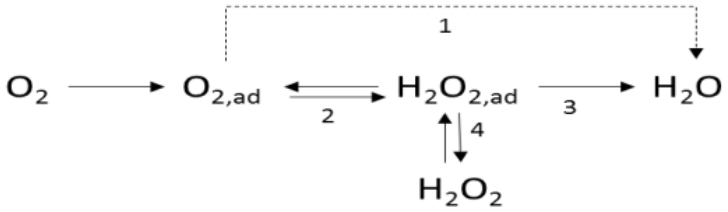

Fig. 2.3: Hydrogen peroxide formation mechanism.

Hydrogen peroxide H_2O_2 has a longer lifetime than radicals. It may detach from Pt surface, diffuse far from its formation sites and decompose into radicals in the presence of transition metal cation or heat. The radicals that attack the ionomer end-groups are

widely accepted as the source of ionomer degradation mechanisms [59], leading to ionomer thinning [60].

Platinum dissolution and carbon corrosion are considered the primary chemical degradation mechanism [61] leading to a series of secondary chemical degradation mechanisms, including Ostwald ripening [62], particle migration and agglomeration [63], and detachment of catalyst particles [64]. The dissolved platinum even catalyzes the carbon corrosion reaction and aggravates the degradation rate [65]. Cathode carbon support degradation is one of the crucial factors for the reduced lifetime of PEM fuel cells. In an electrochemical environment, carbon corrosion proceeds by the following reaction [66]:

$$\mathrm{C} + 2\,\mathrm{H_2O} \longrightarrow \mathrm{CO_2} + 4\,\mathrm{H^+} + 4\,\mathrm{e^-} \qquad E_0 = 0.207\,V\ vs.\ V_{\mathrm{RHE}}$$

The above reaction indicates that the oxidation of carbon can occur when the cathode potential exceeds 0.207 V $vs\ V_{\mathrm{RHE}}$, leading to negligible carbon corrosion under operating conditions and considerable carbon corrosion under transient operating conditions, such as start-up/shutdown and local H_2 starvation [67]. The carbon corrosion leads to a severe loss of CL structural integrity and collapse of the support structure, reducing the porosity and increasing mass transport resistance [68].

2.2.2 Mechanical Degradation

While chemical degradation gradually deteriorates the catalyst coated membrane (CCM), mechanical degradation is responsible for irreversible physical damage including cracks, delamination and pinholes [15, 69, 70], as schematically shown in **Fig. 2.4**.

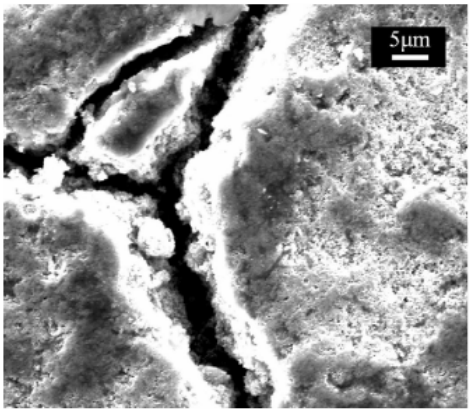

(a) Cracks [15].

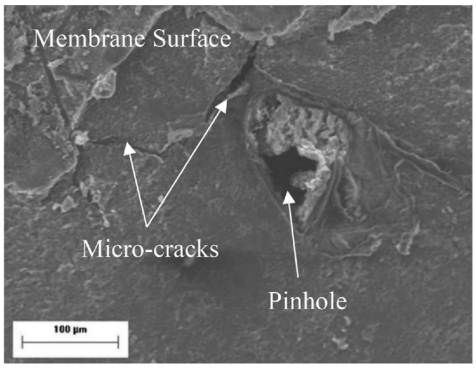

(b) Pinhole and microcracks [69].

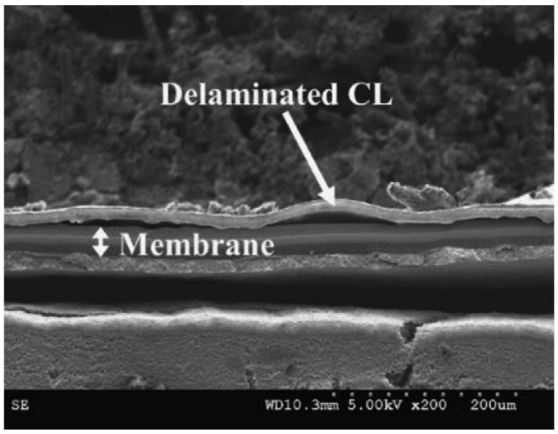

(c) Interface delamination [70].

Fig. 2.4: Mechanical degradation modes of the catalyst layer (a) crack formation; (b) pinhole; (c) delamination.

The cracks in the CL increase the CL resistance, aggravate the water flooding problem and lead to non-uniform current distribution. The pinholes lead to hydrogen crossover and cell voltage decay. Delamination may cause peeling of CL off the membrane leading to an increase in activation losses. It may also occur inside the CL leads to the breakage of the ionomer network. The impact of these mechanical degradation modes is summarized in **Table. 2.2**.

Table 2.2: Different types of degradation modes and its impact in fuel cell.

Degradation Mode	**Impact of degradation modes in fuel cell.**
Cracks [71]	• Increase resistance in the CL • Aggravate water flooding • Non-uniform current distribution
Pinhole [69]	• Hydrogen crossover causing hot spots • Cell voltage decay • Instant electrode short-circuits
Delamination [70]	• Increase in activation losses • Peel off CL • Break ionomer network in CL

While a series of complex chemical and mechanical degradation is responsible for pinholes formation, the combined effect of mechanical stress like clamping stress and cyclic hygrothermal stress is the root cause for crack and delamination. The clamping stress is initially applied to ensure good electrical contact between the fuel cell components. The cyclic hygrothermal stress is induced by cyclic changes of relative humidity (RH) and temperature inside the catalyst layer. The combined mechanical stress causes the cyclic expansion and shrinkage of the ionomer in the CL, leading to crack formation, and the occurrence and growth of delamination.

Morphologies of the catalyst layer have a huge impact on performance degradation. Park *et al.* investigates the ionomer coverage on carbon black (CB)-supported Pt catalyst and graphitized carbon black (GCB)-supported Pt catalyst, as illustrated in **Fig. 2.5a** and **Fig. 2.5b**, respectively. They discover different carbon support has a significant impact on

ionomer coverage, closely related to performance loss. Park *et al.* conducts failure analysis on catalyst layer using X-ray CT and discovers that the volume fraction of ionomer phase increases from 21 % at BOL to 51 % at EOL, as shown in **Fig. 2.5c**. The nanoscale ionomer exhibits thickness-dependent proton conductivity and water uptake behavior [72]. Moreover, the increase in ionomer thickness also increases transport resistance for O_2 in the ionomer.

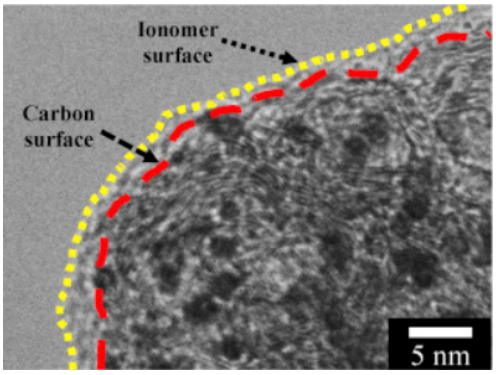

(a) C-Pt/CB [16].

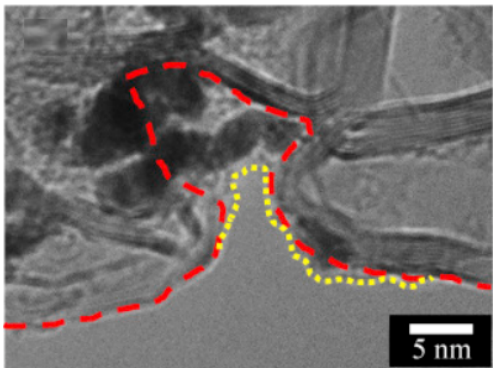

(b) C-Pt/GCB [16].

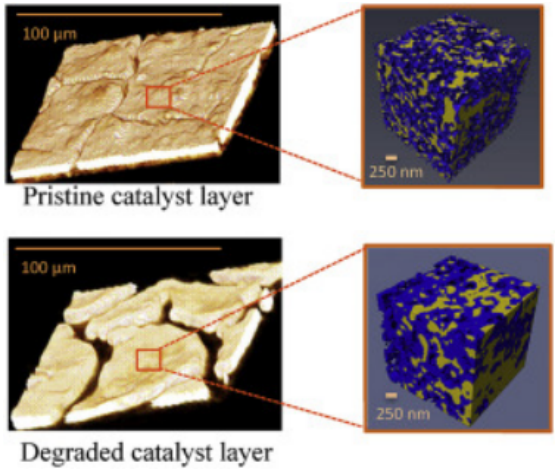

(c) Ionomer expansion [17].

Fig. 2.5: Morphologies of the ionomer covered on the carbon-supported Pt catalysts: (a) C-Pt/CB; (b) C-Pt/GCB. Morphological variation at the end of service life including (c) Cracked catalyst surface and ionomer volume expansion.

Experimental

An essential step towards understanding crack and delamination is first to understand the resistance to fracture of the CCM under different levels of hygrothermal loading conditions and loading direction. Although load for crack and delamination can be arbitrary, any stress state could be decomposed into a combination of three fundamental independent stress modes as schematically illustrated in **Fig. 2.6**.

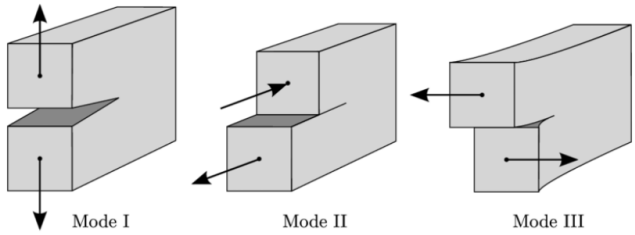

Fig. 2.6: Schematic of three fracture modes are defined: Tensile fracture (Mode I), in-plane shear fracture (Mode II) and out-of-plane shear fracture (Mode III).

Different material testing techniques have been developed and employed to characterize the catalyst-coat membrane's resistance to fracture in each mode including the double edge notch tension test [73, 74], trouser tear test [73, 75–77], knife slit test [73, 78] and double cantilever beam test [79]. Those works on fracture toughness are valuable and widely employed in simulation work.

Ex-situ experiments have also been done to investigate the effect of cyclic hygrothermal stresses on fuel cell crack formation and propagation. Jian *et al.* conducted wet-dry cycles on the catalyst layer and observed considerable growth of catalyst agglomerate and crack formation [80]. Chang *et al.* studied the effect of cyclic relative humidity and temperature, respectively and found out that cyclic relative humidity is the main driving force for crack

propagation, but combined hygrothermal cycles lead to the more severe crack. It is mainly because the high temperature and high relative humidity weaken the material strength of the ionomer [81].

Numerical

Modelling efforts have been made on simulating crack and delamination behaviour in the CCM, particularly under cyclic relative humidity and temperature. Banan *et al.* employed the finite element method (FEM) along with the cohesive zone model (CZM) to investigate the effect of hygrothermal cycling and vibration, respectively, on the in-plane membrane crack and interfacial delamination propagation in CCM [82–84]. Ding *et al.* proposed a node release algorithm in FEM to numerically studied the through-plane crack growth in fuel cell membrane [85]. Qin *et al.* studied the effect of crack location and fuel cell start-up time on delamination behavior [86]. In addition to the interfacial delamination between the CL and the membrane investigated above, delamination also occurs inside the CL where cyclic hygrothermal stresses separate the ionomer from the Pt/C agglomerate. A series of research studies have been conducted separately on investigating the interface delamination between the ionomer and catalyst agglomerate inside the catalyst layer [13, 15, 87] with a simplified 2D model. Rong *et al.* in a sequential work stochastically reconstructs a 2D CL of size 20 pixels by 20 pixels based on TEM image and found out the cyclic hygrothermal stress causes a decrease in the connection between different solid phases, which may indicate performance degradation [14].

2.2.3 Summary

A summary of modeling work on CL delamination is listed in **Table 2.3** in chronological order. Among these works, delamination propagation at the CL/Membrane interface has already been investigated under various fuel cell loading conditions. For delamination between different solid phases inside the CL, the understanding of how the interface delamination propagates between the ionomer and the agglomerate is preliminary examined for different representative or reconstructed two-dimension models. This present study is

Table 2.3: A summary of modelling work for CL delamination in fuel cell literature.

Authors	Scale	Geometry	Delamination Location	Ref.
2007 Rong et al.	Microscale	Assumed 2D	Ionomer/Agglomerate	[13]
2007 Rong et al.	Microscale	Reconstructed 2D	Ionomer/Agglomerate	[14]
2014 Banan et al.	Macroscale	Fuel Cell Stack 2D	In-plane CL/Membrane	[82–84]
2016 Ding et al.	Macroscale	Fuel Cell Stack 2D	Through-plane MEA	[85]
2018 Chang et al.	Microscale	Assumed 2D	Ionomer/Agglomerate	[15]
2021 Qin et al.	Macroscale	Fuel Cell Stack 2D	In-plane CL/Membrane	[86]
Present Study	Microscale	Reconstructed 3D	Ionomer/Agglomerate	-

focused on the development of a reconstruction method exhibiting statistical information of real experimental CL images and the development of a numerical model to investigate the microstructure changes between different phases in CL. The follow is the contribution of the present thesis research:

- Development of a hybrid reconstruction method based on simulated annealing to reconstruct the CL on top of the classic randomly packed spheres model but with the inclusion of multiple statistical correlation functions;
- Understanding the impact of dynamic driving conditions on CL microstructure changes

to improve the understanding of the mechanical degradation mechanism. Due to the lack of experimental means for investigating the CL microstructure variation during the fuel cell operation, the microstructure changes is studied numerically.

Chapter 3

Statistical Characterization and Reconstruction

This chapter is intended to describe the detailed reconstruction method and statistical functions used in this study.

3.1 Theory of Statistical Characterization

3.1.1 Indicator Functions

The indicator function is used to distinguish different phases in porous structure. A random media can have multiple phases i = 1,2,3,...n. For the catalyst layer, it consists of pore, carbon, ionomer and platinum. By grouping carbon, ionomer and platinum together into a solid phase, the catalyst layer is simplified to a binary state consisting of solid phase and

pore phase (i = solid, pore). Assuming that each phase i occupies a volume subset V_i of the total volume V, the indicator function for phase i is defined as [39]

$$I^{(i)}(x) = \begin{cases} 1, & \text{if } x \in V_i \\ 0, & \text{otherwise} \end{cases} \tag{3.1}$$

where superscript i means different phases, V_i means the volume subset occupied by phase i, x is a geometric point in this porous media.

Summing **Eq. 3.1** over solid and pore phase, the following equation is obtained

$$\sum_i I^{(i)}(x) = I^{(\text{solid})}(x) + I^{(\text{pore})}(x) = 1 \tag{3.2}$$

Eq. 3.2 simply means that each geometric point x must belongs to one certain phase. In this case, it would be either solid or pore phase. The addition of the probability of finding a solid phase and a pore phase at a given location x would be unity as follows

$$P\{I^{(\text{solid})}(x)\} + P\{I^{(\text{pore})}(x)\} = 1 \tag{3.3}$$

Knowing the exact structure of the catalyst layer is to know the indicator functions at each geometric point x of the random media. In the thesis, the catalyst layer used is digitized as a collection of pixels in 2D or voxels in 3D which is considered as the geometric point x. Therefore, knowing the indicator function for every pixel/voxel is to knowing the exact structure of the catalyst layer.

3.1.2 One-point Correlation Function

The one point correlation function is defined as the probability of finding a given phase at any given location x. The one-point correlation function for phase i is defined as

$$S_1^{(i)}(x) = P\{I^i(x)\} = \phi_i \tag{3.4}$$

where ϕ_i is the volume fraction of phase i.

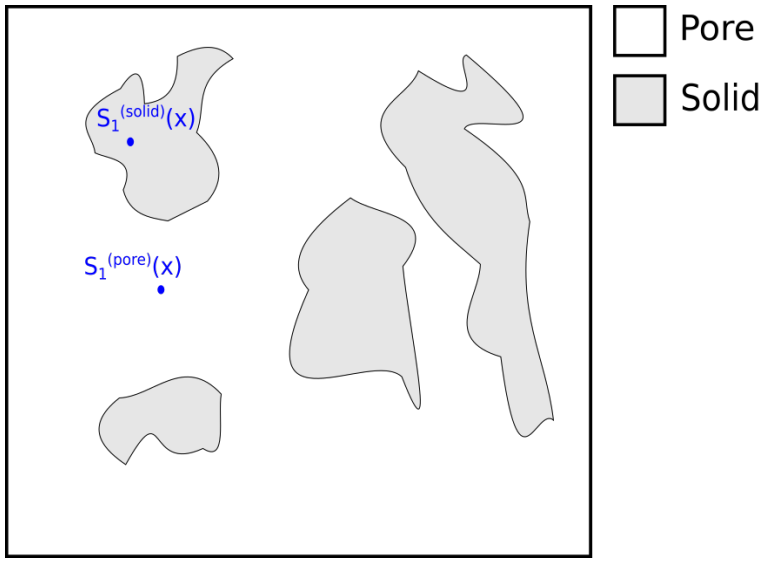

Fig. 3.1: A schematic showing instances of one-point correlation function (White phase is pore and grey phase is solid).

The one-point correlation function S_1 is the probability that a randomly sampled point in the media will be in the same phase as shown in **Fig. 3.1** and this probability is equivalent to ϕ_i, the volume fraction of phase i.

3.1.3 Two-point Correlation Function

The two-point correlation function S_2 is the probability of finding any two points x_1 and x_2 in the same phase i. For an isotropic and homogeneous media, a vector could be used to connect two points x_1 and x_2, i.e. $r = x_2 - x_1$. The two-point correlation function for phase i can be defined as

$$S_2^{(i)}(r) = P\{I^{(i)}(x_1) = 1, I^{(i)}(x_2) = 1\} \tag{3.5}$$

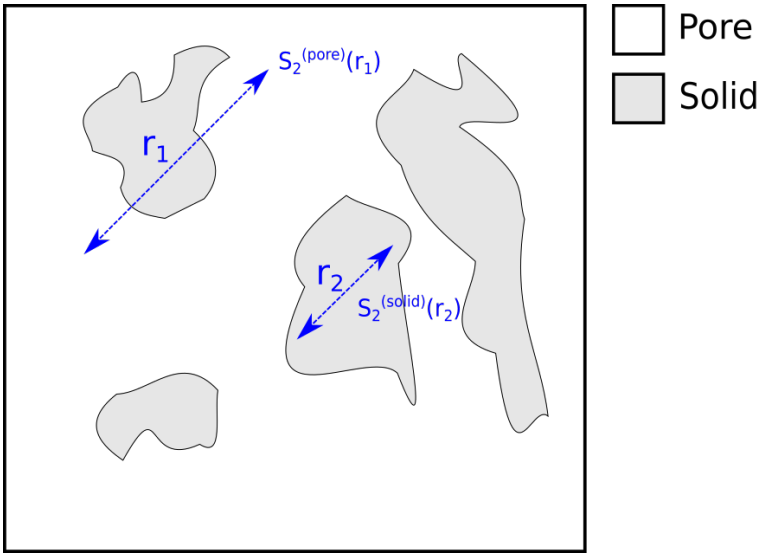

Fig. 3.2: A schematic showing instances of two-point correlation function in dashed blue lines with arrowheads (White phase is pore and grey phase is solid).

Fig. 3.2 illustrates two instances of two-point correlation function. $S_2^{\text{pore}}(r_1)$ and $S_2^{\text{solid}}(r_2)$ stand for the probability of finding end points of line segments r_1 and r_2 belonging to pore phase and solid phase, respectively.

The two point correlation function has the following asymptotic behavior in two-phase

medium when the length of line segment r approaches to zero and infinity [88]

$$\lim_{r\to 0} S_2^{(i)}(r) = S_2^{(i)}(0) = \phi_i$$
$$\lim_{r\to \infty} S_2^{(i)}(r) = \phi_i^2 \tag{3.6}$$

As shown in **Eq. 3.6**, it is clear that two-point correlation function contains certain geometric information of the porous media since the asymptotic behavior approaches to volume phase fraction.

Moreover, the specific surface area s is defined as the area of two-phase interface per unit volume of the medium and it is a crucial characteristic length scale in porous medium. Assuming continuous medium, the specific surface area s is related to two-point correlation in different dimensions D [89]

$$\frac{d}{dr} S_2(r)|_{r=0} = \begin{cases} -\frac{s}{2} & D = 1 \\ -\frac{s}{\pi} & D = 2 \\ -\frac{s}{4} & D = 3 \end{cases} \tag{3.7}$$

where D is dimension and s the specific surface area.

The specific surface area has also been used in several permeability approximation models [90, 91]. Therefore, two-point correlation function is also connected with transport properties.

In addition to estimation of permeability using specific surface area s, permeability κ can also be estimated by empirical equation using characteristic length scale as a estimator.

The empirical equation is used to curve-fitting the experimental results for permeability measurement and it is shown below [92]

$$\kappa = a + b \ln \phi_{\text{void}} + c \ln \overline{\lambda} \tag{3.8}$$

$$\overline{\lambda} = \int_0^{\infty} {}^{\text{norm}} S_2^{(\text{void})}(r) dr \tag{3.9}$$

$${}^{\text{norm}} S_2^{(\text{void})}(r) = \frac{S_2^{(\text{void})}(r) - \phi_{\text{void}}^2}{\phi_{\text{void}} - \phi_{\text{void}}^2} \tag{3.10}$$

where κ is the permeability, ϕ_{void} the volume fraction of pore phase, $\overline{\lambda}$ the characteristic length scale, $S_2^{(\text{void})}$ the normalized two-point correlation function (also called auto-correlation function) and a, b, c are fitting coefficients used in [92].

To summarize, the two-point correlation function has been used to estimate specific surface area and characteristics length scale for two-length medium to estimate permeability. It is also related with geometric properties. Therefore, since the two-point correlation function is related with both geometric and physical properties of the porous medium, it is included in the catalyst layer characterization and reconstruction process.

3.1.4 Lineal Path Function

The lineal path function is defined as the probability that a line segment of length r lies entirely in the phase i when randomly thrown into the sample [39]. It can be represented mathematically as [40]

$$L^{(i)}(r) = P\{I^{(i)}(x_1) = 1, I^{(i)}(x_1 + dr) = 1, I^{(i)}(x_1 + 2dr) = 1, \cdots, I^{(i)}(x_2) = 1\} \tag{3.11}$$

where x_1 and x_2 are two points in space, line length r is defined as $r = x_2 - x_1$, and dr is the infinitesimal change in r.

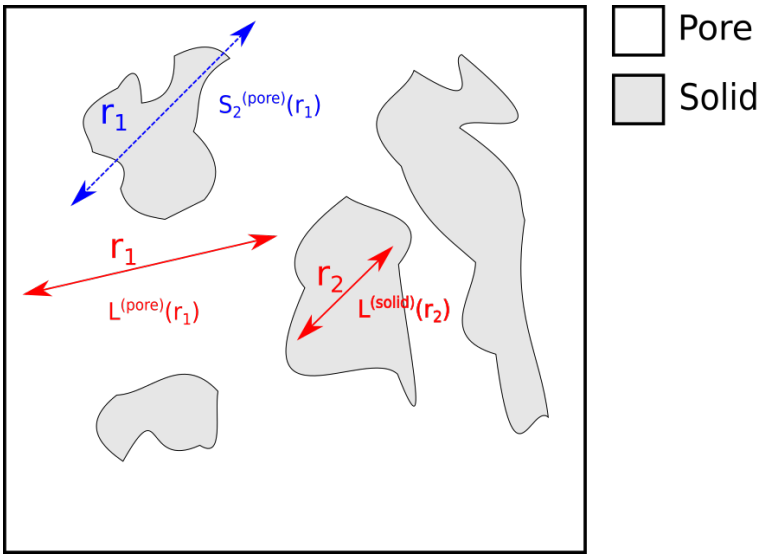

Fig. 3.3: A schematic showing instances of lineal path function in solid red lines with arrowheads and instances of two-point correlation function in dashed blue line with arrowheads (White phase is pore and grey phase is solid).

The lineal path function $L^{(i)}(r)$ is a monotonically decreasing function because the space available in phase i decreases as the length of line segment r is increased. At the two extreme cases, the lineal path function approaches asymptotically as follows [39]

$$\begin{aligned} \lim_{r\to 0} L^{(i)}(r) &= L^{(i)}(0) = \phi_i \\ \lim_{r\to\infty} L^{(i)}(r) &= 0 \end{aligned} \tag{3.12}$$

As depicted in **Fig. 3.3**, the two solid red line segments are instances of lineal path function. $L^{(\text{pore})}(r_1)$ stands for the the probability of finding a line segment of length r_1 wholly residing in the pore phase. Two-point correlation function represented by the

dashed blue line $S_2^{(\text{pore})}(r_1)$ stands for the probability of finding two end points of a line segment r_1 residing in the pore phase.

The two-point correlation function $S_2^{(i)}(r)$ only requires two endpoints of line segment r residing in the same phase i while the lineal path function $L^{(i)}(r)$ requires the whole line segment r residing in the same phase i; hence the lineal path function contains certain information on phase connectivity that is not captured by the two-point correlation function [88]. Additionally, the lineal path function is the integral form of the chord length function [41], similar to the pore size distribution function and characterizes cluster sizes in the microstructure; hence lineal path function is used for estimating the diffusion coefficient for Knudsen diffusion [93]. Therefore, the lineal path function has been selected to characterize and reconstruct catalyst layer.

3.1.5 Orthogonal Sampling Method and Boundary Treatment

The definitions of the statistical functions discussed so far in this chapter are in its continuous form. However, digital images are encountered in most of the engineering application. The discrete nature of digitized images provides easier ways to extract statistical information via sampling method. Practically speaking, orthogonal sampling method has been used in the correlation function computation in order to save computational costs rather than random sampling method. During sampling, boundary treatment including normal boundary treatment and periodic boundary treatment is also crucial in extracting statistical information and reconstruction.

As shown in **Fig. 3.4**, a pixelized porous medium image of size 6 by 6 in pixels consists

of pore phase in white and solid phase in grey. The orthogonal sampling method for a 2-D pixelized images is to sample every row and column of the image. Once sampling for all rows and columns are obtained, they are averaged separately in each direction.

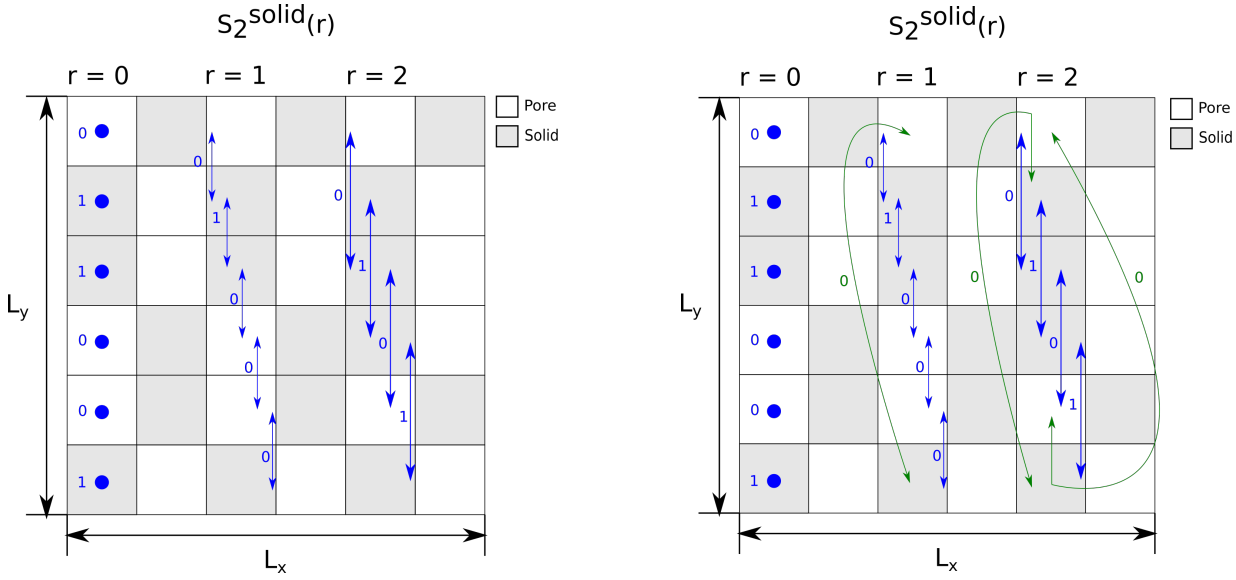

(a) Normal boundary treatment.

(b) Periodic boundary treatment.

Fig. 3.4: Schematic illustration of computation of $S_2^{\text{solid}}(r)$ by orthogonal sampling with normal and periodic boundary treatment. The normal boundary treatment takes sampling points until at the edge of the image, while the period boundary treatment loops around the perimeter to the other side of the image (shown in green curved lines with arrowheads).

For a pixel column, the two-point correlation is computed as

$$S_2^i(r) = \frac{1}{L_y - r} \sum_{1}^{L_y - r} I_{x,y}^i I_{x,y+r}^i \tag{3.13}$$

where L_y is the length in y-direction.

When it comes to orthogonally sample an image, there are two types of boundary treatment. The normal boundary treatment is to sample from the beginning of an image to the

end of it. As shown in **Fig. 3.4a**, there are three instances of column sampling of $S_2^{\text{solid}}(r)$ with orthogonal sampling. For computing $S_2^{\text{solid}}(r)$ with normal boundary treatment, as r increases, the number of sampled points decrease since the sampling process stops at the edge of an image. However, it is different in the case of periodic boundary treatment where the sampling process is looped around to the the start of the image for line segment r as schematically illustrated in **Fig. 3.4b**. Typically, normal boundary treatment is used at edges without periodicity, while periodic boundary treatment is for the edges requiring periodicity.

Orthogonal sampling of lineal path function $L^{(i)}(r)$ for digitized images is different from computation of two-point correlation function. The lineal path function $L^{(i)}(r)$ for a pixelized image is defined as the probability of finding a line crossing r pixels which belongs to phase i. Prior to the computation of lineal path function $L^{(i)}(r)$, the chord length for phase i must be calculated. As schematically shown in **Fig. 3.5** for the computation of $L^{\text{solid}}(r)$, the iteration stops whenever it encounters an interfacial pixel (pore pixel) and then the chord of length l of solid pixel has been recorded. Once chord length l is known, for a pixel column, the lineal path function for phase i is defined as

$$L^i(r) = \begin{cases} \frac{l-r}{L_y-r} & \text{when} \quad 0 \leq r \leq l \\ 0 & \text{otherwise} \end{cases} \tag{3.14}$$

where l is the chord length and L_y the height of the image.

In this thesis research, the orthogonal sampling with the normal boundary treatment has been used to compute the statistical functions from images because those images are

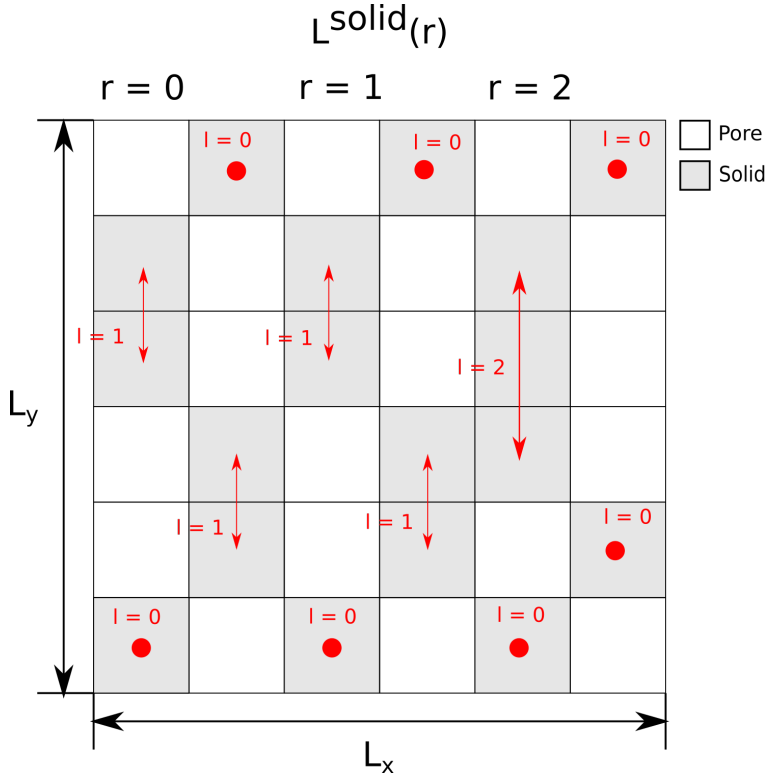

Fig. 3.5: Schematic illustration of computation of $L^{\text{solid}}(r)$ by orthogonal sampling with normal boundary treatment.

generally from experimental image technique where edge periodicity is absent. As for reconstruction of the CL, a combination of both normal and periodic boundary treatment has been used to estimate the structure in this thesis. Normal boundary treatment has been selected to reconstruct the through-plane direction of the CL, while the periodic boundary treatment has been chosen to reconstruct the in-plane of the CL. As the CL is designed with lower platinum loading for cost reduction, the thickness (through-plane direction) is much smaller than the catalyst layer's length and width (in-plane direction). The reconstructed catalyst layer is a sub-volume of the catalyst layer and it needs to be representative of the whole CL. Therefore, periodic boundary treatment has been used in

in-plane direction to ensure periodicity for in-plane dimensions (length and width), while normal boundary treatment has been employed in the through-plane direction (thickness) where periodicity is no longer required due to small thickness compared with the length and width of the CL.

3.2 Validation of the Statistical Function Algorithm

Before the reconstruction process, it is crucial to validate the accuracy of the algorithm that computes the statistical function against available analytical solution for idealized porous medium. The idealized porous medium is the randomly packed penetrable spheres model, which is an extension of the well-known randomly packed impenetrable spheres model, as schematically represented in **Fig. 3.6**.

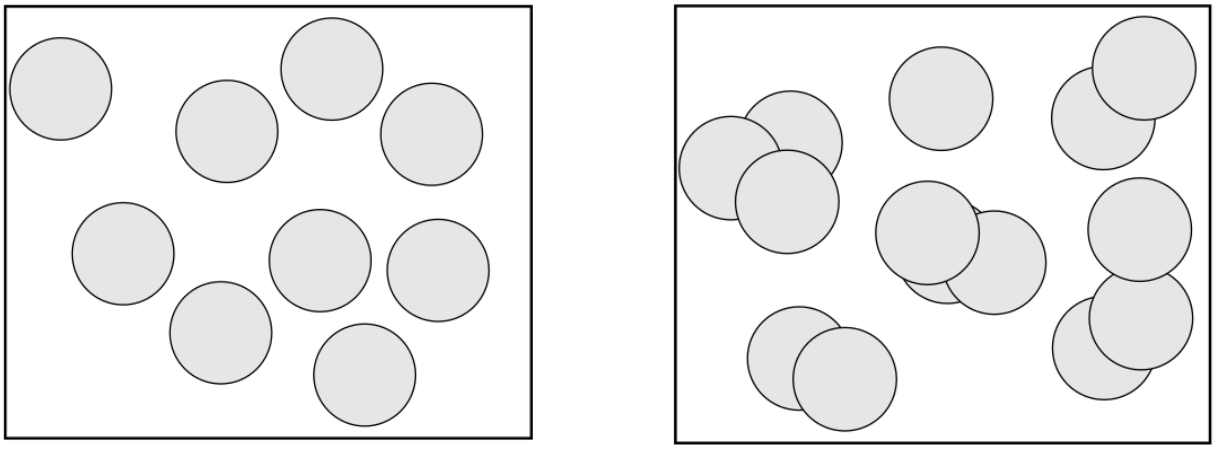

(a) Impenetrable spheres model.

(b) Penetrable spheres model.

Fig. 3.6: Schematic of randomly packed impenetrable and penetrable spheres model.

Berryman [94] and Coker [89] mathematically derived the analytical solution for two-

Table 3.1: Input and output parameters for the randomly generated penetrable spheres.

Parameters	Symbol	Value	Units
Input Parameters			
Number of Spheres	N_{sphere}	110	-
Sphere Radius	R_{sphere}	8	Voxels
Domain Size	N^3	64^3	Voxels
Output Parameters			
Pore Volume Fraction	ϕ_{pore}	0.4518	-
Sphere Packing Density	ρ	0.00037	$\frac{\text{sphere}}{\text{voxel}^3}$

point correlation function and lineal path function for void phase in randomly packed penetrable spheres model, respectively.

Firstly, a random number generator has been used to randomly spawn sphere of radius R_{sphere} inside a computational domain size of 64 x 64 x 64 until the total number of spheres N_{sphere}, as shown in **Fig. 3.7**. Then the pore volume fraction ϕ_{pore} is calculated by iterating through the whole domain to determine whether the voxel center is inside any of the spheres to obtain the total number of pore voxel then divided by the total number of voxels.

The sphere packing density ρ is defined as [94]

$$\rho = \frac{-3 \ln \phi_{\text{pore}}}{4\pi R_{\text{sphere}}^3} \tag{3.15}$$

where ϕ_{pore} is the pore volume fraction and R_{sphere} the radius of sphere.

The detailed input and output parameters used are listed in **Table. 3.1**.

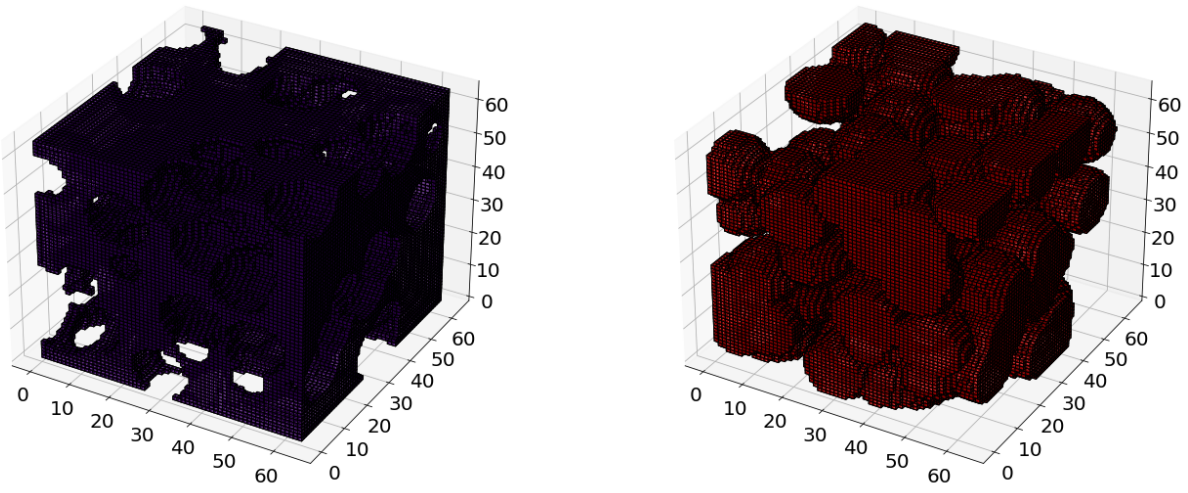

(a) Pore phase.

(b) Solid phase.

Fig. 3.7: Segmented phases in randomly generated penetrable solid spheres (a) pore phase (purple); (b) solid phase (red).

3.2.1 Validation of Two-point Correlation Function

The analytical solution for the two-point correlation function of void phase in a randomly packed penetrable spheres model is given as [94]

$$
\begin{aligned}
S_2^{\text{pore}}(r) &= \exp\{-\rho V_2(r)\} \\
\frac{V_2(r)}{R_{\text{sphere}}^3} &= \begin{cases} \frac{4\pi}{3}\left(1 + \frac{3r}{4R_{\text{sphere}}} - \frac{r^3}{16R_{\text{sphere}}^3}\right) & \text{for} \quad \frac{r}{R_{\text{sphere}}} < 2 \\ \frac{8\pi}{3} \quad \text{for} \quad \frac{r}{R_{\text{sphere}}} \geq 2 \end{cases}
\end{aligned}
\tag{3.16}
$$

where $V_2(r)$ is the union volume of two spheres of the same radius R_{sphere} apart from each other by distance r. When r is zero, two spheres overlap each other and the union volume $V_2(r)$ is $\frac{4\pi}{3}R_{\text{sphere}}^3$. When $r \geq 2R_{\text{sphere}}$, the union volume $V_2(r)$ is the total volume of two

spheres $\frac{8\pi}{3}R^3_{\text{sphere}}$.

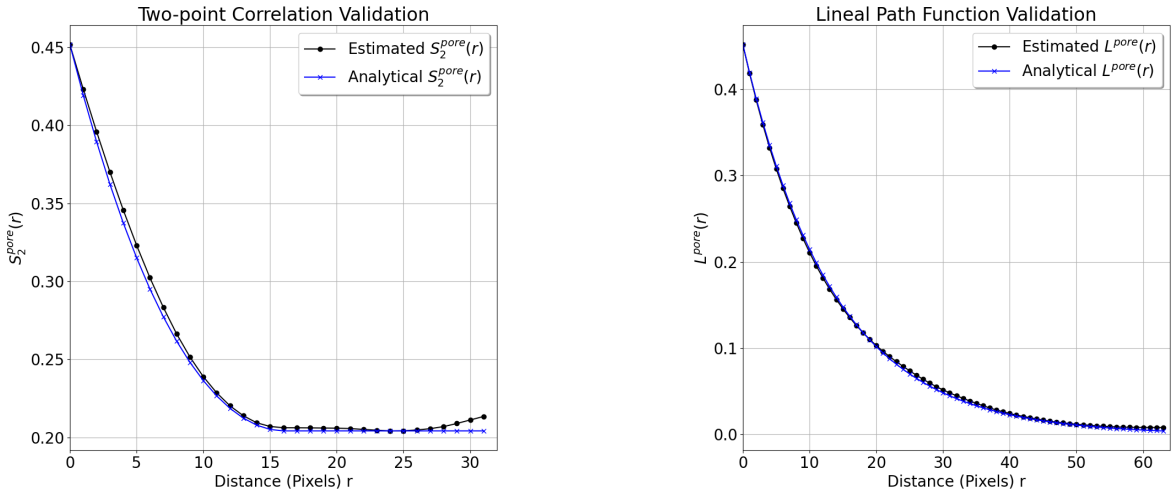

(a) Two-point correlation function S_2^{pore}.

(b) Lineal path function L^{pore}.

Fig. 3.8: Comparison of analytical and estimated (a) two-point correlation function for the pore phase; (b) lineal path function for the pore phase.

The comparison of analytical and computed two-point correlation function for the pore phase is shown in **Fig. 3.8a**. An orthogonal sampling with normal boundary treatment has been adopted to compute the two point correlation function $S_2^{\text{pore}}(r)$ for the pore phase. Reasonable agreement has been observed in **Fig. 3.8a** until the distance r approaches half of the domain size N. The two-point correlation function does not include any long-range information [95], hence not suitable to characterize long-range features of the microstructure statistically [96]. It is also why the two-point correlation function alone is not capable of characterizing the CL microstructure, and combination with other statistical functions is necessary, such as lineal path function. Moreover, the asymptotic behavior (when $r \to 0$, $S_2^{\text{pore}}(r) \to \phi_{\text{pore}}$; when $r \to \infty$, $S_2^{\text{pore}}(r) \to \phi^2_{\text{pore}}$) agrees fairly well as previously discussed

in **Eq. 3.6**. Therefore, the algorithm for computing the two-point correlation function is validated against the analytical solution.

3.2.2 Validation of Lineal Path Function

The analytical solution for the lineal path function for the pore phase is given as [89]

$$L^{\text{pore}}(r) = \phi_{\text{pore}}^{1+\frac{3r}{4R_{\text{sphere}}}} \tag{3.17}$$

As shown in **Fig. 3.8b**, the numerical results agree fairly well with the analytical results for lineal path function of pore phase $L^{\text{pore}}(r)$. Moreover, the asymptotic behavior (when $r \to 0$, $L^{\text{pore}}(r) \to \phi_{\text{pore}}$; when $r \to \infty$, $L^{\text{pore}}(r) \to 0$) agrees fairly well as previously discussed in **Eq. 3.12**. Therefore, the algorithm for computing the lineal path function is validated against the analytical solution. The combination of the two-point correlation function and the lineal path function is adopted for the reconstruction part of this thesis research.

It needs to be addressed that the analytical solution for both S_2^{pore} and L^{pore} is derived based on continuous domain. In contrast, the reconstructed structure is based on discretized domain. The discrepancy between the analytical and estimated solution becomes less and less as more voxels have been used to discretize the domain. The domain size N^3 used in the validation is 64^3. As the domain size N is increased, the discrepancy decreases.

3.3 Stochastic Reconstruction of Catalyst Layer

This section discusses the sphere-based stochastic reconstruction method developed in this work and detailed architecture is illustrated in **Fig. 3.9**. Firstly, the segmented CL data is converted to a binary state consisting of solid and pore. The statistical correlation functions S_2 and L is extracted by orthogonal sampling functioning as the blueprint for the reconstruction process. The reconstruction process consists of three modules: (i) Module 1 initialization of carbon spheres, (ii) Module 2 stochastic reconstruction, (iii) Module 3 segmentation, as described below.

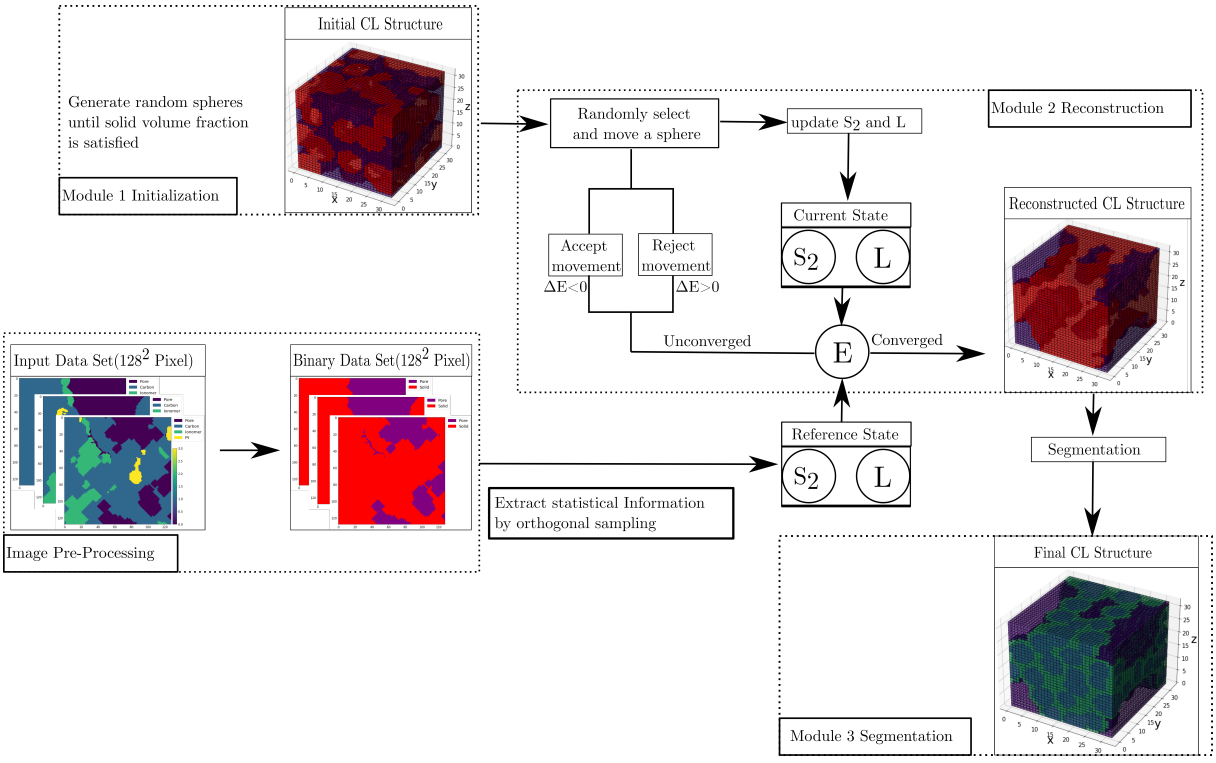

Fig. 3.9: Schematic showing the architecture of the reconstruction process.

3.3.1 Simplifications

The hybrid reconstruction method proposed in this thesis work is based on the following simplifications

- The volume fraction of platinum is assumed to be negligible for the reconstruction method for obtaining simple geometry for the numerical modelling work shown in Chapter 4 and 5.
- The current reconstruction method contains the high-order statistical information for binary phase of solid (ionomer, carbon and platinum) and pore phase such as two-point correlation function and lineal path function. After segmenting the carbon and ionomer phase from the solid phase, some of statistical information may be lost.
- The size of the spheres is assumed to be same for simplicity.
- The ionomer thin film is assumed to be uniform and wraps around the carbon agglomerate.

3.3.2 Image Processing

Multiphase Medium

Generally, any digitized image could be used for the reconstruction purpose. The catalyst layer image was received from Toray, Japan. The image was obtained using Toray in-house analysis. The details regarding their catalyst layer imaging technique and analysis conducted are confidential. As schematically shown in **Fig. 3.10a**, the CL received from

Toray has been converted into an three-dimensional array of size 128 x 128 x 128 where different numerical value indicates different phases with 0 for the pore, 1 for carbon, 2 for the ionomer and 3 for the platinum phase. Each colour indicates a different phase with pore phase in purple, carbon phase in blue, ionomer phase in green and platinum phase in yellow. The CL microstructure received is very pixelated and rough interface making it unsuitable for conducting numerical analysis with the current structure.

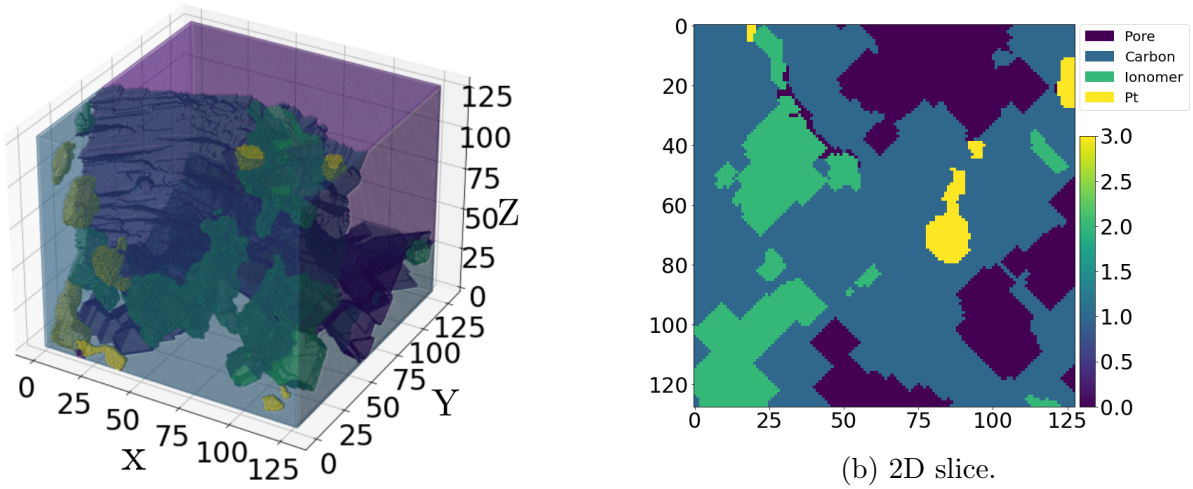

(a) 3D CL microstructure.

(b) 2D slice.

Fig. 3.10: (a) Digitized CL data from Toray with dimension of 128 x 128 x 128 in unit voxel; (b) 2D slice of the 3D CL microstructure in xy plance at $z = 16$.

It is worth mentioning that the voxel nature of the CL structure is very compatible with LBM which is a lattice-based method for fluid flow analysis. However, the interest of this thesis research is in the solid domain and the main solver is based on FEM requiring smooth edges. The convergence issue caused by rough edges is pronounced in the delamination model described in Chapter 4. Hence, the reconstruction part of the thesis work has to reconstruct the CL microstructure without rough edges. It is the reason why the recon-

struction work in this thesis research incorporates randomly packed spheres which gives smooth edges and extends the capability of statistical reconstruction for numerical modelling. Due to the complexity of the three-dimensional microstructure, a two-dimensional slice at $z = 16\,[\text{voxels}]$ has been taken for analysis in this thesis research, as shown in **Fig. 3.10b**. The size of the two-dimensional CL slice is 128 x 128 in unit pixels. In **Fig. 3.11**, the two-point correlation function $S_2^{(i)}(r)$ and lineal path function $L^{(i)}(r)$ for pore, carbon, ionomer and platinum phases are extracted from the two-dimensional slice of CL microstructure. As discussed in the previous section, the two point correlation function $S_2^{(i)}(0)$ at $r = 0$ is the volume fraction for phase i. The volume fraction ϕ_i for pore, carbon, ionomer and the platinum phase is 22.33 %, 60.96 %, 14.27 % and 2.44 %, respectively. In **Fig. 3.11a**, the S_2^{pore} reduces quickly from ϕ_{pore} until reaching the minimum 2.26 % at $r = 45$, and jumps back up as r is increased to the size of the square image. Since $S_2^{\text{pore}}(r)$ means the probability of finding two endpoints of the line segment of length r both residing in the pore phase of the microstructure image, it can be used to visualize the probability distribution of the feature of interest in the microstructure image. The probability of finding two endpoints of line of length $r = 45$ inside the pore phase $S_2^{\text{pore}}(45)$ is the lowest for the microstructure in **Fig. 3.10b**. When the feature size r is greater than $r = 45$, the $S_2^{\text{pore}}(r)$ increases again. It is because there are some pores near the opposing edges of the image presented in **Fig. 3.10b**. It has some implications in the geometric information of the microstructure image. However, from a physics point of view, it is essential to know both how far pores are distributed and the size of the pore, and the two-point correlation function fails to provide accurate information for the size of the pore. Additionally, it has been suggested that the two-point correlation function suffers at characterizing

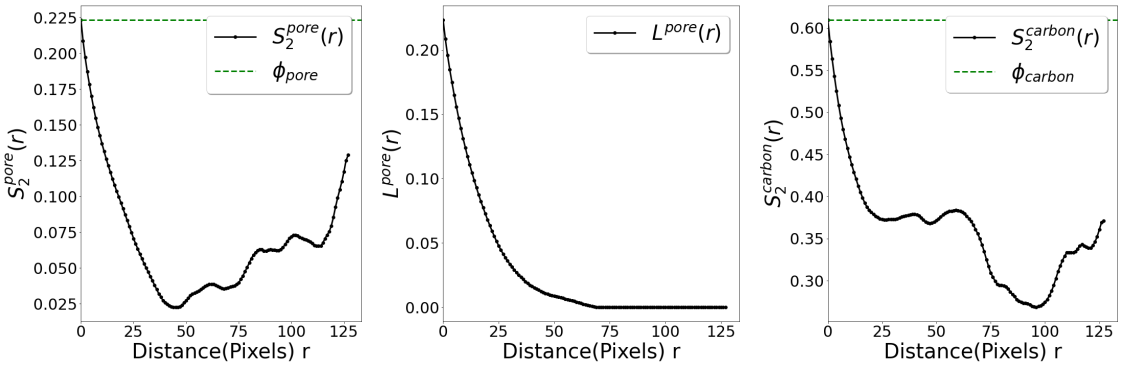

(a) $S_2^{\text{pore}}(r)$ (b) $\text{L}^{\text{pore}}(r)$ (c) $S_2^{\text{carbon}}(r)$

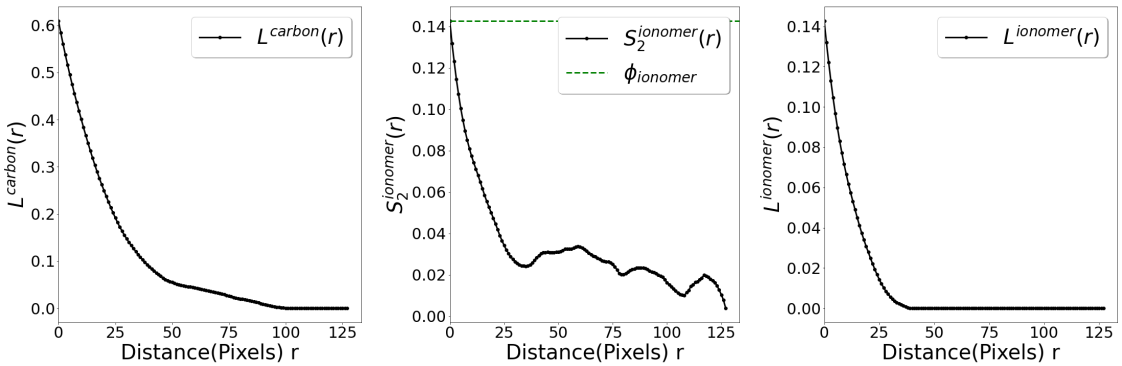

(d) $\text{L}^{\text{carbon}}(r)$ (e) $S_2^{\text{ionomer}}(r)$ (f) $\text{L}^{\text{ionomer}}(r)$

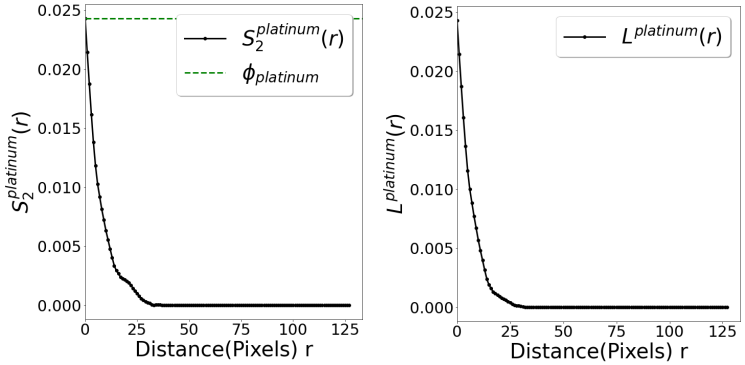

(g) $S_2^{\text{platinum}}(r)$ (h) $\text{L}^{\text{platinum}}(r)$

Fig. 3.11: The $S_2^{(i)}(r)$ of (a) pore, (c) carbon, (e) ionomer, (g) platinum; and $\text{L}^{(\text{i})}(\text{r})$ of (b) pore, (d) carbon, (f) ionomer, and (h) platinum extracted from **Fig. 3.10b**.

the domain-wide phase features [95, 96]. Therefore, the lineal path function is incorporated in the thesis research to enhance the statistical characterization capability of the microstructure images and to reconstruct a more accurate representation of the CL microstructure.

In **Fig. 3.11a**, the lineal path function for pore phase $\mathrm{L}^{\mathrm{pore}}(r)$ is presented. The $\mathrm{L}^{\mathrm{pore}}(r)$ means the probability of finding all points of the line segment of length r residing in the pore phase of the microstructure image. The $\mathrm{L}^{\mathrm{pore}}(r)$ starts from ϕ_{pore} at $r = 0$ and then exponentially decays to 0 as r increases. Physically, it means that the chances of finding a line segment of length r which fits in the pore becomes more and more unlikely as r is increased to the domain size. The lineal path contains information regarding the size of the pore in microstructure [41]. It is a great enhancer when used in conjunction with the two-point correlation function to characterize experimental images and to reconstruct CL microstructure. Similar to the discussion in **Fig. 3.11a** and **Fig. 3.11b**, the **Fig. 3.11c-h** presents the two-point correlation function and lineal path function for carbon, ionomer and solid phase. It would not be discussed in detail here to avoid redundancy.

Binary Medium

Since the research interest is the morphological changes of the solid phase, the microstructure presented in **Fig. 3.10b** has been converted to a binary medium with pore phase and solid phase, as presented in **Fig. 3.12c**. The two-point correlation function $S_2^{\mathrm{solid}}(r)$ and lineal path function $\mathrm{L}^{\mathrm{solid}}(r)$ of the solid phase are presented in **Fig. 3.12a** and **Fig. 3.12b**. Based on the image analysis, the solid volume fraction ϕ_{solid} is 77.67 %. Both $S_2^{\mathrm{solid}}(r)$ and $L^{\mathrm{solid}}(r)$ are used for the reference functions for the reconstruction process. One of the

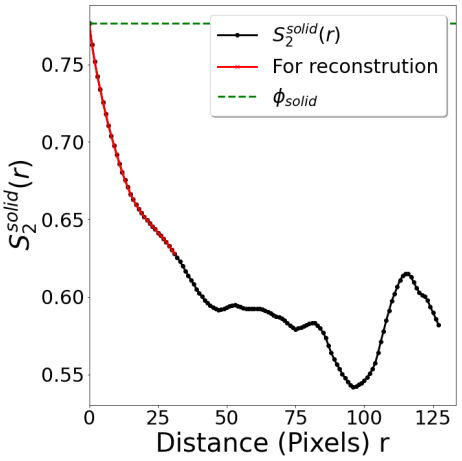

(a) $S_2^{\text{solid}}(r)$

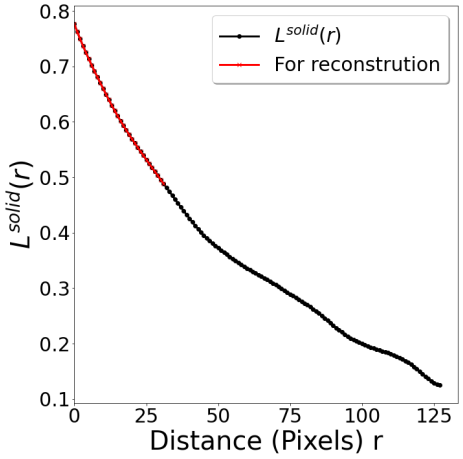

(b) $\text{L}^{\text{solid}}(r)$

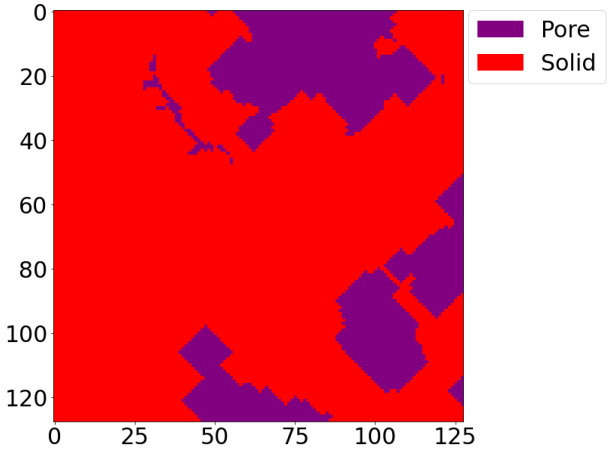

(c) Binary CL medium

Fig. 3.12: (a) The two-point correlation function $S_2^{(i)}(r)$ for solid phase; (b) the lineal path function $\text{L}^{\text{solid}}(r)$ for solid phase; (c) 2D slice of the CL microstructure with solid and pore phase.

characteristic length suggested for reconstruction is obtained by observing the distance r when the $S_2^{\text{solid}}(r)$ reaches ϕ^2_{solid} [89]. From **Fig. 3.12a**, the characteristic length is around 35 pixels. It is suggested that the reconstruction size should be at least in the same order of magnitude of the reconstruction characteristic length. Therefore, a reconstruction domain of 32 x 32 x 32 is selected based on the suggested criteria and limited computational cost.

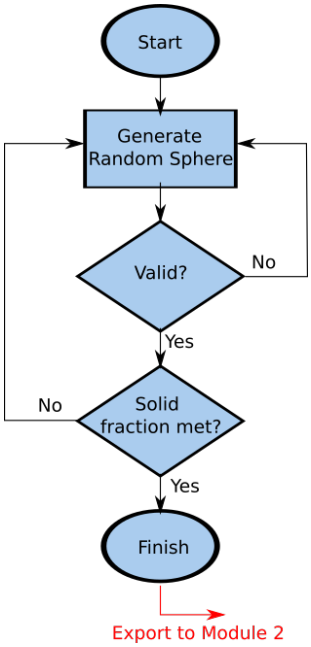

Fig. 3.13: Schematic flowchart for the Module 1 Initialization of the reconstruction algorithm.

3.3.3 Module 1 Initialization

The first step of the reconstruction process is to generate an array of spheres. The solid phase of the CL microstructure is represented by a series of spheres. The radius of the sphere is assumed to be constant in this study and spheres become the unit elements in the computational domain. As schematically shown in **Fig. 3.13**, the trail spheres are introduced one at a time into the computational domain until the solid fraction has been met. The radius of the sphere is assumed to be constant in this study. The trial spheres are randomly generated in the computational domain of size N x N x N in unit voxels. The trial sphere is accepted at a probability to avoid spheres over-clustering. The acceptance

probability is given by [45]

$$P(\nu) = \exp\left(-\frac{\nu}{\epsilon_v}\right) \tag{3.18}$$

where ν is the ratio of the overlapped volume to the volume of a sphere and ϵ_ν is a parameter controlling the cluster of spheres related to the structure of agglomerates [45].

The initialization process terminates after the solid volume fraction ϕ_{solid} has been met and detailed parameters used in the initialization is summarized in **Table 3.2**.

Table 3.2: Input parameters for Module 1 Initialization

Parameters	Symbol	Value	Units
Input Parameters			
Solid Volume Fraction	ϕ_{solid}	0.7767	-
Sphere Radius	R_{sphere}	5	Voxels
Domain Size	N^3	32^3	Voxels
Cluster Parameter	ϵ_ν	0.5	-

A sensitivity study has been conducted to analyze the impact of the cluster parameter ϵ_ν and R_{sphere} used in the initialization process. Since the evaluation of two-point correlation function and lineal path function requires $O(N^4)$ operations [45], the domain size N is selected to be a relatively small value of $N = 32$ to save reconstruction time. The cluster parameter ϵ_ν controls the level of clusterness in the computational domain. If the trial sphere doesn't overlap with any of the existing spheres at all, the acceptance probability is 100 %. If the trial sphere overlaps with the existing domain, the higher the overlapping volume ν, the less probable for the trial sphere to be accepted. As the cluster parameter ϵ_ν gets larger, the probability for accepting trial sphere becomes higher, and hence the more spheres end up in domain after initialization. More spheres in the computational domain result in an increase in reconstruction time in the subsequent module.

If there are not enough spheres inside the computational domain, the residual in the reconstruction module plateaus and the reconstruction doesn't reaches convergence in reasonable amount of time. As schematically shown in **Fig. 3.14**, the number of spheres inside the computational domain increases from 79 to 103 as the clusterness parameter ϵ_ν increases from 0.1 to 0.9. The impact of varying cluster parameter ϵ_ν doesn't have much impact on the number of spheres in the domain which correlates with the computational cost. Therefore, the cluster parameter is selected to be 0.5 for this thesis research. As for the selection of the radius of the sphere R_{sphere}, ideally it should be selected according to the radius distribution of carbon black in the sample. In this thesis research, the radius

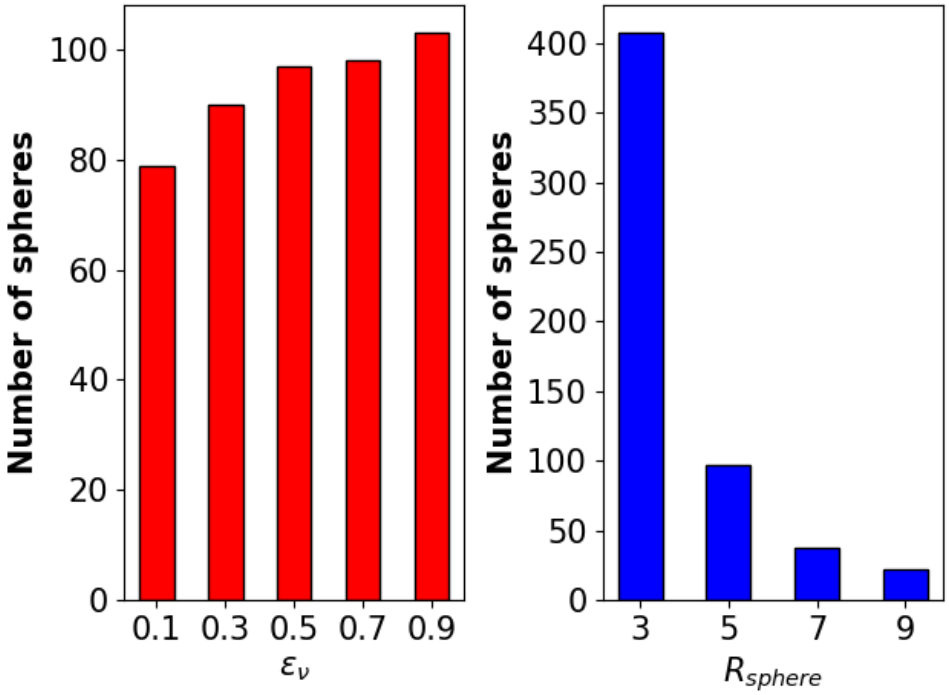

Fig. 3.14: Sensitivity studies of varying clusterness parameters ϵ_ν with domain size N = 32 and $R_{\text{sphere}} = 5$, and varying sphere radius R_{sphere} with domain size N = 32 and $\epsilon_\nu = 0.5$.

of sphere is assumed to be constant for simplicity. In this thesis research, sphere has been used as an unit element to reconstruct the final agglomerate structure based on the Toray image. As the radius of sphere decreases, the total number of sphere increases in the computational domain. Increasing number of spheres would increase the computational cost for the subsequent reconstruction. As schematically shown in **Fig. 3.14**, as the sphere radius increases from 3 to 5, the number of spheres inside the domain decreases from 407 to 97. Order of magnitude difference has been observed with varying sphere radius. Therefore, with the selection of domain size $N = 32$ and cluster parameter $\epsilon_\nu = 0.5$, a radius of five voxels for the spheres R_{sphere} is selected in this thesis research.

The voxelized CL microstructure is shown in **Fig. 3.15c**. The two-point correlation functions and lineal path functions for the initialized CL microstructure are presented in **Fig. 3.15a** and **Fig. 3.15b**. It can be observed that the $S_2^{\text{solid}}(r)$ and $\text{L}^{\text{solid}}(r)$ at $r = 0$ in initialized structure match well with those of the reference structure since the solid volume fraction is the only convergence criterion for the initialization process. Significant difference in the $S_2^{\text{solid}}(r)$ and $L^{\text{solid}}(r)$ of the initialized structure and reference structure has been observed. It echoes with the fact that the fabrication-based reconstruction that only uses volume fraction as a convergence criterion is not a good representation of the CL microstructure in terms of its statistical characteristics. The details on how to reduce the difference between the reconstructed microstructure and experimental microstructure will be described in the next section.

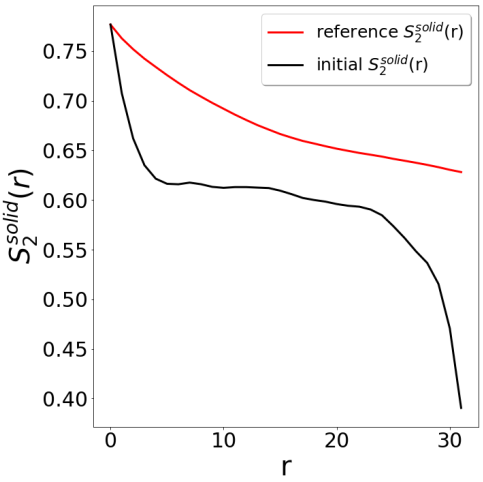

(a) $S_2^{\text{solid}}(r)$ comparison.

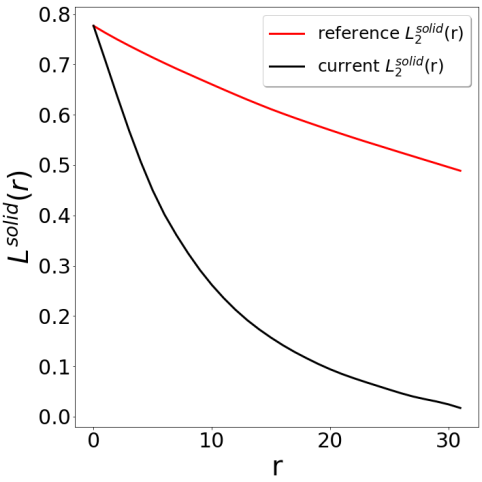

(b) $\text{L}^{\text{solid}}(r)$ comparison.

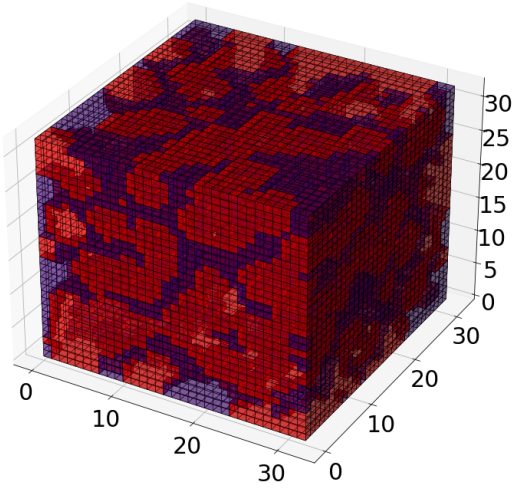

(c) Initialized CL structure.

Fig. 3.15: Initialized catalyst layer structure: (a) and (b) are the comparison of $S_2^{\text{solid}}(r)$ and $L^{\text{solid}}(r)$ of the initial CL structure with the reference CL structure; (c) Initialized CL structure (red is solid, purple is pore).

3.3.4 Module 2 Reconstruction

Simulated Annealing Method

The reconstruction process is essentially converted to an optimization problem to minimize the difference between the current microstructure and the reference microstructure. As discussed in Chapter 2, the common optimization method includes SA [45,47] and Gaussian field [42, 43]. Since the Gaussian field method is not able to include multiple statistical correlation functions [47], the SA method is selected. The SA method is named after the metal annealing process, where the system's internal energy and physical temperature are minimized. The SA process in this thesis research is achieved by randomly selecting and moving spheres inside the domain in the direction of discrepancy minimization as presented in **Fig. 3.16**. The measure of the discrepancy between the current CL microstructure and the experimental image is named energy E. It is defined as the sum of the squared difference between the difference in all correlation functions as shown below

$$E = \sum_{r=0}^{N} \left[S_{2,\text{ref}}^{\text{solid}}(r) - S_2^{\text{solid}}(r)\right]^2 + \left[L_{\text{ref}}^{\text{solid}}(r) - L^{\text{solid}}(r)\right]^2 \tag{3.19}$$

where N is the length of the computational box, $S_{2,\text{ref}}^{\text{solid}}$ the two-point correlation function of the reference image from Toray, $L_{\text{ref}}^{\text{solid}}$ the lineal path function of the reference image from Toray, S_2^{solid} the two-point correlation function of the reconstructed CL structure and L^{solid} the lineal path function of the reconstructed CL structure.

A sphere in the current structure is randomly selected to be moved a random displacement and the energy of the current structure ${}^{i+1}E$ is evaluated and compared with the

energy ${}^{i}E$ before the random movement. The change in energy $\Delta\,{}^{i}E$ for the iteration i is defined as

$$\Delta\,{}^{i}E = {}^{i+1}E - {}^{i}E \tag{3.20}$$

where ${}^{i}E$ is the energy for the reconstructed CL microstructure in iteration i and ${}^{i+1}E$ the energy for the trial CL microstructure in trial iteration $i+1$.

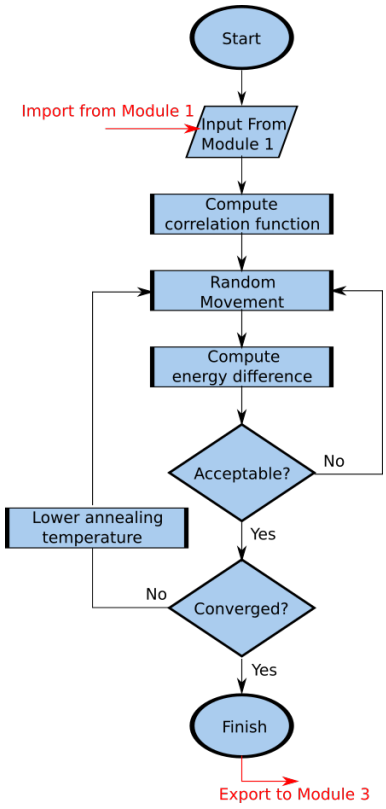

Fig. 3.16: Schematic flowchart for the Module 2 reconstruction algorithm.

Energy Minimization Algorithm

After the definition of the energy E and change in energy $\Delta^i E$, an energy minimization algorithm is needed to accept the energy change $\Delta^i E$ based on a certain criterion. There are two common approaches in the field of SA including a threshold energy based energy minimization proposed by Dueck *et al.* [97] and a probability based energy minimization proposed by Metropolis *et al.* [98]. The Dueck method accepts change in energy as long as it satisfies a threshold value such as $\Delta^i E \leq E_{\text{threshold}}$, and rejects other change in energy if $\Delta^i E > E_{\text{threshold}}$. The threshold value $E_{\text{threshold}}$ is a small positive number either determined from the initial system energy or simply a constant value. The Dueck method accepts every energy-decreasing movement ($\Delta^i E < 0$) and accepts energy-increasing move as long as it is less than or equal to the threshold value ($0 \leq \Delta^i E \leq E_{\text{threshold}}$). Some energy-increasing movement below threshold value ($0 \leq \Delta^i E \leq E_{\text{threshold}}$) is allowed in case the system is trapped in local minimum. The Dueck method has reduced computational time compared with other methods [98]. However, the Dueck method does not allow any movement above the threshold value ($\Delta^i E < 0$). It is important to have energy-increasing movement in order to avoiding being trapped in the local minimum. The Dueck method causes that some certain states of the microstructure is not accessible by this aggressive rejection [99]. On the other hand, the probability based Metropolis method accepts all energy-decreasing iteration and accepts energy-increasing iteration with a probability. Metropolis method allows all states of the microstructure to be accessible at the price of increased computational cost. Therefore, Metropolis method has been selected as the

energy minimization method in this thesis research. It is defined as [98]

$$P\left(\Delta\,{}^{i}E\right) = \begin{cases} 1, & \Delta E \leq 0 \\ \exp\left(\frac{-\Delta\,{}^{i}E}{{}^{i}T}\right), & \Delta E > 0, \end{cases} \tag{3.21}$$

where $\Delta\,{}^{i}E$ is the energy change for iteration i, $P\left(\Delta\,{}^{i}E\right)$ the probability of accepting the trial sphere movement in iteration $i+1$ with energy change of $\Delta\,{}^{i}E$ and ${}^{i}T$ the annealing temperature for iteration i.

The Metropolis method accepts every energy-decreasing iteration and accepts energy-increasing iteration at a ratio controlled by annealing temperature T. The rate of change of T is called cooling schedule. The detail on the cooling schedule and annealing temperature T is described in the following section.

Cooling Schedule

Annealing temperature T plays an important role in SA with the Metropolis method since it directly determines the probability of accepting energy-increasing iteration, and hence influences the computational time and whether the system energy would converge to the global minimum without being trapped in the local minimum.

In literature, there are two types of cooling schedules including the logarithmic cooling schedule [100] and power-law schedule [101]. The logarithmic cooling schedule is rarely used in literature because it reduces the temperature too slow to ensure fast convergence [102]. The power-law schedule is preferred in the literature due to its robustness and hence

adopted in this thesis research. It is defined as [101]

$$^{i+1}T = \lambda\, ^{i}T \tag{3.22}$$

where λ is the temperature reduction parameter typically less than one, i the iteration step, ^{i}T the temperature at current iteration step and ^{i+1}T the temperature at next iteration step.

The temperature reduction parameter λ could be either a constant value or a dynamic value dependent on the current system energy [103]. The dynamic λ is an ad-hoc formula without being mathematically derived. No clear evidence has been provided to support the argument that the dynamic λ would speed up the reconstruction process and is suitable for all microstructure [104, 105]. Therefore, a constant temperature reduction parameter λ is selected.

The initial annealing temperature of the reconstruction is determined from the energy change for the first couple of energy increasing iterations. The following equation is used to estimate the initial temperature [102]

$$\begin{aligned} ^{0}T &= \frac{-\overline{\Delta E}}{\ln P_0} \\ \overline{\Delta E} &= \frac{1}{N_{\text{init}}} \sum_{i=1}^{N_{\text{init}}} \Delta\, ^{i}E \end{aligned} \tag{3.23}$$

where N_{init} is the number of energy increasing step specified by user, ^{0}T the initial annealing temperature, P_0 the probability of accepting energy-increasing iteration at the beginning

of reconstruction (usually 0.5), $\overline{\Delta E}$ the average of the change of energy in the first N_{init} number of energy increasing iteration, $\Delta^{i}E$ the energy difference at iteration i.

Table 3.3: Input parameters and boundary treatment for Module 2 Reconstruction

Parameters	Symbol	Value	Units
Input Parameters			
Temperature Reduction Parameter	λ	0.9	-
Parameter for T_{init}	N_{init}	10	-
Probability for T_{init}	P_0	0.5	-
Convergence Criteria	$\varepsilon_{\text{recon}}$	0.005	-
Components	Boundary Treatment Method		
xy planes	Normal Boundary Treatment (in-plane direction)		
xz and yz planes	Periodic Boundary Treatment (through-plane direction)		

The detailed input parameters for the reconstruction process is summarized in **Table 3.3**. For this reconstruction, different sampling methods have been used for different boundaries as previously discussed in **Section 3.1.5.** Periodic boundary treatment has been applied to xz and yz planes while normal boundary treatment has been applied to xy planes due to through-plane dimension is significantly less than the in-plane dimension for the CL.

The aim of the reconstruction is to minimize the energy E as described in **Equ. 3.19**. Ideally, the energy should be minimized to zeros where the reconstructed CL structure is exactly the same as the experimental image in terms of statistical information. Realistically, the energy is often reduced to below a specified tolerance $\varepsilon_{\text{recon}}$ called convergence criteria. As schematically shown in **Fig. 3.17a**, the residual energy E is plotted against the reciprocal of the annealing temperature T. It can be observed that from the zoom-in plot for the first 100 successful iterations the energy E decreases in an exponentially decaying manner. This behaviour is caused by large statistical information variations in the

early stage of the reconstruction. A random movement of the sphere is easy to result in reduction in energy residual E ($\Delta E < 0$).

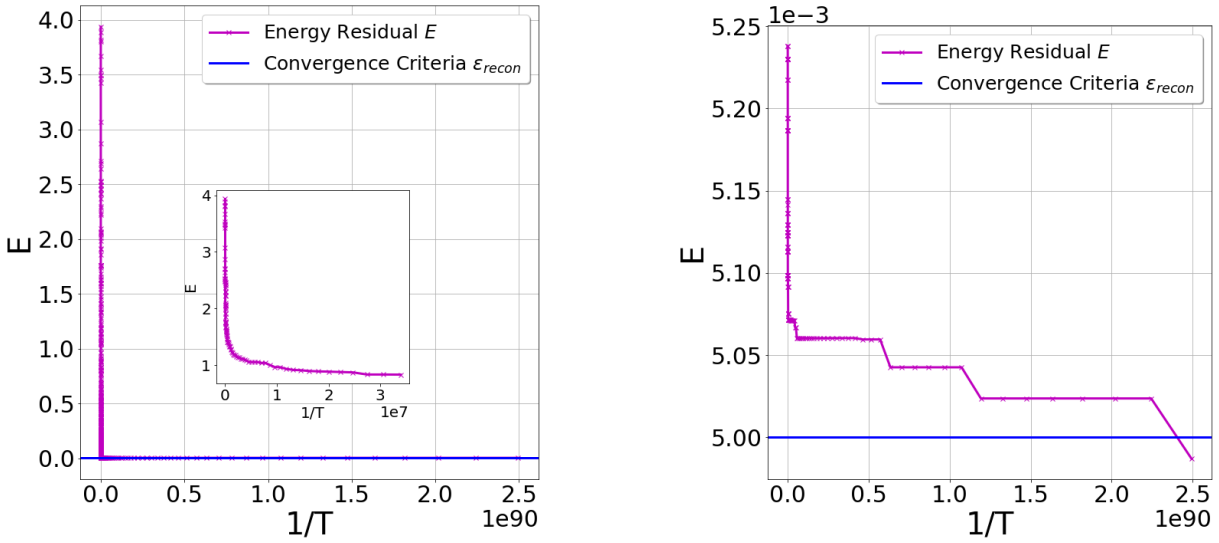

(a) (b)

Fig. 3.17: (a) Convergence chart with energy residual E as a function of the reciprocal of the annealing temperature for all successful iterations with zoomed in figure for the first 100 successful iterations; (b) Convergence chart for the last 100 successful iterations.

However, the above statement does not hold true for the later stage of the reconstruction process as illustrated in **Fig. 3.17b**. The energy E reduces at a much slower rate with a "staircase" phenomena where marginal drops in energy E for many successful iterations followed by a sudden drop in energy. During the later stage of the reconstruction process, reduction in energy is harder to achieve by the random movement of a sphere where most of the computational cost is allocated at the later stage of the reconstruction.

As illustrated in **Fig. 3.18c**, the carbon spheres tend to agglomerate together to minimize the statistical information difference between the reconstructed structure and ex-

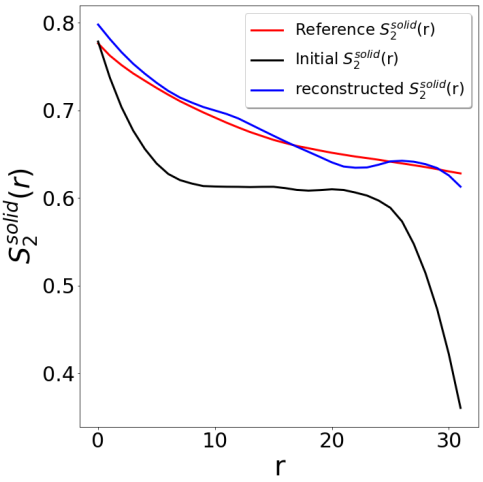

(a) $S_2^{\text{solid}}(r)$ comparison.

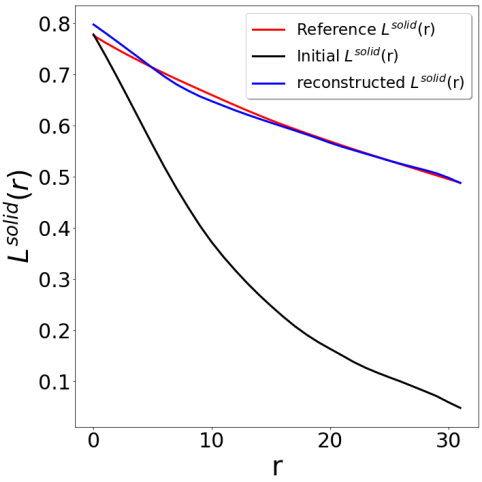

(b) $\text{L}^{\text{solid}}(r)$ comparison.

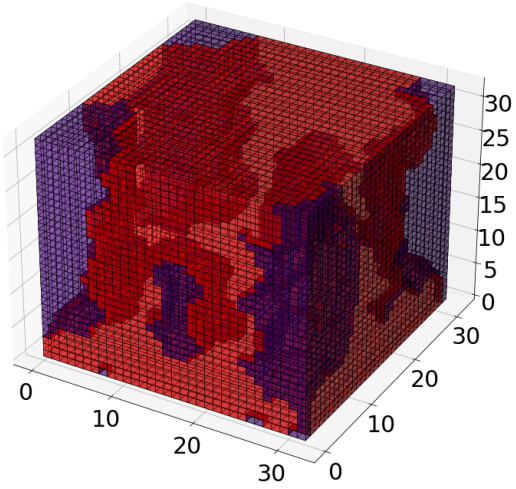

(c) Reconstructed CL structure.

Fig. 3.18: Reconstructed catalyst layer structure: (a) and (b) are the comparison of $S_2^{\text{solid}}(r)$ and $L^{\text{solid}}(r)$ of the reconstructed CL structure with the reference and initial CL structure; (c) Reconstructed CL structure (red is solid, purple is pore).

perimental image. The two-point correlation functions and lineal path functions for the reconstructed CL microstructure are presented in **Fig. 3.18a** and **Fig. 3.18b**. It can be

observed that both $S_2^{\text{solid}}(r)$ and $L^{\text{solid}}(r)$ for the reconstructed microstructure improved significantly from the initial CL microstructure. The Perasons correlation coefficients [106] for the $S_2^{\text{solid}}(r)$ and the $L^{\text{solid}}(r)$ between the reconstructed structure and reference structure are 99.32 % and 99.57 %, respectively. Some slight deviation has been observed at $L^{\text{solid}}(r = 0)$ with a relative error of 2.74 % as illustrated in **Fig. 3.18b**, which is still reasonable. As for the two-point correlation function $S_2^{\text{solid}}(r)$, the maximum relative error still occurs at $r = 0$ which is 2.76 %. The reason why maximum relative errors in $S_2^{\text{solid}}(r)$ and $L^{\text{solid}}(r = 0)$ both occur at $r = 0$ is that the random displacement of the sphere inside the domain would change the volume fraction of the solid phase ϕ_{solid} to reduce the energy residual elsewhere ($r = 1, 2, \ldots, 32$).

To summarize, the CL has been successfully reconstructed based on the sphere-based hybrid reconstruction method proposed in this thesis research. Good agreement has been observed between the reconstructed microstructure and experimental microstructure provided by Toray Japan in terms of statistical information. In the next section, the solid phase would be segmented into the ionomer phase and the Pt/C agglomerate phase preparing for the delamination model described in the Chapter 4.

3.3.5 Module 3 Segmentation

After the reconstruction, a segmentation method for the solid phase has been used to differentiate the Pt/C and the ionomer phase. In this model, the ionomer is assumed to be uniformly covering the Pt/C agglomerate and the Pt/C is assumed to be perfectly spherical. The detailed algorithm is shown in **Fig. 3.19**. An initial guess of the Pt/C

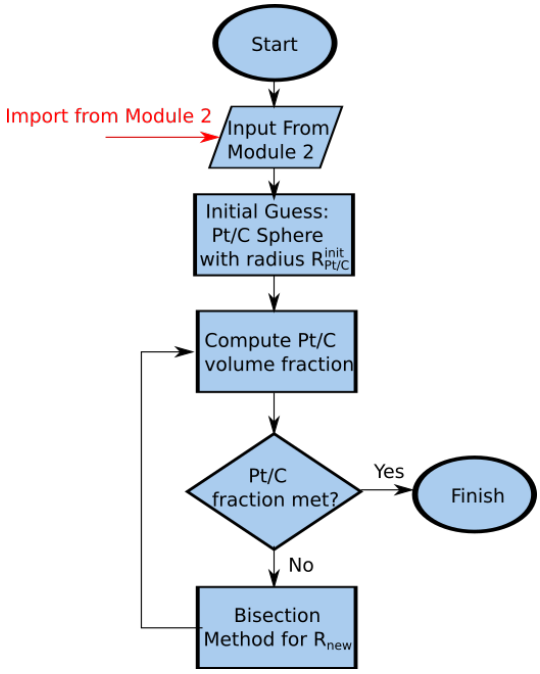

Fig. 3.19: Schematic flowchart for the Module 3 Segmentation algorithm.

agglomerate radius has been chosen $R^{\text{init}}_{\text{Pt/C}}$. The volume fraction of the guessed Pt/C phase $\phi_{\text{Pt/C}}$ is calculated and compared with the Pt/C fraction $\phi^{\text{ref}}_{\text{Pt/C}}$ of the experimental image from Toray. The relative error between $\phi_{\text{Pt/C}}$ and $\phi^{\text{ref}}_{\text{Pt/C}}$ is defined as the residual in the segmentation module. Then, the program iteratively finds the radius of the Pt/C agglomerate $R_{\text{Pt/C}}$ to ensure the difference between the $\phi_{\text{Pt/C}}$ and $\phi^{\text{ref}}_{\text{Pt/C}}$ is small and within a tolerance. To the best of author's knowledge, the segmentation process is typically very fast. Therefore, in terms of selecting the proper iteration method, it is suggested to focus more on the robustness and simplicity instead of convergence speed. Therefore, a bisection method [107] has been selected in this thesis research to update the new Pt/C radius until

convergence criteria for segmentation has been met $\varepsilon_{\text{segmentation}}$. The residual is defined as

$$\epsilon^{\text{residual}}_{\text{segmentation}} = \frac{|\phi_{\text{Pt/C}} - \phi^{\text{ref}}_{\text{Pt/C}}|}{\phi^{\text{ref}}_{\text{Pt/C}}} < \varepsilon_{\text{segmentation}} \tag{3.24}$$

where $\epsilon^{\text{residual}}_{\text{segmentation}}$ is the residual for segmentation, $\phi_{\text{Pt/C}}$ the volume fraction of Pt/C for the current iteration, $\phi^{\text{ref}}_{\text{Pt/C}}$ the volume fraction of Pt/C for the experimental images and $\varepsilon_{\text{segmentation}}$ the convergence criteria for segmentation.

The input parameters for the module 3 is summarized in **Table. 3.4**. The reference Pt/C volume fraction $\phi^{\text{ref}}_{\text{Pt/C}}$ is extracted from the experimental image shown in **Fig. 3.10b**. It is simply the addition of the platinum volume fraction ϕ_{platinum} and the carbon volume fraction ϕ_{carbon}.

Table 3.4: Input parameters for Module 3 Segmentation

Parameters	Symbol	Value	Units
Input Parameters			
Reference Pt/C Volume Fraction	$\phi^{\text{ref}}_{\text{Pt/C}}$	0.6336	-
Initial Pt/C radius guess	$R^{\text{init}}_{\text{Pt/C}}$	2.5	Voxels
Convergence Criteria	$\varepsilon_{\text{segmentation}}$	0.01	-

The converged segmented CL structure is shown in **Fig. 3.20**. It could be observed that the ionomer forms a network to provide protonic pathway. The carbon spheres form into Pt/C agglomerates to provide reaction sites for the electrochemical reactions. The interface between the ionomer thin layer and the Pt/C agglomerate is the interest of this current thesis research and it will be elaborated in Chapter 4 and 5.

Although the statistical correlation functions for the solid phase of the CL has been verified as discussed in **section 3.3.4**, the segmented CL microstructure doesn't contain

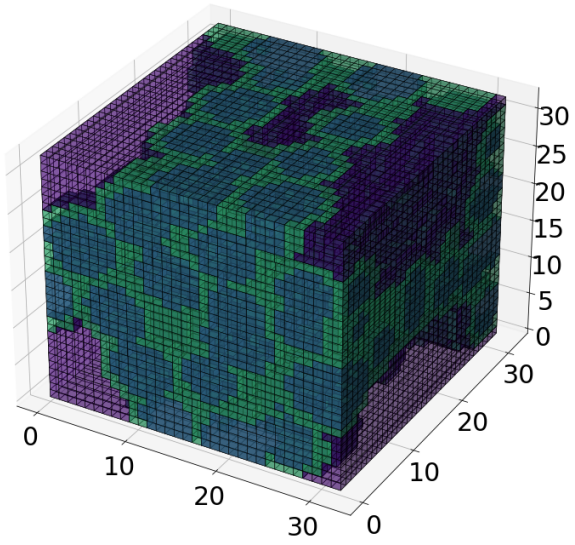

Fig. 3.20: The reconstructed and segmented CL structure with pore phase in purple, Pt/C phase in blue and the ionomer in green.

high-order statistical information such as the two-point correlation function and the lineal path function for the ionomer phase. The reconstructed and segmented ionomer phase just contains the low-order statistical information such as the ionomer volume fraction ϕ_{ionomer}. It is because the input image used for reconstruction is a binary image consisting of solid and pore, as shown in **Fig. 3.12** which only contains information for solid and pore phase. After reconstruction, the solid phase is segmented to the ionomer phase and the Pt/C agglomerate phase based on its volume fraction. Therefore, it does not contain high-order statistical information for the ionomer and the Pt/C agglomerate phase.

3.4 Summary

In Chapter 3, the theory of statistical characterization of microstructure images, including the two-point correlation and lineal path functions, has been discussed. The algorithm for computing those functions is elaborated and validated against the existing analytical solution. The hybrid reconstruction method has been developed and programmed. The advantages and disadvantages of the reconstruction method have been discussed.

Chapter 4

Delamination Model Development

In this chapter, a three-dimensional delamination model will be developed to study the microstructure changes focusing on the interface delamination between the catalyst agglomerate and the ionomer. Delaminated ionomer thin-film cuts off the supply of protons to the platinum reaction sites, leading to unsuccessful oxygen reduction reaction and hence performance loss. This chapter provides the essential information about the physical models, assumptions, model formulations, material properties, boundary conditions, numerical procedure as well as numerical implementation. Validation of the material properties is conducted against the experimental data available in literature.

4.1 Physical Model

The reconstructed catalyst layer consists of the ionomer phase, the Pt/C agglomerate phase and the pore phase. Because of limitation in computational resources, only a sub-

domain of the reconstructed catalyst layer is used for the structure model. **Fig. 4.1** shows a sub-domain (one-eighth) of the reconstructed catalyst layer employed for the numerical analysis. It is computationally inefficient to conduct numerical analysis on the full domain. The standard modus operandi for studying microstructure is to utilize RVE with periodic boundary conditions to numerically simulate and investigate the deformation behavior of the systems [108, 109].

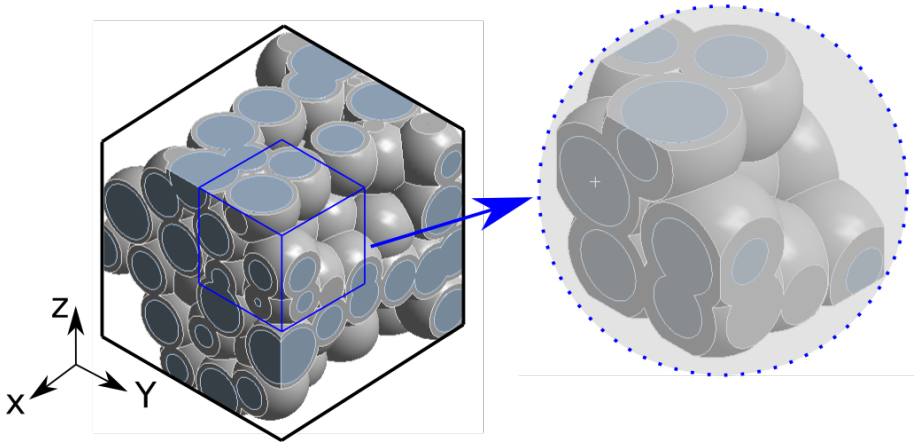

Fig. 4.1: A schematic drawing of the reconstructed catalyst layer from the previous reconstruction process and one-eighth of the microstructure reconstructed in the previous chapter is chosen as the representative volume element for the delamination study hereafter.

This implementation allows investigation of the stress and strain field and delamination behaviour of the CL in a computationally inexpensive manner at the same mesh density. However, the periodic boundary conditions usually set up in a way to ensure all the RVEs deform identically, and hence the edge and boundary effect is entirely removed and the system is an infinite system [110]. In reality, the catalyst layer has edges and boundaries (a finite system), and the deformation behaviour would be different from those of the finite system. In this analysis, there is order of magnitude difference in dimension between the

RVE and the entire CL. The total number of internal units is much higher than the boundary units. It is arguable that the deformation of a finite system with many internal units compared to boundary units is similar to the deformation of an infinite system [110, 111]. Therefore, one-eighth of the reconstructed domain has been used as RVE with periodic boundary conditions to investigate the delamination and deformation behaviour of the entire system using reasonable computational resources.

4.2 Assumptions

Without losing major characteristics of the delamination behavior, some major assumptions are summarized as follows:

- All material properties are assumed to be isotropic including the ionomer swelling and thermal expansion. Pt/C agglomerate is assumed to be elastic since Young's modulus for the Pt/C agglomerate's is much higher than the ionomer [13, 14].
- Humidity gradient and temperature gradient inside the reconstructed catalyst layer are ignored. Since the scale of the geometry is small, it is reasonable to assume the temperature and relative humidity increases uniformly from ambient condition to operating condition [15, 82–84].
- The ionomer material properties used in this thesis research is the bulk ionomer. In reality, polymer physical properties vary from bulk ionomer to thin-film and to polytetrafluoroethylene (PTFE) lattice and chain due to confinement effect [112].

However, due to lack of experimental apparatus, the humidity and temperature dependent stress-strain response for nano-scale ionomer is not available in literature. Therefore, ionomer bulk properties have been used in this thesis research.

4.3 Governing Equations

4.3.1 Force Balance Equations

To obtain the force balance equations for a deformable solid body, the general state of stress at an arbitrary point in the body is examined via balancing the external load with internal stress. Applying the condition of force balance to an infinitesimal element of the solid body results in the equations shown below [113]

$$\frac{\partial \sigma_{ij}}{\partial x_i} + b_i = 0 \tag{4.1}$$

where σ_{ij} is the Cauchy stress tensor and b_i the body force per unit volume.

4.3.2 Strain-displacement Equations

Due to the non-linear behaviour of the ionomer and dynamic fuel cell operating condition, the small strain assumption typically encountered in engineering analysis is no longer valid. In contrast to linear elasticity, many different ways are proposed in the non-linear continuum mechanics to describe the relationship between the strain and the displacement. Despite many other proposed strain measure theories, the green strain theory is adopted

here because it is widely used and implemented in finite element methods. The green strain theory consists of a linear term and a quadratic term and is defined below [114]

$$\epsilon_{ij} = \frac{1}{2}\left(\frac{\partial u_i}{\partial x_j} + \frac{\partial u_j}{\partial x_i}\right) + \frac{1}{2}\left(\frac{\partial u_k}{\partial x_i}\frac{\partial u_k}{\partial x_j}\right) \tag{4.2}$$

where ϵ_{ij} the strain tensor, u_i the displacement in the spatial coordinate direction x_i.

4.3.3 Constitutive Equations

Pt/C agglomerate

For the current study, the Pt/C agglomerate is assumed to be isotropic and elastic since it is mechanically stronger than the ionomer [13, 15, 87].

Pt/C agglomerate's elastic behavior is characterized with Hooke's law [83] such that

$$\epsilon_{ij}^{E} = \frac{1}{E}\left[\sigma_{ij} - \nu\left(\sigma_{kk}\delta_{ij} - \sigma_{ij}\right)\right] \tag{4.3}$$

where E and ν are Young's modulus and Poission's ratio respectively, σ_{kk} the trace of σ_{ij} ($\sigma_{kk} = \sigma_{11} + \sigma_{22} + \sigma_{33}$), δ_{ij} the Kronecker delta and ϵ_{ij}^{E} the elastic strain.

Ionomer

The ionomer material properties are hygrothermally and temporally dependent as determined experimentally [115–118]. An uncoupled theory of strain tensor has been deployed where the incremental strain due to other strain component is negligible. The strain tensor

is additively decomposed into [83, 119]

$$\epsilon_{ij} = \epsilon_{ij}^{M} + \epsilon_{ij}^{T} + \epsilon_{ij}^{S} \tag{4.4}$$

where ϵ_{ij}^{M} is the mechanical strain, ϵ_{ij}^{T} and ϵ_{ij}^{S} are the strain induced by the variations in temperature and humidity, respectively.

The ϵ_{ij}^{T} and ϵ_{ij}^{S} are calculated as [119]

$$\epsilon_{ij}^{T} = \alpha \left(T - T_0\right) \delta_{ij} \tag{4.5}$$

$$\epsilon_{ij}^{S} = \beta \left(RH - RH_0\right) \delta_{ij} \tag{4.6}$$

where T_0 and RH_0 are the reference temperature and relative humidity at room condition, respectively. T and RH are the temperature and relative humidity of the ionomer during fuel cell operation.

Due to ionomer's dependence on different strain rates, an elasto-viscoplastic (evp) formulation has been used to capture its constitutive response [120], its one-dimensional rheological model is shown in **Fig. 4.2**. The spring, slider and dash-pot elements characterize the linear elastic, isotropic hardening and viscous responses, respectively.

The mechanical strain tensor ϵ^{M} is the summation of elastic and viscoplastic component

$$\epsilon_{ij}^{M} = \epsilon_{ij}^{E} + \epsilon_{ij}^{\mathrm{VP}} \tag{4.7}$$

where the elastic strain ϵ_{ij}^{E} follows the Hooke's law as represented by Eq. (3) for the Pt/C

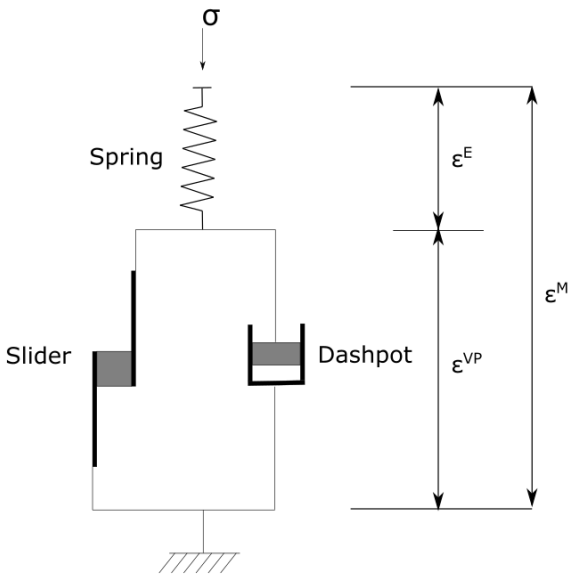

Fig. 4.2: Elasto-viscoplastic (evp) rheological model used in this study for the ionomer in the catalyst layers.

agglomerate, and $\epsilon_{ij}^{\mathrm{VP}}$ is the equivalent viscoplastic strain, defined as [83]

$$\epsilon_{ij}^{\mathrm{VP}} = \int_0^{t_f} \sqrt{\frac{2}{3}\dot{\epsilon}_{ij}\dot{\epsilon}_{ij}}dt \tag{4.8}$$

where $\dot{\epsilon}_{ij}$ is the strain rate.

The effect of strain rate on yield strength of the material is expressed by elasto-viscoplastic model with Peirce formulation as follows [121]

$$\dot{\epsilon}_{ij} = \gamma \left(\frac{\sigma_y}{\sigma_y^0} - 1 \right)^{1/m} \tag{4.9}$$

where γ is the material viscosity parameter and m is the strain rate parameter. σ_y is the rate-dependent yield strength and it is sensitive to different strain rates. σ_y^0 is the rate-

independent yield strength where the strain rate applied is infinitely small. Therefore, σ_y converges to σ_y^0 when strain rate is infinitely small (quasi-static loading).

Viscoplasiticy could be modeled by incorporating the rate-dependency in von-mises yield function [122]. The Pierce formulation [120] incorporated in von-mises yield function is

$$f(\sigma_{ij}) = \sqrt{\frac{3}{2}\sigma_{ij}^{\text{Dev}}\sigma_{ij}^{\text{Dev}}} - \sigma_y^0 \left(1 + \frac{\dot{\epsilon}_{ij}}{\gamma}\right)^m \tag{4.10}$$

where σ_{ij}^{Dev} is the deviatoric stress tensor components.

The deviatoric stress tensor σ_{ij}^{Dev} is a component of the Cahchy stress tensor σ_{ij} responsible for the shape change of an infinitesimally small element. The other component of σ_{ij} is the hydrostatic stress σ^{Hyd}, which is the average of the normal stress components of the Cauchy stress and is related to the volume change of an element. The hydrostatic stress σ^{Hyd} is a scalar quantity but often written in tensor form σ_{ij}^{Hyd}. These definitions are given below [114]

$$\sigma_{ij}^{\text{Dev}} = \sigma_{ij} - \sigma_{ij}^{\text{Hyd}} \tag{4.11}$$

$$\sigma_{ij}^{\text{Hyd}} = \begin{bmatrix} \sigma^{\text{Hyd}} & 0 & 0 \\ 0 & \sigma^{\text{Hyd}} & 0 \\ 0 & 0 & \sigma^{\text{Hyd}} \end{bmatrix} \tag{4.12}$$

$$\sigma^{\text{Hyd}} = \frac{1}{3}\sigma_{kk} \tag{4.13}$$

where σ_{kk} is the trace of the σ_{ij}.

Interface Model

In order to numerically simulate the interface delamination, two commonly used approaches are the Virtual Crack Closure Technique (VCCT) [121] and Cohesive Zone Method (CZM) [123]. The cohesive zone method is adopted here to study the interfacial delamination since it avoids difficulties in VCCT such as dynamic remeshing in delamination propagation to recompute fracture parameters [15, 123]. The CZM approach assumes a Cohesive Damage Zone develops near the tip of a crack. The Cohesive Damage Zone allows and extends the classical continuum approach to capture fracture process [123].

In this work, a bilinear constitutive relationship is adopted to characterize the delamination process as illustrated in **Fig. 4.3a**. The bilinear model consists of a linear elastic stiffening region with stiffness K and a linear softening region. Before the initiation of a crack, the cohesive model is assumed to be linear elastic until traction exceeds the interfacial strength τ_i^0 where the delamination initiates. As the delamination propagates, the traction force decreases as a function of separation displacement which is known as the linear softening region. The area under the curve is the fracture energy G_i, a measure of fracture toughness usually measured experimentally.

As briefly mentioned in **Section** 2.2.2, there are three modes of fracture including normal mode, in-plane shear mode and out-of-plane shear mode. Under loading condition, the delamination process is the combination of three fundamental modes. For the present study, the out-of-plane mode is assumed to behave the same as the in-plane shear mode. The mixed mode of fracture is adopted for the work as schematically shown in **Fig. 4.3b**.

Onset of interface delamination is modelled with cohesive zone method that makes

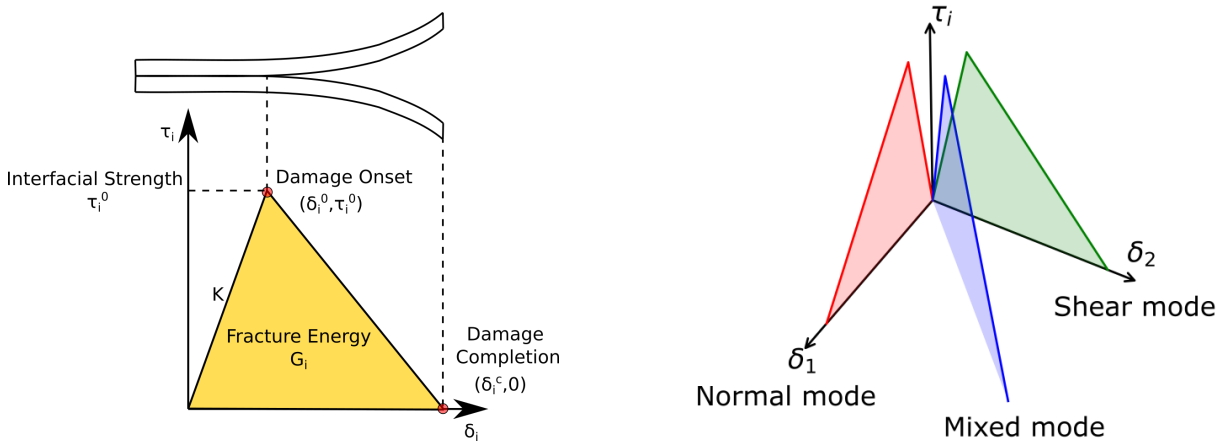

(a) Single mode.

(b) Mixed mode.

Fig. 4.3: Schematic of bilinear constitutive relationship used in the present analysis: (a) single mode; (b) mixed mode combining normal and shear mode

use of interface finite element to characterize the constitutive behavior of the damage interface [124]. The interface constitutive relationship between the traction vector τ_i and the displacement vector δ_i could be written as

$$\begin{bmatrix} \tau_1 \\ \tau_2 \\ \tau_3 \end{bmatrix} = \begin{bmatrix} (1-D)\,K + DKH\,(-\delta_1) & 0 & 0 \\ 0 & (1-D)\,K & 0 \\ 0 & 0 & (1-D)\,K \end{bmatrix} \begin{bmatrix} \delta_1 \\ \delta_2 \\ \delta_3 \end{bmatrix} \tag{4.14}$$

The subscript 1 2 and 3 for τ_i and δ_i stands for the traction and separation vector for three modes of fracture and they are in-plane normal, in-plane shearing and out-of-plane shearing, respectively. In **Eq. 4.14**, K stands for the initial stiffness of the interface element before damage onset. H stands for the Heaviside function (H(x) = 1 if x>0) to eliminate

interpenetration between the interface elements. The damage parameter D ranging from 0 (damage onset) to 1 (damage completion) characterizing the extent of damage is written as follows

$$D(\delta_i) = \begin{cases} 0 & \delta_i < \delta_i^0 \\ \frac{\delta_i^c(\delta_i - \delta_i^0)}{\delta_i(\delta_i^c - \delta_0^0)} & \delta_i^0 \leq \delta_i \leq \delta_i^c \\ 1 & \delta_i > \delta_i^c \end{cases} \tag{4.15}$$

where δ_i^0 is the displacement at the cohesive interfacial strength, δ_i^c the displacement at the completion of delamination.

A mixed-mode non-dimensional displacement jump λ_m to measure the interface displacement in mixed mode is defined as [121, 125]

$$\lambda_m = \sqrt{\left(\frac{\delta_1}{\delta_1^c}\right)^2 + \beta^2\left(\frac{\delta_2}{\delta_2^c}\right)^2 + \beta^2\left(\frac{\delta_3}{\delta_3^c}\right)^2} \tag{4.16}$$

where the non-dimensional weighting parameter β is representing different weighting for each fracture mode and β is usually set to one standing for equal contribution of three modes of fracture [125].

The damage parameter D_m associated with the mixed mode bilinear cohesive law is defined as

$$D_m = \begin{cases} 0 & \lambda_m \leq \lambda_{cr} \\ \min(1, \eta\frac{\lambda_m - \lambda_{cr}}{\lambda_m}) & \lambda_m > \lambda_{cr} \end{cases} \tag{4.17}$$

where λ_{cr} is the non-dimensional critical displacement in the mixed mode which represents the onset of delamination in the mixed mode, and η the intermediate variable. These

parameters are defined as [121]

$$\lambda_{cr} = \frac{\delta_1^0}{\delta_1^c} = \beta\frac{\delta_2^0}{\delta_2^c} = \beta\frac{\delta_3^0}{\delta_3^c}$$
$$\eta = \frac{\delta_1^c}{\delta_1^c - \delta_1^0} = \frac{\delta_2^c}{\delta_2^c - \delta_2^0} = \frac{\delta_3^c}{\delta_3^c - \delta_3^0}$$

where δ_1^0, δ_2^0 and δ_2^0 are the displacement at the normal, in-plane shear and out-of-plane shear interfacial strength, respectively, δ_1^c, δ_2^c and δ_3^c are the displacement at the completion of normal, in-plane shear and out-of-plane shear fracture, respectively.

The two surfaces in contact could carry shear stresses and the effect of friction at the contact surfaces is considered by using the Coulomb friction model [126]. Relative sliding motion will occur at the contacting surfaces when the shear stress exceeds the limit value τ_{lim}, defined as [13, 15, 121]

$$\tau_{lim} = \mu P + P_0 \tag{4.18}$$

where μ is the friction coefficient, P the contact pressure and P_0 the cohesion sliding resistance.

4.4 Material Properties

The isotropic linear elastic and plastic properties of Nafion 211 have been experimentally measured by Lu et al. [116] at selected strain rates at various temperature and humidity

values. The Young's modulus E, rate-independent yield strength σ_y^0 and tangent modulus H_0 at selected temperature and humidity values are listed in Table 1. As for the the rate-dependent elasto-viscoplastic behavior, the material strain rate hardening parameter m and viscosity parameter γ are calculated via curve fitting with non-linear least square fitting the yield strength at different strain rates of 0.2 $[min^{-1}]$ and 5 $[min^{-1}]$ [116]. The thermal and swelling coefficients are obtained from [119]. At small strains, the Poisson ratio ν is not sensitive to varying water content and temperature and it is taken to be 0.4 [127]. The Pt/C agglomerate is mechanically stronger than ionomer and is considered as elastic material with the Young's modulus of 4800 MPa [13].

Table 4.1: Material properties for Nafion 211: E, σ_y^0 and H_0 are taken from [116] and m and γ are determined in the present study based on Peirce viscoplastic model in accordance with the experimental results [116].

	E [MPa]	σ_y^0 [MPa]	H_0 [MPa]	m	γ
$25°C$ and 30%	270	4.78	15.6	7.64E-02	6.79E-08
$45°C$ and 50%	215	2.29	6.1	8.52E-02	2.52E-09
$65°C$ and 70%	110	1.15	3.5	1.12E-01	6.92E-09
$80°C$ and 90%	65	0.59	1.9	8.9E-02	2.51E-12

The fracture material properties for out-of-plane shear is assumed to be the same as in-plane shear due to lack of experimental studies. In order to model the mixed-mode fracture, the normal strength τ_n^0, the normal displacement at the completion of delamination δ_1^c, the shear strength τ_2^0, the tangential displacement at the completion of delamination δ_2^c, the ratio $\frac{\delta_n^0}{\delta_n^c}$ and non-dimensional weighting parameter β need to be determined. The fracture toughness for mode I (normal) G_I and mode II (shear) G_{II} are taken as 27 J/m^2 [79] and 900 J/m^2 [73], respectively at $25°C$ and 30% relative humidity. At atomic scale, the normal strength of the interface τ_1^0 is taken to be E/10 where E is the Young's modulus

of the ionomer [13, 15, 82]. The normal and shear strength are proportional to the normal and shear fracture toughness defined as [82, 128]

$$\tau_2^0 = \tau_1^0 \sqrt{\frac{G_{II}}{G_I}} \tag{4.19}$$

The other parameters are calculated from the fracture toughness and interfacial strength for the bilinear CZM model and given in **Table 4.2**. It is noted that the non-dimensional weighing parameter β between the shear mode and normal mode is taken as unity due to the lack of information in literature.

Table 4.2: Fracture material properties: G_I [79] and G_{II} [73] are taken from experimental studies. τ_1^0, τ_2^0, δ_1^c, δ_1^c, $\frac{\delta_1^0}{\delta_1^c}$ and β the properties used in the present CZM analysis, determined from the data in studies [73, 79, 82].

	$G_I[J/m^2]$	$G_{II}[J/m^2]$	$\tau_1^0[MPa]$	$\tau_2^0[MPa]$	$\delta_1^c[um]$	$\delta_2^c[um]$	$\frac{\delta_1^0}{\delta_1^c}$	β
$25°C$ and 30%	27	900	27	155.88	2.00	11.55	0.2	1
$45°C$ and 50%	24	716.67	21.50	117.49	2.23	12.20	0.2	1
$65°C$ and 70%	21	533.33	11	55.43	3.82	19.24	0.2	1
$80°C$ and 90%	18	350	6.50	28.66	5.54	24.42	0.2	1

As for the frictional contact model, the frictional coefficient is dependent on shearing rates. For the current study, the frictional coefficient μ of 0.2 has been selected due to low loading rate [13] encountered. The cohesion sliding resistance P_0 is assumed as zero due to lack of experimental studies.

Table 4.3: Boundary conditions applied to the computational domain to ensure proper periodicity.

Component	Boundary Condition Type	Details
Surface 1234	Fixed displacement	UY=0, Free UX, Free UZ
Surface 1265	Fixed displacement	UX=0, Free UY, Free UZ
Surface 2376 (bot)	Fixed displacement	UZ=0, Free UX, Free UY
Surface 5678	Coupled displacement	Free UX, Free UZ, UY is same for all nodes on surface
Surface 3287	Coupled displacement	Free UY, Free UZ, UX is same for all nodes on surface
Surface 1384 (top)	Coupled displacement	Free UX, Free UY, UZ is same for all nodes on surface
Surface 1384 (top)	Pressure	Constant clamping stress of 1 MPa

4.5 Boundary and Operating Condition

The implementation of boundary conditions to ensure symmetry is a crucial step for the reconstructed catalyst layer in a periodic unit cell to be representative enough for the entire catalyst layer. Mizzi *et al.* proposed a set of boundary conditions for microstructure to ensure the proper deformation under loading [110] as illustrated in **Fig. 4.4**. Their proposed boundary conditions are adopted for the thesis work and details about boundary condition is listed in **Table 4.4**. A constant clamping stress of 1 MPa is applied at the top surface of the computational domain.

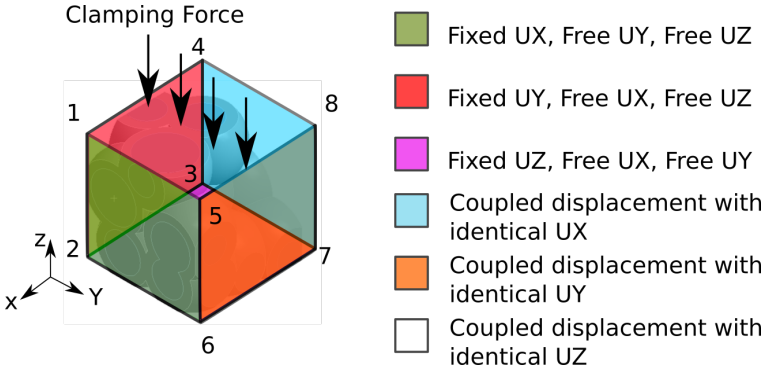

Fig. 4.4: Schematic showing the boundary condition implementation for reconstructed catalyst layer as a periodic unit cell.

PEM fuel cell operation includes start-up, driving, shut-down and parking, as shown schematically in **Fig. 4.5**. The relative humidity and temperature ramps up during start-up, decreases during shut-down and remains relatively stable at peak value during driving. The constant clamping stress is applied and will vary due to shrinkage and expansion during operating cycles [85].

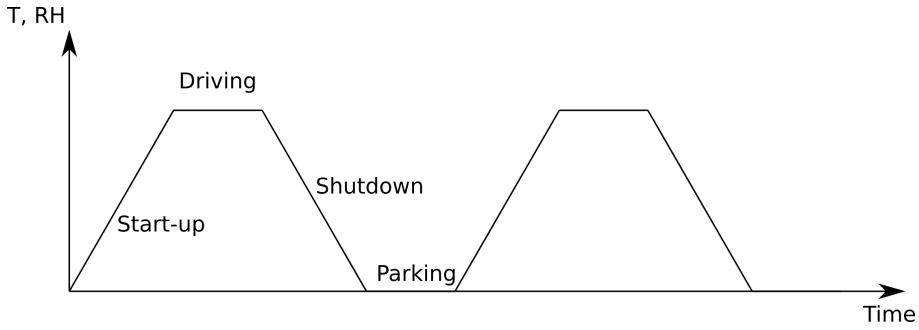

Fig. 4.5: The profile of humidity and temperature changes a PEM fuel cell is considered experiencing during vehicle driving cycles

The initial and operating conditions for the current model have been applied in accordance with the driving cycles. The initial and operating condition applied during hygrothermal cycles is

- *Initial conditions*: T = 25 $^{\circ}C$ and 30 % RH.
- *Operating conditions*: T = 85 $^{\circ}C$ and 90 % RH.

During the fuel cell operation, the condition applied for the analysis involves: A ramped temperature and relative humidity are applied uniformly to the ionomer in accordance with a driving profile between T = 25 $^{\circ}C$ and RH = 30 % and T = 85 $^{\circ}C$ and RH = 90 %; the specific profile will be provided before the results are presented.

4.6 Numerical Implementation

In this section, the detailed numerical implementation of the delamination model is presented with a focus on (i) the numerical procedure, (ii) the mesh settings , and (iii) the grid independency study.

4.6.1 Numerical Procedure

Updated Lagrangian Formulation

The governing equations of the delamination model are discretized and solved in CSM software, ANSYS Mechanical, based on the FEM. Due to the presence of geometric non-linearity in this model, the Cauchy stress cannot be simply updated by its increment directly [121]. In this thesis research, the formulation used is ULM. The unique feature of ULM is that all the derivatives are with respect to the current (deformed) coordinates instead of the initial (undeformed) coordinates. Based on the principle of virtual work, the force-balance equation could be written into the following form [114]

$$\int_{{}^{t}\mathrm{V}} {}^{t+\Delta t}_{t}\mathrm{P}_{ij}\,\delta\,{}^{t+\Delta t}_{t}\varepsilon_{ij}\,\mathrm{d}\,{}^{t}\mathrm{V} = {}^{t+\Delta t}\mathscr{R} \tag{4.20}$$

where P_{ij} is the second Piola-Kirchhoff stress, ${}^{t+\Delta t}_{t}\mathrm{S}_{ij}$ the second Piola-Kirchhoff stress at time $t+\Delta t$ with respect to configuration at t, ε_{ij} the strain, $\delta\varepsilon_{ij}$ the infinitesimally small increment of strain ε_{ij}, ${}^{t+\Delta t}\mathscr{R}$ the external work done to the system by the external load at time $t+\Delta t$ and $\int_{{}^{t}\mathrm{V}}\mathrm{dV}$ is integration over the volume ${}^{t}\mathrm{V}$ with respect to configuration at t. It should be noted that the second Piola-Kirchhoff stress P_{ij} is the energy conjugate

of the strain ε_{ij}.

The term ${}^{t+\Delta t}_{t}\mathrm{P}_{ij}$ and ${}^{t+\Delta t}_{t}\varepsilon_{ij}$ is decomposed into a known part and an unknown part shown below

$$ {}^{t+\Delta t}_{t}\mathrm{P}_{ij} = {}^{t}_{t}\mathrm{P}_{ij} + {}_{t}\mathrm{P}_{ij} = {}^{t}\sigma_{ij} + {}_{t}\mathrm{P}_{ij} \tag{4.21} $$

$$ {}^{t+\Delta t}_{t}\varepsilon_{ij} = {}^{t}_{t}\varepsilon_{ij} + {}_{t}\varepsilon_{ij} = {}_{t}\varepsilon_{ij} \tag{4.22} $$

where ${}^{t}_{t}\mathrm{P}_{ij}$ is the second Piola-Kirchhoff at time t with respect to the configuration at time t which is equivalent to the Cauchy stress tensor σ_{ij} at time t, ${}_{t}\mathrm{P}_{ij}$ the increment of second Piola-Kirchhoff at time t, ${}^{t}_{t}\varepsilon_{ij}$ the strain at time t with respect to the configuration at time t which is equivalent to zero and ${}_{t}\varepsilon_{ij}$ the increment of strain at time t.

Previously described in **Equ. 4.2**, the strain ε_{ij} could be decomposed into a linear term and a quadratic term based on the green strain theory [114]. Similarly, the increment of strain ${}_{t}\varepsilon_{ij}$ is decomposed into a linear term and a quadratic term

$$ {}_{t}\varepsilon_{ij} = {}_{t}e_{ij} + {}_{t}\eta_{ij} \tag{4.23} $$

where the linear term ${}_{t}e_{ij}$ and quadratic term ${}_{t}\eta_{ij}$ are related back to the derivative of the displacement

$$ {}_{t}e_{ij} = \frac{1}{2}({}_{t}u_{i,j} + {}_{t}u_{j,i}) \tag{4.24} $$

$$ {}_{t}\eta_{ij} = \frac{1}{2}{}_{t}u_{k,i}\,{}_{t}u_{k,j} \tag{4.25} $$

Substitute **Equ. 4.21-4.23** into **Equ. 4.20** yields the equation of the principle of virtual work is transformed into

$$\int_{{}^t\mathrm{V}} {}_t\mathrm{P}_{ij}\,\delta\,{}_t\varepsilon_{ij}\,\mathrm{d}\,{}^t\mathrm{V} + \int_{{}^t\mathrm{V}} {}^t\sigma_{ij}\,\delta\,{}_t\eta_{ij}\,\mathrm{d}\,{}^t\mathrm{V} = {}^{t+\Delta t}\mathscr{R} - \int_{{}^t\mathrm{V}} {}^t\sigma_{ij}\,\delta\,{}_te_{ij}\,\mathrm{d}\,{}^t\mathrm{V} \tag{4.26}$$

The **Equ. 4.26** is highly non-linear and linearization needs to be performed. Linearizing the first term and substituting the constitutive equations, the resulting equation is shown below

$$\int_{{}^t\mathrm{V}} {}_t\mathrm{C}_{ijrs}\ {}_te_{rs}\delta\,{}_te_{ij}\,\mathrm{d}\,{}^t\mathrm{V} + \int_{{}^t\mathrm{V}} {}^t\sigma_{ij}\,\delta\,{}_t\eta_{ij}\,\mathrm{d}\,{}^t\mathrm{V} = {}^{t+\Delta t}\mathscr{R} - \int_{{}^t\mathrm{V}} {}^t\sigma_{ij}\,\delta\,{}_te_{ij}\,\mathrm{d}\,{}^t\mathrm{V} \tag{4.27}$$

where ${}_tC_{ijrs}$ is the material constant fourth order tensor with respect to the configuration at time t.

The equation derived by the ULM is written into incremental form suitable for modified Newton-Raphson procedure

$$\int_{{}^t\mathrm{V}} {}_t\mathrm{C}_{ijrs}\,\Delta\,{}_te^k_{rs}\delta\,{}_te_{ij}\,\mathrm{d}\,{}^t\mathrm{V} + \int_{{}^t\mathrm{V}} {}^t\sigma_{ij}\,\delta\Delta\,{}_t\eta_{ij}\,\mathrm{d}\,{}^t\mathrm{V} = {}^{t+\Delta t}\mathscr{R} - \int_{{}^{t+\Delta t}\mathrm{V}^{k-1}} {}^{t+\Delta t}\sigma^{k-1}_{ij}\delta\,{}_{t+\Delta t}e^{k-1}_{ij}\,\mathrm{d}\,{}^{t+\Delta t}\mathrm{V} \tag{4.28}$$

where superscript k is the iterator ($k = 1, 2, 3, \dots$) inside a time increment Δt, $\Delta\,{}_te^k_{rs}$ and $\Delta\,{}_t\eta^k_{rs}$ are the increments of linear term and quadratic term in the strain tensor ${}_t\epsilon_{ij}$, respectively.

The displacement increment equation and the initial conditions are

$$ {}^{t+\Delta t}u_i{}^{k} = {}^{t+\Delta t}u_i{}^{k-1} + \Delta u_i^k \tag{4.29} $$

$$ {}^{t+\Delta t}u_i{}^{0} = {}^{t}u_i, \quad {}^{t+\Delta t}\sigma_{ij}{}^{0} = {}^{t}\sigma_{ij}, \quad {}^{t+\Delta t}e_{ij}{}^{0} = {}^{t}e_{ij} \tag{4.30} $$

Finite Element Discretization

The **Equ. 4.28** is discretized with FEM into the following matrix form [114]

$$ {}^{t}_{t}\underline{\mathrm{K}}\Delta\underline{\mathrm{U}}^{k} = {}^{t+\Delta t}\underline{\mathrm{R}} - {}^{t+\Delta t}_{t+\Delta t}\underline{\mathrm{F}}^{\mathrm{k-1}} \tag{4.31} $$

where ${}^{t}_{t}\underline{\mathrm{K}}$ is the stiffness matrix of the system at time t with respect to the configuration at time t, $\Delta\underline{\mathrm{U}}^{k}$ the increment in nodal points displacement matrix in iteration k, ${}^{t+\Delta t}\underline{\mathrm{R}}$ the nodal points force matrix corresponding to the external stresses at time $t+\Delta t$, ${}^{t+\Delta t}_{t+\Delta t}\underline{\mathrm{F}}^{\mathrm{k-1}}$ the nodal points force matrix corresponding to the internal stresses at time $t+\Delta t$ with respect to the configuration at time $t+\Delta t$ in iteration step $k-1$ and k is the iterator $k = 1, 2, 3, \ldots, k_{max}$.

The nodal points displacement matrix at time step $t+\Delta t$ is solved by iteratively adding some displacement increment ΔU from the equation shown below

$$ \begin{aligned} {}^{t+\Delta t}\underline{\mathrm{U}}^{k} &= {}^{t}\underline{\mathrm{U}} + \sum_{j=1}^{k} \Delta\underline{\mathrm{U}}^{j} \\ &= {}^{t+\Delta t}\underline{\mathrm{U}}^{k-1} + \Delta\underline{\mathrm{U}}^{\mathrm{k}} \end{aligned} \tag{4.32} $$

where $\underline{\mathrm{U}}^{k}$ is the nodal points displacement matrix at time t, ${}^{t+\Delta t}\underline{\mathrm{U}}^{k}$ the nodal points

displacement matrix at time $t + \Delta t$.

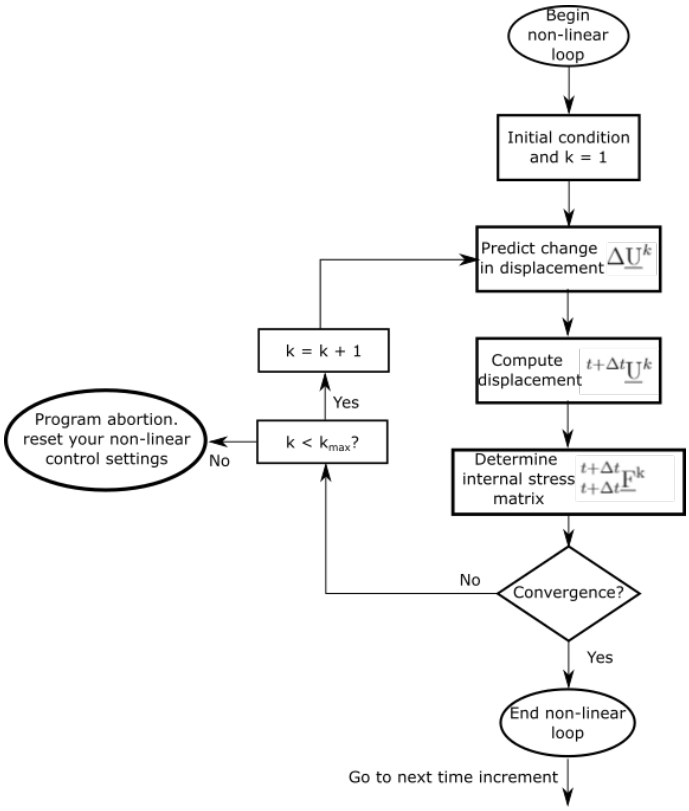

Fig. 4.6: Illustration of modified Newton-Raphson method in updated Lagrangian method based solver in one non-linear inner loop.

The numerical procedure for the ULM based solver is the modified Newton-Raphson method [129] as illustrated in **Fig. 4.6**. It is also commonly referred to the nonlinear inner loop in FEM literature. The major steps for this procedure is outlined as follows:

1. Initialize the computational domain with initial conditions.

2. Predict incremental displacement matrix $\Delta\, \underline{\mathrm{U}}^{\mathrm{k}}$

3. Compute displacement matrix ${}^{t+\Delta t}\underline{\mathrm{U}}^{k}$ in iteration step k

4. Determine ${}^{t+\Delta t}_{t+\Delta t}\underline{\mathrm{F}}^{\mathrm{k}}$ the nodal points force matrix corresponding to the internal stresses at time $t + \Delta t$ with respect to the configuration at time $t + \Delta t$ in iteration step k.

5. Check for convergence by comparing ${}^{t+\Delta t}\underline{\mathrm{R}}$ and ${}^{t+\Delta t}_{t+\Delta t}\underline{\mathrm{F}}^{\mathrm{k}}$. In FEM literature, the difference between these two matrices is usually referred to as "out-of-balance" virtual work term [114]. If convergence has been reached, the model converges at the current time step and moves on the next time increment.

6. If the model does not reach convergence in current iteration k, then the iteration number k is compared with maximum allowable iteration k_{max} to see whether $k > k_{max}$ holds. If not, the model proceeds to next iteration. If yes, it means that the computational model is not stable or the boundaries are ill-conditioned, and it would be erroneous to proceed with the current settings. Some actions are required to modify the settings of the model, such as checking the non-linear control settings, the quality of mesh and ill-constrain of boundary conditions.

As shown in the oscillating cycles in **Fig. 4.7**, the predicted nodal points force matrix due to the internal stresses $\underline{\mathrm{F}}$ keeps on updating until it becomes closer to the nodal points force matrix due to the external stresses $\underline{\mathrm{R}}$ during one inner cycle. The number of maximum iterations allowed for one inner loop is $k_{\max}$.

After the convergence has been reached in the inner loop at time $t + \Delta t$, it moves onto the next inner loop at time $t + 2\Delta t$. It keeps on looping until the convergence has been reached at final time t_{final}.

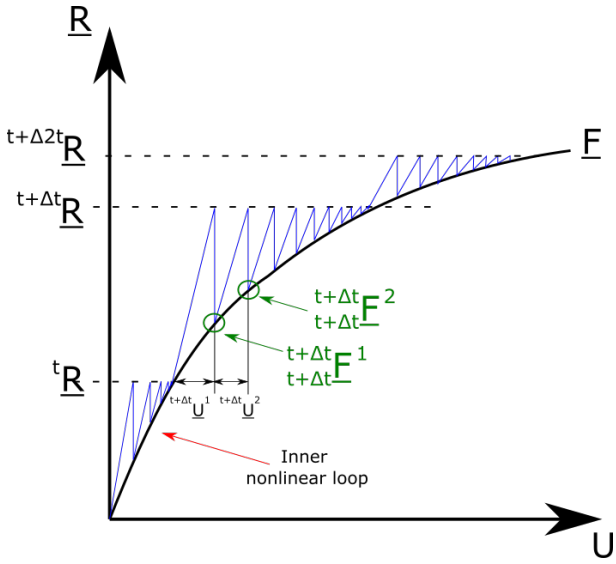

Fig. 4.7: Schematic illustration of nested structure of modified Newton-Raphson method in updated Lagrangian method based solver.

Convergence Criteria and Time Step Setting

The nodal points force matrix corresponding to the external stress ${}^{t+\Delta t}\underline{\mathrm{R}}$ and nodal points force matrix corresponding to the internal stress ${}^{t+\Delta t}_{t+\Delta t}\underline{\mathrm{F}}^{\mathrm{k}}$ are compared to check convergence. Because both matrices have the same size, a convergence criterion is used based on the RMS and RMSE. RMS of a matrix $\underline{A}$ and RMSE of a matrix $\underline{A}$ and $\underline{B}$ of the same size N are

$$\mathrm{RMS}\left(\underline{A}\right) = \sqrt{\sum_{i=1}^{N} \frac{\left(A_i\right)^2}{N}} \tag{4.33}$$

$$\mathrm{RMSE}\left(\underline{A} - \underline{B}\right) = \sqrt{\sum_{i=1}^{N} \frac{\left(A_i - B_i\right)^2}{N}} \tag{4.34}$$

where N is the total number of entries in matrix $\underline{A}$ and $\underline{B}$, A_i and B_i are entries in matrix $\underline{A}$ and $\underline{B}$, respectively.

The convergence criteria used in this delamination model is

$$\frac{\mathrm{RMSE}\left({}^{\mathrm{t}+\Delta\mathrm{t}}\underline{\mathrm{R}} - {}^{t+\Delta t}_{t+\Delta t}\underline{\mathrm{F}}^{\mathrm{k}}\right)}{\mathrm{RMS}\left({}^{\mathrm{t}+\Delta\mathrm{t}}\underline{\mathrm{R}}\right)} < \epsilon_{tol} \tag{4.35}$$

where ϵ_{tol} is the tolerance allowed for convergence.

The proper time step also play a significant role for the delamination model convergence. Ideally, using a small time step would help model convergence, but in return, the demand for computational resources is high. The model described in this chapter is highly non-linear, with both material nonlinearity from the constitutive equations of the ionomer and the geometric nonlinearity from the green strain measure which generally requires a smaller time step for convergence and accuracy. On the other hand, the interest of this thesis research is the deformation and delamination after cyclic loading conditions consisting of many load steps. It demands the time step be larger for reasonable convergence time. Therefore, adaptive time-stepping scheme [130] is employed to ensure accuracy and convergence without wasting too many computational resources. In the early stage of the load step, the load step is divided into more initial substeps (N_{init}) for stability. If the numerical model is stable, a more aggressive time-stepping scheme is used with a minimum substep number and a maximum substep number allowing for one load step. The detailed convergence settings used in this thesis research is summarized in **Table. 4.4**.

More details on the convergence settings can be found in the manual of the FEA software [121]. As for more details on the formulation of ULM and FEM discretization,

Table 4.4: Parameters used in the delamination model for model convergence.

Parameters	Symbols	Value
Convergence Settings		
Convergence tolerance	ϵ_{tol}	$5e^{-3}$
Maximum iteration number	k_{max}	50
Initial subtep number	N_{init}	60
Minimum substep number	N_{min}	20
Maximum substep number	N_{max}	100

further information can be found in several resources [114, 131–133].

4.6.2 Mesh Settings

The CL microstructure consists of the ionomer, Pt/C agglomerate and pore as illustrated in **Fig. 4.8**. Ideally, a fluid-solid coupling model could be conducted to simulate the microstructure deformation. However, for the scope of this thesis research, only the solid domain (the ionomer and the Pt/C agglomerate) is discretized and subsequently solved.

10-Node tetrahedral structural solid elements (SOLID 187) [121] are used to make up the domains of the ionomer and the Pt/C agglomerate. To simulate interface delamination, CZM [121] has been adopted in this thesis research. CZM elements are generally placed at the delamination interface. The interface between the ionomer and the Pt/C agglomerate has been meshed with 16-node quadratic interface elements (INTER 204). These CZM elements are used to simulate material's resistance to delamination. Additionally, contact model has been introduced at the interface to simulate contact and sliding after completion of delamination. A contact pair has been defined that contact surfaces are the inner surface of the ionomer while the target surfaces are the outer surface of the Pt/C agglomerate, as

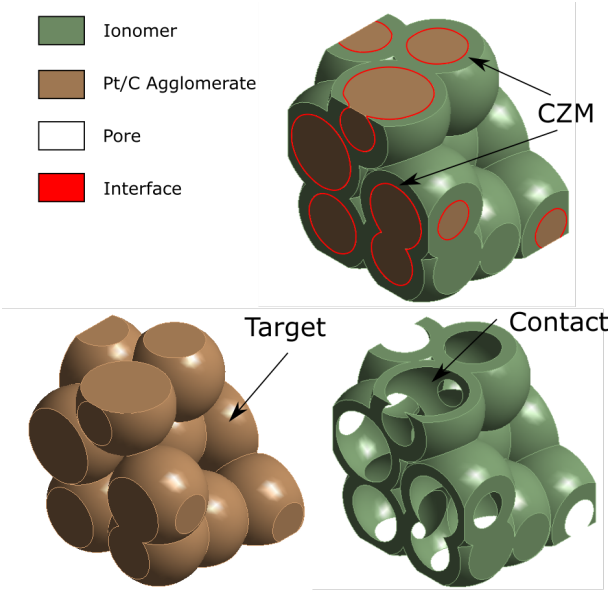

Fig. 4.8: A schematic showing the microstructure of the catalyst layer.

illustrated in **Fig. 4.8**. The contact surfaces are discretized with 8-Node surface-to-surface contact elements (CONTA 174) and the target surfaces are discretized with pairing target elements (TARGE 170). Therefore, the computational domain of this thesis research has been divided into a series of grids to simulate deformation and delamination in the CL microstructure.

The solid (SOLID 187), CZM (INTER 204) and contact (CONTA 174, TARGE 170) elements are selected in a way that all elements are compatible to each other [121].

4.6.3 Grid Independency

Mesh independence study has been conducted to ensure the solution is independent of mesh. An uniform mesh scheme has been applied to the interface between the ionomer

and the Pt/C agglomerate. Since the focus of the study is the interface delamination, the interface has been refined from 17853 CZM elements to 106589 CZM elements. The area of delaminated surface after one hygrothermal cycle obtained by 106589 CZM elements has been selected as the "exact solution", and the relative errors, Err is defined as

$$Err = \left| \frac{\Theta_{\text{ref}} - \Theta_N}{\Theta_{\text{ref}}} \right| \times 100\% \tag{4.36}$$

where θ represents the variables to be compared (i.e., the delaminated surface area).

As shown in **Fig. 4.9**, the error term drops quickly from nearly 10% as the number of CZM elements is increased. By considering the trade-off between the accuracy and computational time, a mesh with 54651 CZM elements and 72762 solid elements has been selected for the current study with an relative error of 2.68%, which is quite reasonable.

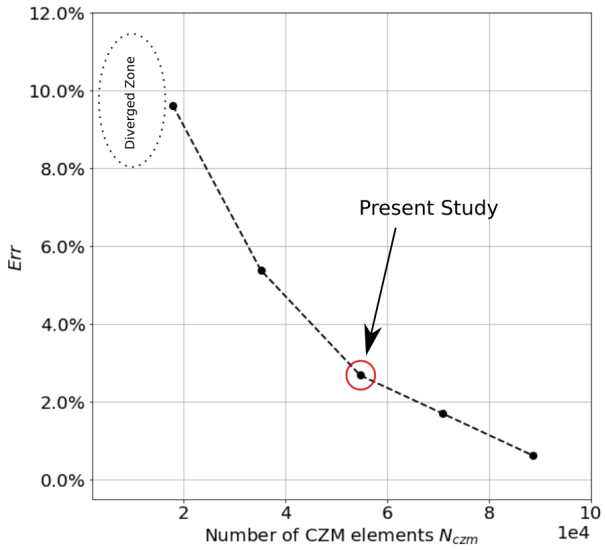

Fig. 4.9: Effect of number of CZM elements at the interface.

4.7 Comparison with Experimental Data

This section is focused on two parts: (i) The elasto-viscoplastic material model under different humidity and temperature conditions; (ii) the CZM interface model to capture the delamination onset and propagation. The viscoplasticity model is validated from the experimental work by Lu et al. [116] and its companion numerical study by Khattra et al. [115] while the CZM damage model is validated against the experimental data by Jia et al. [79].

4.7.1 Validation of Elasto-viscoplasticity Model

In the experimental work by Lu et al. [116], tensile tests were conducted on Nafion 211 to investigate the variations in Young's modulus and proportionality constant under a range of humidity, temperature and strain rate. The mechanical response of Nafion 211 was studied under three strain rates (5 min^{-1}, 0.2 min^{-1}, and quasi-static) for different temperatures (25 $^{\circ}C$, 45 $^{\circ}C$, 65 $^{\circ}C$ and 80 $^{\circ}C$) and relative humidities (30 %, 50 %, 70 % and 90 %). It might be pointed out that the strain rate in their study is the engineering strain rate applied by a tensile machine.

As shown in **Fig. 4.10**, the present model prediction agrees well with the experimental data [116]. It should be pointed out that the elasto-viscoplastic model is unable to capture the time-dependence of the Young's modulus E, which is responsible for the slight deviation from the experimental data at the higher strain rate shown in **Fig. 4.10b**. However, the ionomer's temperature and humidity dependence dominate its dependence on strain rates [116, 134]. Therefore, it is reasonable to assume the time independence of Young's

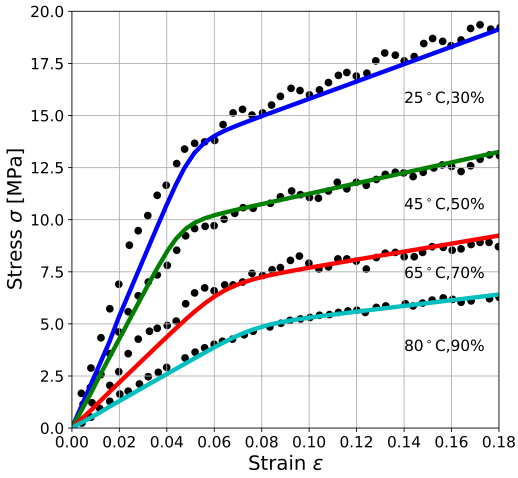

(a) Strain rate of 0.2 min^{-1}

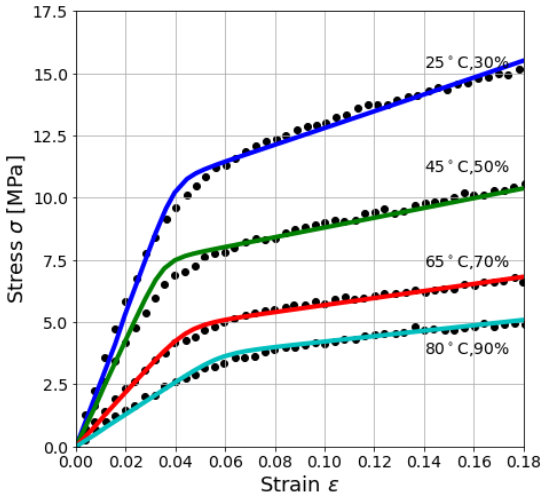

(b) Strain rate of 5 min^{-1}

Fig. 4.10: The stress-strain relation for Nafion 211 at different temperature and humidity values [116] in comparison with the present constitutive model for strain rates (a) at 0.2 min^{-1}, and (b) at 5 min^{-1}. • symbols are the experimental data [116], the solid lines are the model prediction from the present study.

modulus for the ionomer.

4.7.2 Validation of Damage Model

A double cantilever beam (DCB) experiment conducted by Jia et al. [79] investigates the mode I fracture toughness G_I of the catalyst coated membrane (CCM) at the ambient condition of 20 $°C$ and 30% RH. According to the procedure described in the ASTM D5528-94a standard [135], the loading is applied via two load cells at the tip of the double cantilever beam. An initial crack length a_0 is cut into the CCM sample and the load displacement data is recorded experimentally and the critical mode I fracture toughness G_I is interpolated via data reduction methods [136].

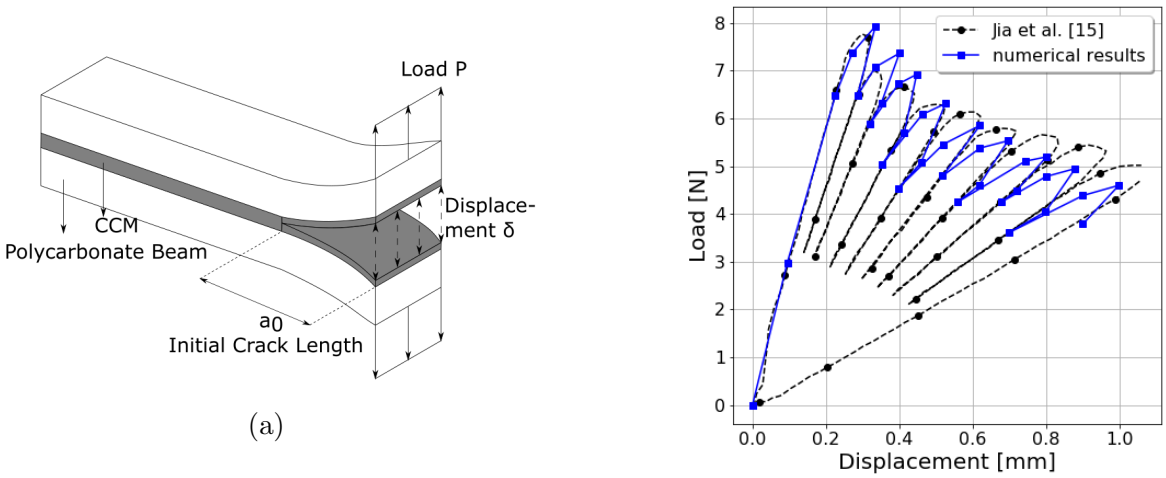

(a)

(b)

Fig. 4.11: (a) Schematic of the double cantilever beam experiment; (b) Comparison between the present model prediction and the experimental results [79].

Under the loading condition specified in ASTM D5528-94a [135], the capability of the current fracture model has been tested against experimental results [79]. As illustrated in Fig. 8, the model prediction agrees fairly well with the experimental results. The model captures the peak load well with only 2.15% percentage difference where the onset of delamination occurs, but underestimates the load as delamination propagation continues where the largest peak load percentage difference is 8.14%. The estimation of the fracture toughness for the mode I fracture G_{Ic} is calculated empirically by [79, 136]

$$G_{Ic} = \frac{12P_C^2a^2}{B^2h^3E'}(1 + 0.64\frac{h}{a})^2 \tag{4.37}$$

where G_I is a function of the cantilever beam geometry, Young's modulus and peak load P_C where deviation from the linearity occurs in the load-displacement curve. Therefore,

since the simulated peak force matches well with the experiment peak force, it implies a good match for the fracture toughness G_I, which validates the damage model.

Chapter 5

Results and Discussion

The purpose of this chapter is to present and analyze the morphological variations during hygrothermal cycles including: (i) the delamination between the ionomer and Pt/C agglomerate, (ii) the ionomer thickening effect due to the plastic strain accumulation in the ionomer.

5.1 Overview

In order to quantify the performance of the CL, the technique for estimating the electrochemical surface area (ECSA) by Cyclic Voltammetry (CV) has been used for decades. The ECSA (current/nominal area) of the CL is a measure of quality of the three phase interface where reactants, ionic-conductive and eletron-conductive material and active catalyst sites are in close contact. During fuel cell operation, the dynamic driving conditions leads to interface delamination between the ionomer and the catalyst/carbon agglomerate.

The delamination causes detachment of the ionomer from the catalyst surface hindering the close contact of the three phases and leading to performance degradation. The delamination process between the ionomer and Pt/C agglomerate in the current study is characterized with the degree of delamination Ψ and ionomer coverage loss A_{loss}. The degree of delamination Ψ is an elemental value at the interface in the discretized model. It is defined as

- $\Psi = 0$ means the ionomer thin layer is still bonding with the catalyst agglomerate, ensuring intimate contact between the ionomer and the catalyst agglomerate for electrochemical reaction to occur.
- $\Psi \in (0\,,\,1)$ stands that the delamination is in progress. As the Ψ increases, the ionomer thin layer is peeled and moving away from the catalyst agglomerate indicating a gradual loss of performance.
- $\Psi = 1$ stands for complete interface delamination and the ionomer is completely detached from the catalyst agglomerate.

For simplicity, the failure criterion for unsuccessful electrochemical reaction is the degree of delamination equal to one ($\Psi = 1$) without considering the gradual degradation when $\Psi \in (0\,,\,1)$. Correspondingly, the ionomer coverage loss A_{loss} is defined as

$$A_{\text{loss}} = \frac{N_{\Psi=1}}{N_{\text{total}}} \tag{5.1}$$

where N_{total} is the total number of CZM elements at the interface between the agglomerate and the ionomer thin film and $N_{\Psi=1}$ the number of CZM elements with the degree of

delamination of unity ($\Psi = 1$).

A_{loss} equal to unity stands for the entire ionomer thin film that is delaminated away from the catalyst/carbon agglomerate, while A_{loss} equal to zero means the entire thin film is attaching with the agglomerate. In this analysis, the degree of delamination Ψ and ionomer coverage loss A_{loss} during any hygrothermal cycles refers to the value occurs at fuel cell operating condition (85 $^{\circ}C$ and 90 %), unless otherwise specified.

Due to the viscoplasticity of the ionomer, the ionomer network in CL after duty cycles experiences irreversible deformation and plastic strain accumulation. The accumulation of plastic strain in return increases the total volume of the ionomer thin layer binding the catalyst agglomerate. The residual volume after cyclic hygrothermal loading thickens the ionomer thin film and increases the oxygen mass transport resistance in the ionomer component of the CL. In order to capture the ionomer layer thickening phenomena due to accumulated plastic damage, the variation in ionomer thin film thickness $\Delta t_{\text{ionomer}}$ is estimated from the relative variation in volume. It is defined as

$$\Delta t_{\text{ionomer}} = \frac{t^{i}_{\text{ionomer}} - t^{\text{fresh}}_{\text{ionomer}}}{t^{\text{fresh}}_{\text{ionomer}}} \tag{5.2}$$

$$t^{\text{fresh}}_{\text{ionomer}} = \frac{V^{\text{fresh}}}{SA^{\text{fresh}}}, t^{i}_{\text{ionomer}} = \frac{V^{i}}{SA^{i}} \tag{5.3}$$

where $\Delta t^{\text{local}}_{\text{ionomer}}$ is the average ionomer thickness variation, $t^{\text{fresh}}_{\text{ionomer}}$ the initial ionomer thickness before loading, $V^{\text{fresh}}_{\text{ionomer}}$ the initial volume of the ionomer before loading, SA^{fresh} the initial ionomer surface area before loading and t^{i}_{ionomer}, V^{i}_{ionomer} and SA^{i} are the ionomer thickness, ionomer volume and ionomer surface area after i cyclic hygrothermal loading, respectively.

However, the ionomer thickening across the interface is not uniform and the direct comparison between the undeformed and deformed geometry is difficult because the shape information at elemental level is not accessible. Therefore, the variation in ionomer thin film thickness is averaged across the interface and it is estimated by the volume variation only in this thesis research. By substituting **Equ. 5.3** into **Equ. 5.2**, it yields

$$\Delta t_{\text{ionomer}} \approx \frac{V^{i}_{\text{ionomer}} - V^{\text{fresh}}_{\text{ionomer}}}{V^{\text{fresh}}_{\text{ionomer}}} \tag{5.4}$$

The degree of delamination Ψ is useful for visualizing and inspecting the gradual failure of the ionomer peeling at specific locations. The parameters $\Delta t_{\text{ionomer}}$ and A_{loss} have been used to describe the failure mechanisms for the entire structure. The above defined physical quantities Ψ, $\Delta t_{\text{ionomer}}$ and A_{loss} has been extensively studied parametrically in this study under different driving profiles. The driving profiles are studied in the order schematically shown in **Fig. 5.1**. From **Section. 5.2** to **Section. 5.4**, the effect of peak-to-peak amplitude of the relative humidity cycles, start-up and shutdown frequency of PEM fuel cells will be investigated, and different driving and parking duration will be investigated.

5.2 Effect of Peak-to-peak Amplitude

The effect of hygrothermal cycle Peak-to-peak (P-p) amplitude for relative humidity ΔRH and for temperature ΔT are analyzed for a constant clamping stress of 1 MPa. As illustrated in **Fig. 5.2**, the cases investigated are $\Delta RH = 20$ % and $\Delta T = 20$ $^{\circ}C$, $\Delta RH =$

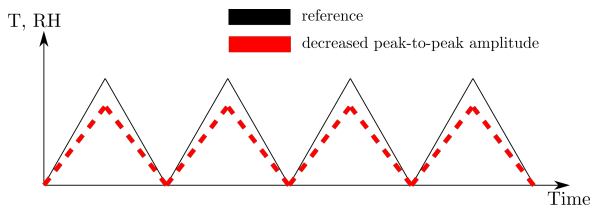

(a) Effect of peak-to-peak amplitude.

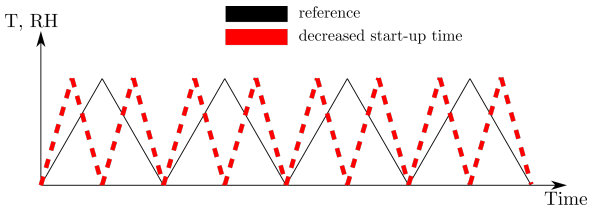

(b) Effect of start-up/shutdown frequency.

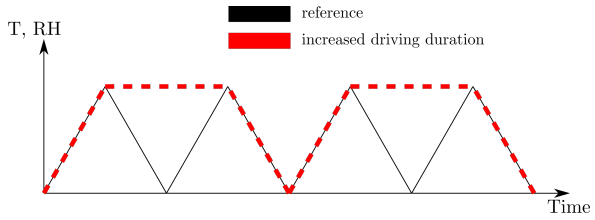

(c) Effect of driving duration.

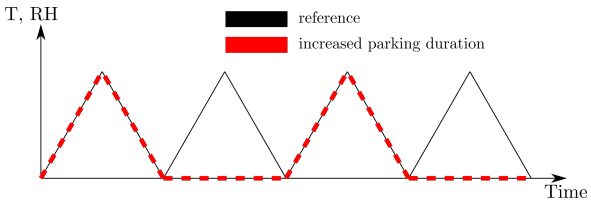

(d) Effect of parking duration.

Fig. 5.1: Schematic showing different driving profile investigating the effect of hygrothermal peak-to-peak amplitude, the driving duration, the parking duration and the start-up/shutdown frequency.

40 % and $\Delta T = 40\ ^{\circ}C$ and $\Delta RH = 60$ % and $\Delta T = 60\ ^{\circ}C$ for one and multiple driving cycles, respectively. Since the ionomer strain due to change in relative humidity is much larger than the strain due to the temperature change as given by **Equ. 4.5** and **Equ. 4.6**, relative change in relative humidity ΔRH is mainly referred hereafter as the condition.

One Driving Cycle $\Delta RH = 60\,\%$

The ionomer morphology during one driving cycle ($\Delta RH = 60\,\%$) has been investigated. During one driving cycle, the CL temperature and relative humidity are increased from 25 $^{\circ}C$ to 85 $^{\circ}C$ and 30 % to 90 % under the course of 200 sec. The interface delamination is visualized during the peak hygrothermal loading from different viewing angles as schematically shown in **Fig. 5.3**. It is observed that 31.94 % of the ionomer thin film is

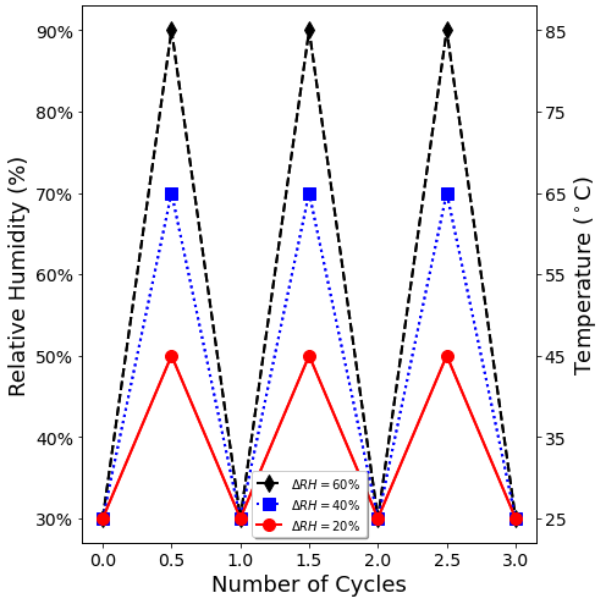

Fig. 5.2: Applied hygrothermal cycles with varying peak to peak amplitude ΔRH = 20 %, 40 % and 60 % with a simultaneous change in temperature from 25 $°C$ to 45 $°C$, 65 $°C$ and 85 $°C$, respectively.

completely delaminated from the Pt/C agglomerate after one driving cycle. Additionally, as schematically shown in **Fig. 5.3b**, the delaminated interface concentrates on the outer regions of the agglomerate structure adjacent to pore. One of the possible explanation is that the ionomer at outer region is not mechanically supported by other agglomerate and hence is allowed to expand freely under hygrothermal stress. The free expansion causes the ionomer thin film being separated and detached from the Pt/C agglomerate indicating loss of protonic pathway to the reaction sites, and hence performance loss. Moreover, the surface dip is more resilient to delamination as shown in **Fig. 5.3d**. The interface between the ionomer and the Pt/C agglomerate at the concavity of the surface dip is still intact. It is because the ionomer thin film around the surface dip being pushed back by neighbouring hydrated ionomer during the expansion making the surface dip more resilient to the

delamination.

The observation in **Fig. 5.3b** and **Fig. 5.3d** implies that the interface delamination is not uniform across the interface and is dependent on the surface morphology. Less-supported outer region of the agglomerate is more prone to delamination, while surface dip is more resilient to delamination. It implies that the surface morphology of agglomerate is an important design parameter for the durability of the catalyst layer and it is crucial to control the agglomerate structure in a manner to minimize the less-supported outer region prone to be damaged.

One Driving Cycle $\Delta RH = 20\,\%$ and $60\,\%$

The ionomer coverage morphology during one driving cycle at different P-p amplitude $\Delta RH = 20\,\%$ and $60\,\%$ is studied. As illustrated in **Fig. 5.4**, the degree of delamination is proportional to the magnitude of hygrothermal P-p amplitude. At the maximum hygrothermal loading during the first driving cycle, the ionomer coverage loss A_{loss} with $\Delta RH = 20$ % and $\Delta RH = 60\,\%$ is 26.64 % and 31.94 %, respectively. It implies that the amplitude of P-p hygrothermal cycle is a main contributor to the interface delamination.

At high P-p amplitude $\Delta RH = 60$ % case, the interface is more intact at the location where multiple agglomerate surfaces intersect together. It is most likely because there is more swelling in the ionomer network for the high $\Delta RH = 60$ % case. The ionomer thin layer expands out after absorbing water molecule until it touches on other ionomer thin layers covering other Pt/C agglomerate. The surface intersection causes the ionomer layer to "merge" together. This unique structure resists the ionomer thin layer to freely expand and the reaction force pushed swelling ionomer tightly against the Pt/C agglomerate

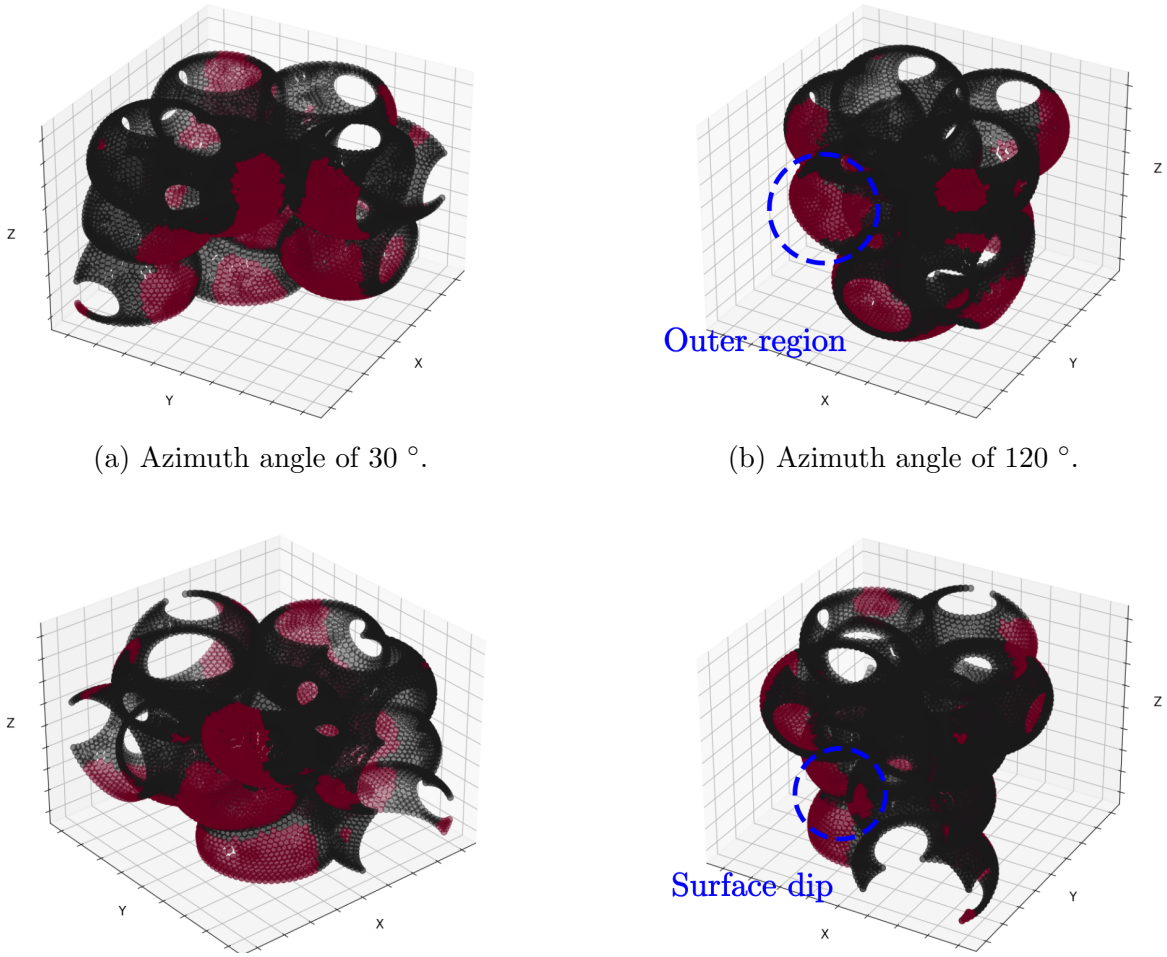

(a) Azimuth angle of 30 °.

(b) Azimuth angle of 120 °.

(c) Azimuth angle of 230 °.

(d) Azimuth angle of 300 °.

Fig. 5.3: The visualization of the ionomer delamination from the Pt/C agglomerate at the peak loading of one driving cycle $\Delta RH = 60\,\%$. The complete delaminated interface $\Psi = 1$ is shown in red while the intact interface and interface not completely delaminated $\Psi \in [0, 1)$ is shown in black. The ionomer delamination is visualized at elevation viewing angle of 30 °, and azimuth angle of (a) 30 °; (b) 120 °; (c) 230 °; (d) 300 °.

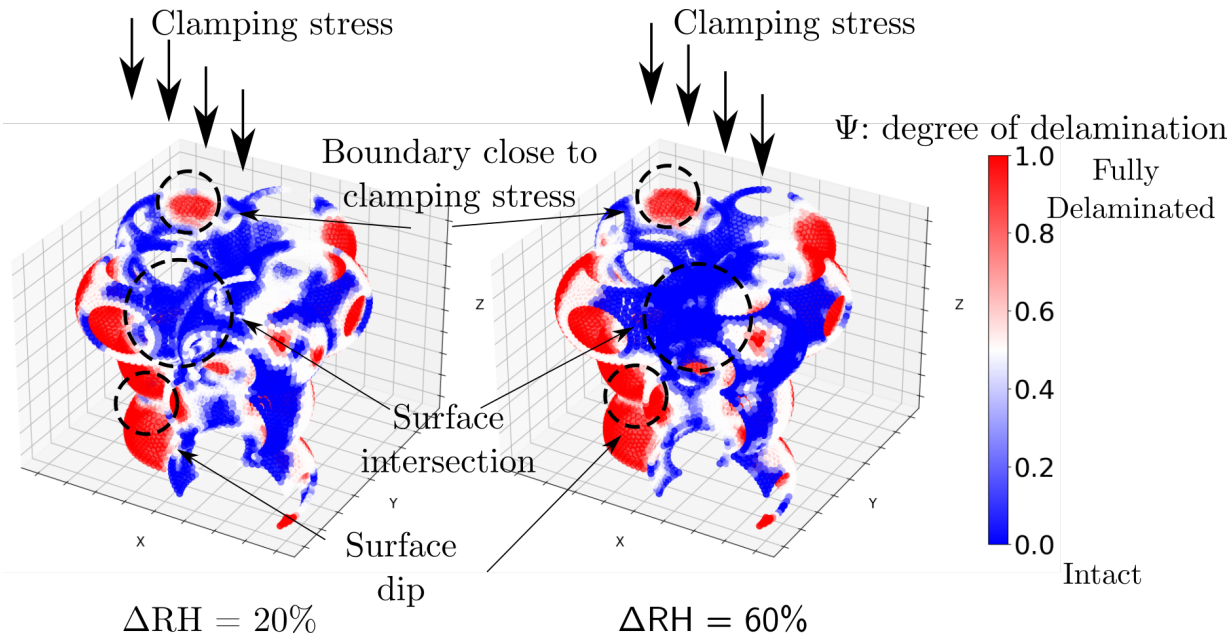

Fig. 5.4: The ionomer coverage characterized by the degree of delamination Ψ at maximum hygrothermal loading during 1st driving cycle at $\Delta RH = 20$ % and 60 %.

resulting in more intact interface at high $\Delta RH = 60$ % case.

Multiple Driving Cycles

Pei *et al.* studied the driving conditions of one of their demonstrating fuel cell buses running fixed route for over 43,000 km [137]. In their study, the measured average start-stop cycles for the fuel cell buses is 0.99 cycles/h. Due to the limitation in computational resources, 25 start-stop cycles are investigated in this thesis research which is approximately equal to the number of start-stop cycles in 25 hours of operation of fuel cell buses running on fixed route.

The ionomer coverage evolution for 25 driving cycles at P-p amplitude $\Delta RH = 60$ % is

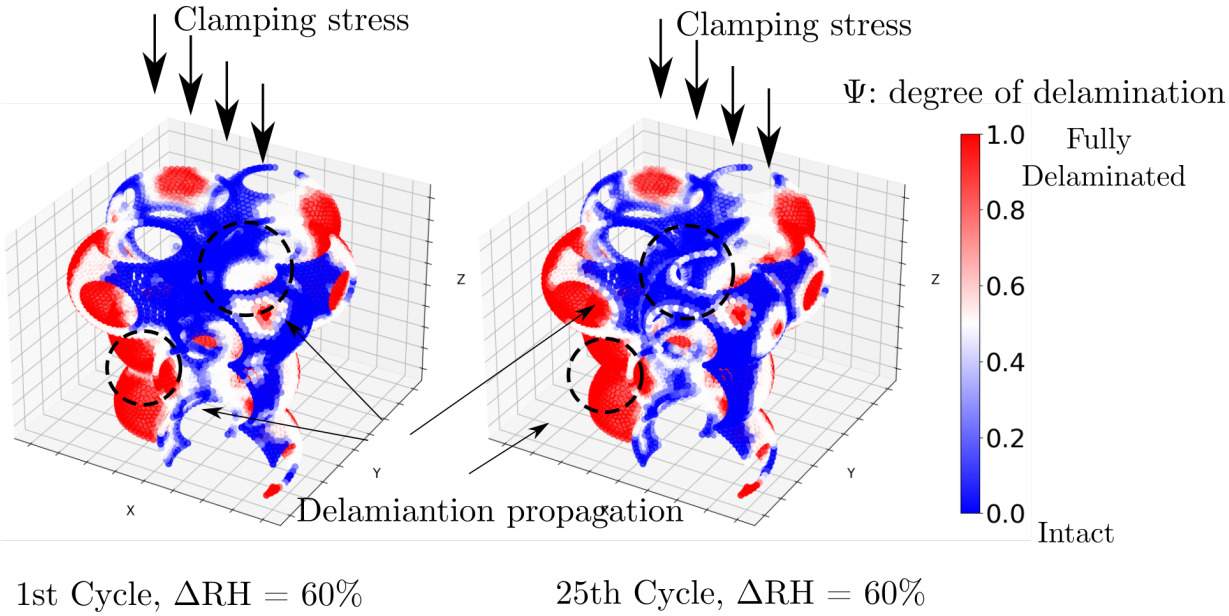

Fig. 5.5: The ionomer coverage characterized by the degree of delamination Ψ at maximum hygrothermal loading after the 1st and 25th driving cycle at $\Delta RH = 60$ %.

investigated. The ionomer coverage characterized by ψ at the peak hygrothermal loading after the 1st and 25th cycles is shown in **Fig. 5.5**. The ionomer coverage loss A_{loss} at the peak loading in the 1st driving cycle is 31.94 %. After 25 start-stop cycles, the ionomer coverage loss A_{loss} increases to 35.29 %. The delamination propagates and approximately 4 % more interface is completely delaminated after the 25th driving cycles. It is observed that the delamination-resilient surface dip has been delaminated after the 25 driving cycles.

As shown in **Fig. 5.6**, the thickness increase of the ionomer layer $\Delta t_{\text{ionomer}}$ and the ionomer coverage loss A_{loss} for 25 hygrothermal cycles at various hygrothermal P-p amplitude ($\Delta RH = 20$ %, 40 % and 60 %) is investigated. In **Fig. 5.6a**, the ionomer thickening induced by plastic deformation is proportional to the hygrothermal P-p amplitude. At the highest $\Delta RH = 60\%$ loading, the ionomer thickness increases 1.71 % and 2.02 % after 1

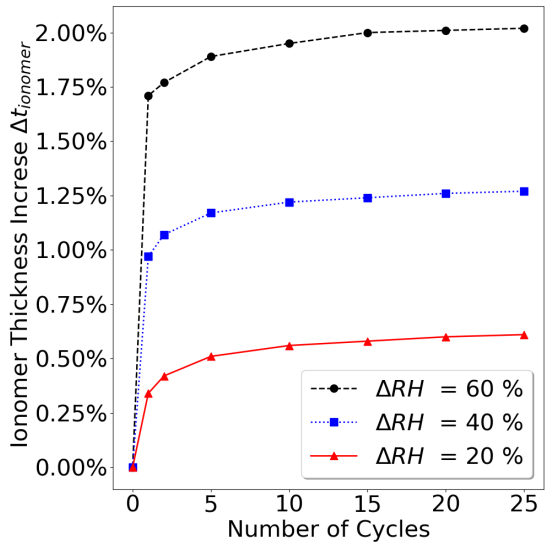

(a) Ionomer thickening $\Delta t_{ionomer}$

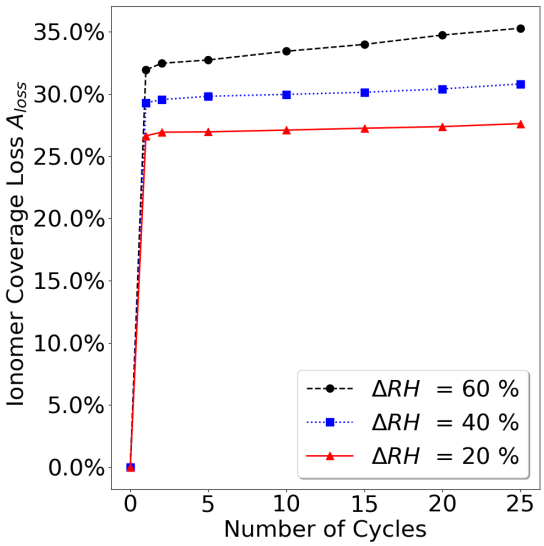

(b) Ionomer coverage loss A_{loss}.

Fig. 5.6: The effect of varying peak-to-peak amplitude ΔRH (20 %, 40 % and 60 %) for 25 driving cycles on (a) Ionomer thickening $\Delta t_{\text{ionomer}}$; (b) the ionomer coverage loss A_{loss}.

and 25 cycles, respectively. By comparison with $\Delta RH = 20\%$, the ionomer thin film only increases 0.34 % and 0.61 % after 1 and 25 cycles, respectively. The ionomer thickness is caused by the residual strain after hygrothermal loading applied. The reduced hygrothermal cycle P-p amplitude greatly reduces the amount of residual strain of the ionomer resulting in decreased ionomer thickening. Additionally, the ionomer material property is dependent on temperature and relative humidity. The yield strength σ_y decreases as the temperature and relative humidity increases as shown in **Fig. 4.10**. At low temperature and humidity value ($\Delta RH = 20\,\%$), the ionomer exhibits high yield strength. Hence, the residual strain is much lower in the case of $\Delta RH = 20\,\%$ compared with the case of $\Delta RH = 60\,\%$.

In **Fig. 5.6b**, the ionomer coverage loss A_{loss} is also proportional to the P-p hygrother-

mal amplitude. The delamination propagates in a bilinear manner. At the peak loading in first hygrothermal cycle, the ionomer coverage loss A_{loss} at $\Delta RH = 20$ %, 40 % and 60 % is 26.64 %, 29.28 % and 31.94 %, respectively. After the first driving cycle, the delamination propagates linearly to 27.62 %, 30.81 % and 35.29 % during 25th driving cycles for ΔRH = 20 %, 40 % and 60 %, respectively.

5.3 Effect of Start-up/Shutdown Time

As the ionomer exhibits elasto-viscoplasticity, the deformation of the ionomer is time-dependent and sensitive to the applied loading rate. Hence, it is crucial to examine how the ionomer mythologies varies responding to different hygrothermal loading rates. As schematically shown in **Fig. 5.7a**, the start-up duration of $\Delta t_{start-up}$ = 200 sec, 100 sec and 50 sec are studied for cyclic loading conditions.

In **Fig. 5.7a** and **Fig. 5.7b**, the ionomer thickness percentage increase $\Delta t_{\text{ionomer}}$ and the ionomer coverage loss A_{loss} for 25 hygrothermal cycles are investigated for start-up time $\Delta t_{start-up}$ of 200 sec, 100 sec and 50 sec at $\Delta RH = 60$ %. As presented in **Fig. 5.7a**, the ionomer thickening due to plastic strain is proportional to the start-up time. After the 1st hygrothermal cycle, the ionomer thickness increase $\Delta t_{\text{ionomer}}$ for $\Delta t_{\text{start-up}}$ = 200 sec, 100 sec and 50 sec is 1.71 %, 1.75 % and 1.71 %, respectively. This non-linear pattern is caused by time-dependency of the ionomer. The plastic deformation of the ionomer is irreversible and it consists of time-dependent and time-independent component. As the start-up time increases (lower loading rate), both the time under hygrothermal stress and the ionomer yield strength σ_y increase according to the ionomer stress-strain relationship shown in

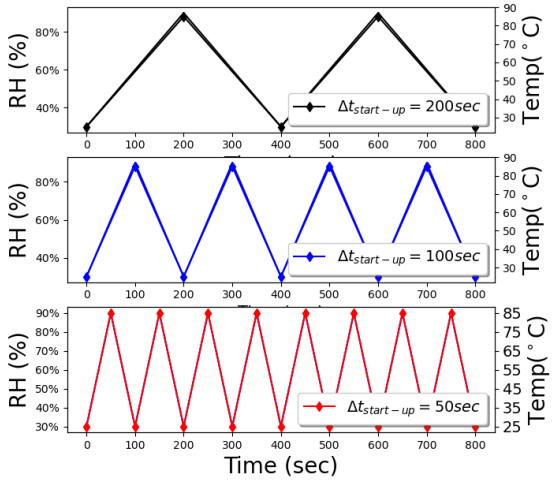

(a) Applied hygrothermal cycles with different start-up time.

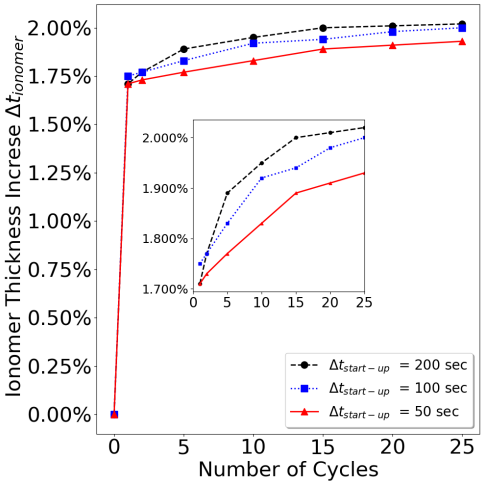

(b) Ionomer thickening $\Delta t_{ionomer}$.

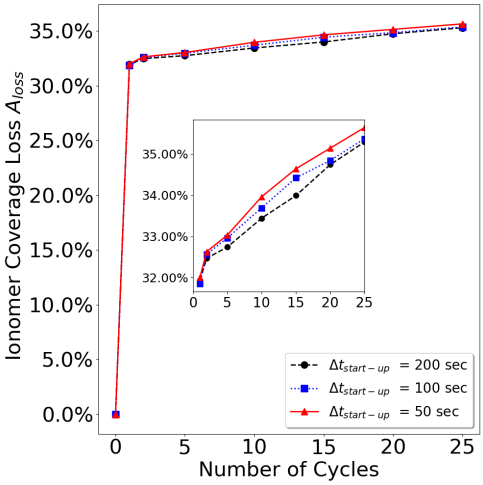

(c) the ionomer coverage loss A_{loss}.

Fig. 5.7: (a) Applied hygrothermal cycles with varying start-up time $\Delta T_{\text{start-up}} = 200$ sec, 100 sec and 50 sec. The effect of varying start-up time $\Delta t_{\text{start-up}}$ (200 sec, 100 sec and 50 sec) for 25 driving cycles on (b) ionomer thickness percentage increase; (c) the ionomer coverage loss A_{loss}.

Fig. 4.10. The case with $\Delta t_{\text{start-up}} = 200$ sec has the longest time under hygrothermal stress after the 1st cycle. The time-dependent plastic deformation is the highest among all three cases investigated. However, as the rise of yield strength at slower loading rate, the time-independent plastic deformation decreases. As the start-up time continues to decrease (increasing hygrothermal loading rate), the time-dependent plastic deformation decreases as the time-independent plastic deformation increases. At the case of $\Delta t_{\text{start-up}} = 100$ sec, the total plastic deformation peaks. Correspondingly, the ionomer thickness also peaks after 1 driving cycle with a percentage increase of $\Delta t_{\text{ionomer}}$ of 1.75 % After the 1st cycle, the ionomer residual volume is proportional to the $\Delta t_{\text{start-up}}$. The $\Delta t_{\text{ionomer}}$ for start-up time of 200 sec, 100sec and 50 sec is 2.02 %, 2 % and 1.93 % after 25 driving cycles, respectively.

An opposite pattern has been observed in the ionomer coverage loss A_{loss} as schematically shown in **Fig. 5.7c**. the ionomer coverage loss A_{loss}, unlike ionomer thickness $\Delta t_{\text{ionomer}}$, is inversely proportional to the start-up time $\Delta t_{\text{start-up}}$. It means that the quicker start-up leads to more interface delamination but less ionomer thickening. Therefore, there is competition between the ionomer yield failure and the interface fracture failure. The main contributor for this competition is the viscoplasticity of the ionomer. This finding in the current 3D model echoes with the finding observed by Rong et al. [13, 14] in their 2D representative CL microstructure study.

5.4 Effect of Driving and Parking

One Driving Cycle

The ionomer morphology is studied during one driving cycle ramping up from ambient condition (25 $^{\circ}C$ and 30 %) to operating condition (85 $^{\circ}C$ and 90 %) in 200 sec, holding for 400 sec and shutting down to ambient condition in 200 sec shown in **Fig. 5.8a**.

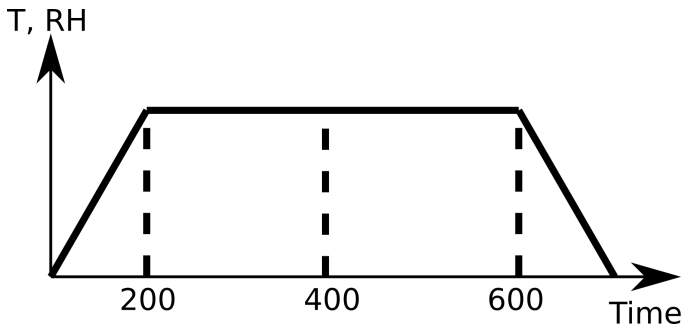

(a)

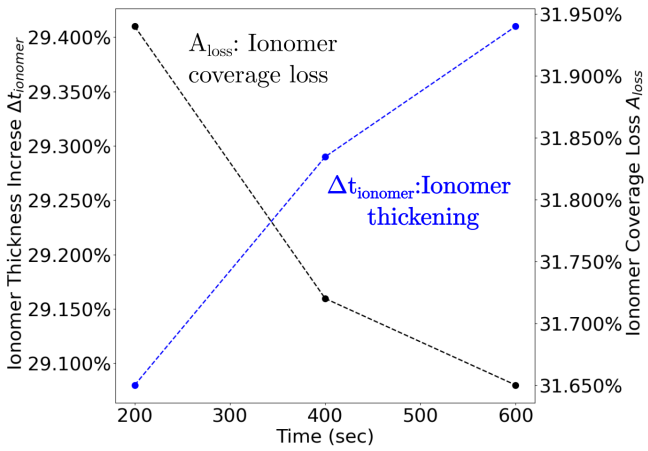

(b)

Fig. 5.8: (a) Applied hygrothermal cycle with start-up/shutdown time of 200 sec and driving duration of 400 sec; (b) the ionomer coverage loss A_{loss} and ionomer thickness increase $\Delta t_{ionomer}$ during the 1st driving cycle evaluated at 200 sec, 400 sec and 600 sec.

As shown in **Fig. 5.8b**, during fuel cell operating condition (85 $^{\circ}C$ and 90 %) from 200 sec to 600 sec, the ionomer thin layer continues to increase while the ionomer coverage loss A_{loss} drops down. Due to viscoplasticity of the ionomer, the plastic strain continues to accumulate under hygrothermal stress at operating condition. As ionomer film thickens, some of the delaminated ionomer thin film swells and reattaches with the catalyst agglomerate, as schematically shown in **Fig. 5.9**. The thickened nation film increases the mass transport resistance of dissolved oxygen in the ionomer film hindering the fuel cell performance. On the other hand, the reattachment of fully delaminated ionomer film to the catalyst agglomerate ensures more intimate contact at the triple phase boundaries.

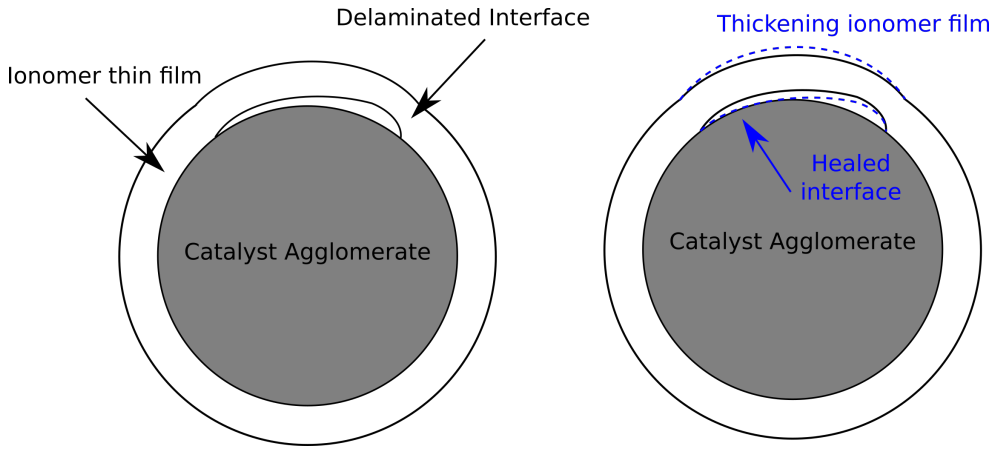

Fig. 5.9: Schematic illustrating the competing mechanism between the ionomer thickening and recovery of delaminated interface during fuel cell operating condition.

Multiple Driving Cycles

In this section, the degrading influences of the driving duration and parking duration under specified driving profiles are investigated. As schematically shown in **Fig. 5.10a**, the P-p hygrothermal amplitude of $\Delta RH = 60$ % is applied with a driving and parking duration

of 0 sec and 0 sec, 400 sec and 0 sec and 400 sec and 400 sec, respectively, for the three cases investigated. **Fig. 5.10b** presents the influences of driving and parking duration on the ionomer thickening due to plastic degradation in the ionomer. It is found out that increased driving duration leads to increased ionomer thickness after hygrothermal loading. After 15 driving cycles, the percentage increases of ionomer thickness $\Delta t_{\text{ionomer}}$ is 2 % and 2.19 % for 0 sec and 400 sec driving duration, respectively. It indicates the increasing time under operating condition will lead to more plastic strain accumulation in the ionomer, resulting in increased mass transport resistance for the dissolved oxygen to reach reaction sites. Additionally, after applying a 400 sec parking duration to allow the ionomer to be relaxed, there is a significant decrease in the ionomer thickening effect.

With the addition of 400 sec parking duration immediately after shutdown, the percentage of ionomer thickening $\Delta t_{\text{ionomer}}$ reduces from 2.19 % to 1.89 % at the end of 15th hygrothermal cycles. During fuel cell operating condition (85 $^{\circ}C$ and 90 %), the ionomer is subjected to a constant hygrothermal stress. The ionomer thin film in CL experiences a time-dependent increase in strain due to the ionomer' viscoplastic characteristics. During PEM fuel cell vehicle parking (25 $^{\circ}C$ and 30 %), the constant hygrothermal stress is removed. The ionomer strain immediately decreases (elastic characteristics) then gradually decreases (viscoplastic characteristics) to a residual strain over a period of time. In indicates that there is a necessity for designing a relaxation schedule for PEM fuel cell vehicle to reduce the hygrothermal degradation in CL. In **Fig. 5.10c**, the effect of driving and parking duration have a complex impact on the ionomer coverage loss A_{loss}. The ionomer coverage loss A_{loss} is, unlike ionomer thickening $\Delta t_{\text{ionomer}}$, inversely proportional to the increasing driving duration. It reconfirms with the mechanism illustrated in **Fig. 5.9**

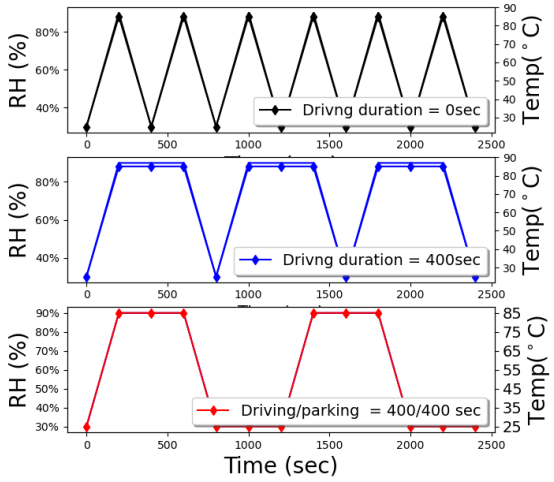

(a) Applied hygrothermal cycles with various driving/parking.

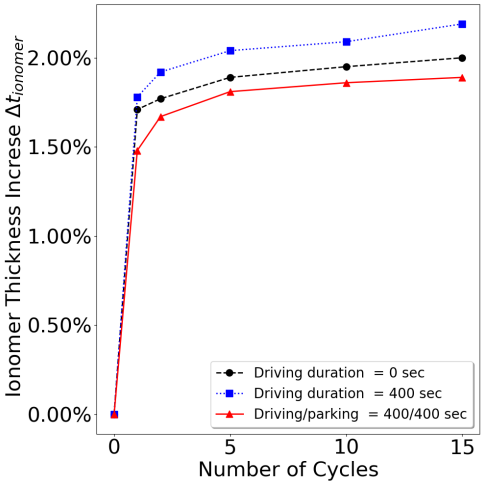

(b) Ionomer thickening $\Delta t_{\text{ionomer}}$.

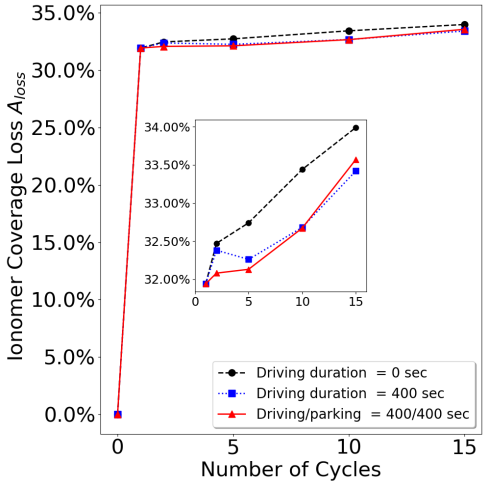

(c) Ionomer coverage loss A_{loss}.

Fig. 5.10: (a) Applied hygrothermal cycles with 0 driving duration, 400 sec driving duration and 400 sec driving with 400 sec parking. The effect of driving and parking on (b) ionomer thickness percentage increase; (c) Ionomer coverage loss A_{loss}.

where the delaminated ionomer thin layer reattaches with the catalyst agglomerate after the ionomer plastic strain accumulates. As for the effect of parking duration, it can be

observed that during the first 10 cycles the 400 sec rest after 400 sec operation shows slower hygrothermal degradation. After 10th cycle, the effect of parking duration is no longer showing better resistance to ionomer coverage degradation. It is mainly due to the reduced residual strain in the ionomer thin film. The reduced ionomer residual volume causes less healing of delaminated interface.

5.5 Summary

In this chapter, a three-dimensional numerical model for the catalyst layer (CL) of the PEM fuel cells has been developed to study the morphological variations and hygrothermal degradation mechanism in CL under different profiles of cyclic loading conditions. The effect of (1) peak-to-peak hygrothermal amplitude, (2) fuel cell stack start-up/shutdown time, and (3) duration of driving and parking are investigated.

A visualization method has been employed to study how ionomer is gradually peeled and delaminated away from the catalyst/carbon agglomerate. It is found that the hygrothermal failure is greatly dependent on the structure and distribution of the agglomerate. It is summarized that (1) the outer region of the agglomerate where not mechanically supported by other agglomerates are more susceptible to delamination; (2) the agglomerate surface dip where the surface concaves in is more resistant to being damaged; (3) the region where multiple agglomerate surfaces intersect shows better resistance to delamination.

In the numerical model, the two performance loss indicator A_{loss} and $\Delta t_{\text{ionomer}}$ have been used to analyze the structural degradation and the following observation have been made: (1) the hygrothermal amplitude is the major contributor to the mechanical degradation of

the catalyst layer; (2) Increasing the start-up frequencies alleviate the problem of ionomer plastic damage at the expense of aggravating the loss of ionomer coverage; (3) a competition between the ionomer thickening and the ionomer coverage has been found; (4) resting fuel cell stack at ambient condition immediately after the long-term operating condition alleviates the degradation of ionomer thickening and ionomer coverage loss.

Chapter 6

Conclusions and Future Work

In this thesis work, a comprehensive understanding of the microstructure of the catalyst layer is investigated through statistical reconstruction and finite element modelling. The developed hybrid reconstruction method realistically reconstruct the catalyst layer microstructure based on statistical correlation functions extracted from experimental images. The reconstructed catalyst layer is based on spheres instead of voxels which greatly extending the practical capability of the reconstructed catalyst layer model for subsequent numerical modelling especially those requiring smoother edges. With the reconstructed catalyst layer microstructure and the validated material and fracture properties of the ionomer, a numerical model based on finite element modelling is performed to investigate the morphological variations in the microstructure under different dynamic driving cycles. The simulation work is focused on the delamination of the ionomer thin film from the catalyst agglomerate and the ionomer thickening due to residual strain in ionomer.

6.1 Conclusions of the Present Work

The key accomplishments in this thesis work are summarized as follows:

- Development of a hybrid reconstruction method and programming of the in-house codes for the reconstruction of the catalyst layer containing statistical information from experimental images. The developed hybrid reconstruction method is both practical (sphere-based) and accurate (statistical information) compared with the fabrication-based and imaged-based reconstruction in literature typically adopting pixel or voxel as unit element which causes the reconstructed geometry only applicable for numerical method like lattice Boltzmann methods but not practical for those numerical methods suffering difficulties in convergence at sharp edges or corners like FEM or FVM.

- Development of a three-dimensional FEM model for investigating and understanding the catalyst layer microstructure. A parametric study has been done on investigating different profiles of driving cycles in order to gain insights on morphological variations of microstructure.

The key contributions of the thesis work are summarized as follows

- The mechanical degradation of fuel cell is strongly dependent on the structure of the catalyst/carbon agglomerate in the catalyst layer. The delamination between the ionomer and the carbon support is not uniform across the interface. It is influenced by surface concavity and the deformed agglomerate shape. The surface concavity of deformed agglomerate all have a decisive effect on the mechanical degradation of CL.

- The ionomer thickening effect due to the accumulated plastic strain in fuel cell operation is observed in the microstructure increasing the mass transport resistance. The ionomer yield failure is proportional to the increase in hygrothermal amplitude, increasing in start-up time of fuel cell stack and increase in driving duration. Additionally, resting the fuel cell stack immediately after operation before restarting recovers some of the ionomer damage.

- The ionomer coverage loss due to delamination is proportional to the increasing hygrothermal amplitude and is inversely proportional to the fuel cell stack start-up time.

- A competition phenomenon is observed in the ionomer's plastic strain failure and the ionomer coverage loss.

6.2 Recommendations for Future Work

Further work for the reconstruction work can be summarized as follows:

- The current reconstruction work considers the two-point correlation function $S_2^{\text{solid}}(r)$ and the lineal path function $L^{\text{solid}}(r)$ for the solid phase. More statistical functions could be incorporated into the reconstruction work such as the cluster function [39] to better characterize the microstructure statistically.

- The current reconstruction work focuses on the accuracy of solid phase. It could be easily extended to focus on the pore phase accuracy by considering the two-point correlation function $S_2^{\text{pore}}(r)$ and the lineal path function $L^{\text{pore}}(r)$ for the pore phase.

- The statistical information contained in the two-point correlation function and lineal path function for a binary microstructure (solid and pore) could be used to directly compute the specific surface area and to estimate characteristics length scale. These parameters could be used to estimate a correlation function for the diffusivity and permeability and compared with experimental results. Futher, the evolution of the pore size and pore size distribution can be analyzed as well.

- The current capability of the reconstruction codes has limitations as follows:

  - The radius of the carbon spheres R_{sphere} are assumed to be uniform.
  - The ionomer thin layer is assumed to be uniformly covering the agglomerate.
  - Only the solid statistical information is considered. The statistical information of the ionomer and the carbon phase is lost after segmentation.

  It would be interesting to extend the capability of the current model by incorporating the carbon sphere distribution and the ionomer distribution obtained from experiments. Some novel methods on how to capture the statistical information for the ionomer phase and carbon phase without doing pixel swapping is highly appreciated for the subsequent numerical modelling. It is crucial for the reconstructed geometry to be applicable for numerical modelling.

- The current reconstruction part of the thesis research is written in a dynamic language Python. This language is selected because it is faster to do prototyping in the early development phase. In Python, the data types are determined at runtime, and it has a feature called the global interpreter lock, which leads to a longer reconstruction

time. It would be great to write in the static language in C or C++ for quicker reconstruction time. After it is rewritten in C++, it would be the right timing to perform more sensitivity studies on the reconstruction time.

Further work for the three-dimensional delamination work can be summarized as follows:

- The ionomer coverage loss is a good measure for performance degradation. It would be interesting to establish an empirical correlations investigating the relationship between the ionomer coverage loss with the performance loss.
- The current material properties in the model are based on experimental studies in the literature. Designing experiments to obtain the swelling expansion coefficient, stress-strain response and fracture properties at different temperatures and relative humidity values would be ideal. After these material properties are determined in-house, more confidence we will have in the accuracy of the model prediction.
- User Defined Results (UDRs) could be written in the ANSYS to interpolate more physical results of interest.
- The current computational time is not practical for more driving cycles. It would be interesting to incorporate the fatigue models such as Paris' Law to estimate for higher number of driving cycles.

References

[1] Xianguo Li. *Principles of fuel cells*. CRC Press, 2005.

[2] Kui Jiao, Jin Xuan, Qing Du, Zhiming Bao, Biao Xie, Bowen Wang, Yan Zhao, Linhao Fan, Huizhi Wang, Zhongjun Hou, et al. Designing the next generation of proton-exchange membrane fuel cells. *Nature*, 595(7867):361–369, 2021.

[3] Yun Wang, Hao Yuan, Andrew Martinez, Patrick Hong, Hui Xu, and Fred R Bockmiller. Polymer electrolyte membrane fuel cell and hydrogen station network for automobiles: Status, technology, and perspectives. *Advances in Applied Energy*, page 100011, 2021.

[4] James Kast, Ram Vijayagopal, John J Gangloff Jr, and Jason Marcinkoski. Clean commercial transportation: Medium and heavy duty fuel cell electric trucks. *International Journal of Hydrogen Energy*, 42(7):4508–4517, 2017.

[5] Rosalin Rath, Piyush Kumar, Smita Mohanty, and Sanjay Kumar Nayak. Recent advances, unsolved deficiencies, and future perspectives of hydrogen fuel cells in transportation and portable sectors. *International Journal of Energy Research*, 43(15):8931–8955, 2019.

[6] Andrew Burke and Anish Kumar Sinha. Technology, sustainability, and marketing of battery electric and hydrogen fuel cell medium-duty and heavy-duty trucks and buses in 2020-2040. 2020.

[7] Jiujun Zhang. *PEM fuel cell electrocatalysts and catalyst layers: fundamentals and applications*. Springer Science & Business Media, 2008.

[8] Roland Friedmann and Trung Van Nguyen. Optimization of the microstructure of the cathode catalyst layer of a pemfc for two-phase flow. *Journal of the Electrochemical Society*, 157(2):B260, 2009.

[9] Samaneh Shahgaldi, Adnan Ozden, Xianguo Li, and Feridun Hamdullahpur. Cathode catalyst layer design with gradients of ionomer distribution for proton exchange membrane fuel cells. *Energy conversion and management*, 171:1476–1486, 2018.

[10] Ryan O'hayre, Suk-Won Cha, Whitney Colella, and Fritz B Prinz. *Fuel cell fundamentals*. John Wiley & Sons, 2016.

[11] Shuaiba Samad, Kee Shyuan Loh, Wai Yin Wong, Tian Khoon Lee, Jaka Sunarso, Seng Tong Chong, and Wan Ramli Wan Daud. Carbon and non-carbon support materials for platinum-based catalysts in fuel cells. *international journal of hydrogen energy*, 43(16):7823–7854, 2018.

[12] S Jamai Peighambardoust, Soosan Rowshanzamir, and Mehdi Amjadi. Review of the proton exchange membranes for fuel cell applications. *International journal of hydrogen energy*, 35(17):9349–9384, 2010.

[13] Feng Rong, Cheng Huang, Zhong-Sheng Liu, Datong Song, and Qianpu Wang. Microstructure changes in the catalyst layers of pem fuel cells induced by load cycling: Part i. mechanical model. *Journal of Power Sources*, 175(2):699–711, 2008.

[14] Feng Rong, Cheng Huang, Zhong-Sheng Liu, Datong Song, and Qianpu Wang. Microstructure changes in the catalyst layers of pem fuel cells induced by load cycling: Part ii. simulation and understanding. *Journal of Power Sources*, 175(2):712–723, 2008.

[15] Yafei Chang, Jian Zhao, Samaneh Shahgaldi, Yanzhou Qin, Yan Yin, and Xianguo Li. Modelling of mechanical microstructure changes in the catalyst layer of a polymer electrolyte membrane fuel cell. *International Journal of Hydrogen Energy*, 45(54):29904–29916, 2020.

[16] Young-Chul Park, Haruki Tokiwa, Katsuyoshi Kakinuma, Masahiro Watanabe, and Makoto Uchida. Effects of carbon supports on pt distribution, ionomer coverage and cathode performance for polymer electrolyte fuel cells. *Journal of Power Sources*, 315:179–191, 2016.

[17] A Pokhrel, M El Hannach, FP Orfino, M Dutta, and E Kjeang. Failure analysis of fuel cell electrodes using three-dimensional multi-length scale x-ray computed tomography. *Journal of Power Sources*, 329:330–338, 2016.

[18] Simon Thiele, Roland Zengerle, and Christoph Ziegler. Nano-morphology of a polymer electrolyte fuel cell catalyst layer—imaging, reconstruction and analysis. *Nano Research*, 4(9):849–860, 2011.

[19] R Singh, AR Akhgar, PC Sui, KJ Lange, and N Djilali. Dual-beam fib/sem characterization, statistical reconstruction, and pore scale modeling of a pemfc catalyst layer. *Journal of The Electrochemical Society*, 161(4):F415, 2014.

[20] Nan Nan and Jingxin Wang. Fib-sem three-dimensional tomography for characterization of carbon-based materials. *Advances in Materials Science and Engineering*, 2019, 2019.

[21] Yuta Katayanagi, Takahiro Shimizu, Yoshiyuki Hashimasa, Nobuhiro Matsushita, Yohtaro Yamazaki, and Takeo Yamaguchi. Cross-sectional observation of nanostructured catalyst layer of polymer electrolyte fuel cell using fib/sem. *Journal of Power Sources*, 280:210–216, 2015.

[22] Riko Moroni and Simon Thiele. Fib/sem tomography segmentation by optical flow estimation. *Ultramicroscopy*, 219:113090, 2020.

[23] Yuan Gao. Using mrt lattice boltzmann method to simulate gas flow in simplified catalyst layer for different inlet–outlet pressure ratio. *International Journal of Heat and Mass Transfer*, 88:122–132, 2015.

[24] Gen Inoue, Kouji Yokoyama, Junpei Ooyama, Takeshi Terao, Tomomi Tokunaga, Norio Kubo, and Motoaki Kawase. Theoretical examination of effective oxygen diffusion coefficient and electrical conductivity of polymer electrolyte fuel cell porous components. *Journal of Power Sources*, 327:610–621, 2016.

[25] Navvab Khajeh-Hosseini-Dalasm, Takashi Sasabe, Takashi Tokumasu, and Ugur Pasaogullari. Effects of polytetrafluoroethylene treatment and compression on gas dif-

fusion layer microstructure using high-resolution x-ray computed tomography. *Journal of Power Sources*, 266:213–221, 2014.

[26] Robin T White, Dilip Ramani, Sebastian Eberhardt, Marina Najm, Francesco P Orfino, Monica Dutta, and Erik Kjeang. Correlative x-ray tomographic imaging of catalyst layer degradation in fuel cells. *Journal of The Electrochemical Society*, 166(13):F914, 2019.

[27] Stanley J Normile and Iryna V Zenyuk. Imaging ionomer in fuel cell catalyst layers with synchrotron nano transmission x-ray microscopy. *Solid State Ionics*, 335:38–46, 2019.

[28] Emily Leonard, Andrew D Shum, Nemanja Danilovic, Christopher Capuano, Katherine E Ayers, Lalit M Pant, Adam Z Weber, Xianghui Xiao, Dilworth Y Parkinson, and Iryna V Zenyuk. Interfacial analysis of a pem electrolyzer using x-ray computed tomography. *Sustainable Energy & Fuels*, 4(2):921–931, 2020.

[29] William K Epting, Jeff Gelb, and Shawn Litster. Resolving the three-dimensional microstructure of polymer electrolyte fuel cell electrodes using nanometer-scale x-ray computed tomography. *Advanced Functional Materials*, 22(3):555–560, 2012.

[30] Tatsuya Hattori, Ai Suzuki, Riadh Sahnoun, Michihisa Koyama, Hideyuki Tsuboi, Nozomu Hatakeyama, Akira Endou, Hiromitsu Takaba, Momoji Kubo, Carlos A Del Carpio, et al. Development of the overpotential simulator for polymer electrolyte fuel cells and application for optimization of cathode structure. *Applied surface science*, 254(23):7929–7932, 2008.

[31] Kyle J Lange, Pang-Chieh Sui, and Ned Djilali. Pore scale simulation of transport and electrochemical reactions in reconstructed pemfc catalyst layers. *Journal of The Electrochemical Society*, 157(10):B1434, 2010.

[32] NA Siddique and Fuqiang Liu. Process based reconstruction and simulation of a three-dimensional fuel cell catalyst layer. *Electrochimica Acta*, 55(19):5357–5366, 2010.

[33] Li Chen, Gang Wu, Edward F Holby, Piotr Zelenay, Wen-Quan Tao, and Qinjun Kang. Lattice boltzmann pore-scale investigation of coupled physical-electrochemical processes in c/pt and non-precious metal cathode catalyst layers in proton exchange membrane fuel cells. *Electrochimica Acta*, 158:175–186, 2015.

[34] Lei Xing, Mohamed Mamlouk, Ravi Kumar, and Keith Scott. Numerical investigation of the optimal nafion® ionomer content in cathode catalyst layer: an agglomerate two-phase flow modelling. *international journal of hydrogen energy*, 39(17):9087–9104, 2014.

[35] Yuze Hou, Hao Deng, Fengwen Pan, Wenmiao Chen, Qing Du, and Kui Jiao. Pore-scale investigation of catalyst layer ingredient and structure effect in proton exchange membrane fuel cell. *Applied Energy*, 253:113561, 2019.

[36] Yuze Hou, Sebastian Prass, Xing Li, Qing Du, Kui Jiao, and Nada Zamel. Pore-scale modeling of anode catalyst layer tolerance upon hydrogen sulfide exposure in pemfc. *Electrocatalysis*, 12(4):403–414, 2021.

[37] Jian Zhao, Adnan Ozden, Samaneh Shahgaldi, Ibrahim E Alaefour, Xianguo Li, and Feridun Hamdullahpur. Effect of pt loading and catalyst type on the pore structure of porous electrodes in polymer electrolyte membrane (pem) fuel cells. *Energy*, 150:69–76, 2018.

[38] Y Jiao, FH Stillinger, and S Torquato. Modeling heterogeneous materials via two-point correlation functions. ii. algorithmic details and applications. *Physical Review E*, 77(3):031135, 2008.

[39] Salvatore Torquato and HW Haslach Jr. Random heterogeneous materials: microstructure and macroscopic properties. *Appl. Mech. Rev.*, 55(4):B62–B63, 2002.

[40] Binglin Lu and Salvatore Torquato. Lineal-path function for random heterogeneous materials. *Physical Review A*, 45(2):922, 1992.

[41] Salvatore Torquato and B Lu. Chord-length distribution function for two-phase random media. *Physical Review E*, 47(4):2950, 1993.

[42] P Levitz. Off-lattice reconstruction of porous media: critical evaluation, geometrical confinement and molecular transport. *Advances in Colloid and Interface Science*, 76:71–106, 1998.

[43] Partha P Mukherjee and Chao-Yang Wang. Stochastic microstructure reconstruction and direct numerical simulation of the pefc catalyst layer. *Journal of the Electrochemical Society*, 153(5):A840, 2006.

[44] Lalit M Pant, Sushanta K Mitra, and Marc Secanell. Stochastic reconstruction using multiple correlation functions with different-phase-neighbor-based pixel selection. *Physical Review E*, 90(2):023306, 2014.

[45] Seung Hyun Kim and Heinz Pitsch. Reconstruction and effective transport properties of the catalyst layer in pem fuel cells. *Journal of the Electrochemical Society*, 156(6):B673, 2009.

[46] Jinfen Kang, Koji Moriyama, and Seung Hyun Kim. An extended stochastic reconstruction method for catalyst layers in proton exchange membrane fuel cells. *Journal of Power Sources*, 325:752–761, 2016.

[47] Pavel Čapek, Martin Veselỳ, Bohumil Bernauer, Petr Sysel, Vladimir Hejtmanek, Milan Kočiřík, Libor Brabec, and Olga Prokopova. Stochastic reconstruction of mixed-matrix membranes and evaluation of effective permeability. *Computational materials science*, 89:142–156, 2014.

[48] Lukas Mosser, Olivier Dubrule, and Martin J Blunt. Reconstruction of three-dimensional porous media using generative adversarial neural networks. *Physical Review E*, 96(4):043309, 2017.

[49] Reza Shams, Mohsen Masihi, Ramin Bozorgmehry Boozarjomehry, and Martin J Blunt. Coupled generative adversarial and auto-encoder neural networks to reconstruct three-dimensional multi-scale porous media. *Journal of Petroleum Science and Engineering*, 186:106794, 2020.

[50] MG Politis, ES Kikkinides, ME Kainourgiakis, and AK Stubos. A hybrid process-based and stochastic reconstruction method of porous media. *Microporous and Mesoporous Materials*, 110(1):92–99, 2008.

[51] Lalit M Pant, Sushanta K Mitra, and Marc Secanell. Multigrid hierarchical simulated annealing method for reconstructing heterogeneous media. *Physical Review E*, 92(6):063303, 2015.

[52] R Singh, PC Sui, KH Wong, E Kjeang, S Knights, and N Djilali. Modeling the effect of chemical membrane degradation on pemfc performance. *Journal of The Electrochemical Society*, 165(6):F3328, 2018.

[53] M Moein-Jahromi, MJ Kermani, and S Movahed. Degradation forecast for pemfc cathode-catalysts under cyclic loads. *Journal of Power Sources*, 359:611–625, 2017.

[54] Lida Ghassemzadeh, Klaus-Dieter Kreuer, Joachim Maier, and Klaus Muller. Chemical degradation of nafion membranes under mimic fuel cell conditions as investigated by solid-state nmr spectroscopy. *The Journal of Physical Chemistry C*, 114(34):14635–14645, 2010.

[55] Chengde Huang, Kim Seng Tan, Jianyi Lin, and Kuang Lee Tan. Xrd and xps analysis of the degradation of the polymer electrolyte in h2–o2 fuel cell. *Chemical Physics Letters*, 371(1-2):80–85, 2003.

[56] Gilles De Moor, C Bas, N Charvin, Jérôme Dillet, Gaël Maranzana, Olivier Lottin, N Caqué, E Rossinot, and L Flandin. Perfluorosulfonic acid membrane degradation

in the hydrogen inlet region: a macroscopic approach. *International Journal of Hydrogen Energy*, 41(1):483–496, 2016.

[57] A Pozio, RF Silva, M De Francesco, and L Giorgi. Nafion degradation in pefcs from end plate iron contamination. *Electrochimica acta*, 48(11):1543–1549, 2003.

[58] S Stucki, GG Scherer, S Schlagowski, and E Fischer. Pem water electrolysers: evidence for membrane failure in 100kw demonstration plants. *Journal of Applied Electrochemistry*, 28(10):1041–1049, 1998.

[59] Maurizio Pianca, Emma Barchiesi, Giuseppe Esposto, and Stefano Radice. End groups in fluoropolymers. *Journal of Fluorine Chemistry*, 95(1-2):71–84, 1999.

[60] Dennis E Curtin, Robert D Lousenberg, Timothy J Henry, Paul C Tangeman, and Monica E Tisack. Advanced materials for improved pemfc performance and life. *Journal of power Sources*, 131(1-2):41–48, 2004.

[61] Josef C Meier, Carolina Galeano, Ioannis Katsounaros, Jonathon Witte, Hans J Bongard, Angel A Topalov, Claudio Baldizzone, Stefano Mezzavilla, Ferdi Schüth, and Karl JJ Mayrhofer. Design criteria for stable pt/c fuel cell catalysts. *Beilstein journal of nanotechnology*, 5(1):44–67, 2014.

[62] PJ Ferreira, Y Shao-Horn, D Morgan, R Makharia, S Kocha, HA Gasteiger, et al. Instability of pt/ c electrocatalysts in proton exchange membrane fuel cells: a mechanistic investigation. *Journal of the Electrochemical Society*, 152(11):A2256, 2005.

[63] Katrin Schlögl, Karl JJ Mayrhofer, Marianne Hanzlik, and Matthias Arenz. Identical-location tem investigations of pt/c electrocatalyst degradation at elevated temperatures. *Journal of Electroanalytical Chemistry*, 662(2):355–360, 2011.

[64] Karl JJ Mayrhofer, Josef C Meier, Sean J Ashton, Gustav KH Wiberg, Florian Kraus, Marianne Hanzlik, and Matthias Arenz. Fuel cell catalyst degradation on the nanoscale. *Electrochemistry Communications*, 10(8):1144–1147, 2008.

[65] Nicolas Linse, Lorenz Gubler, Günther G Scherer, and Alexander Wokaun. The effect of platinum on carbon corrosion behavior in polymer electrolyte fuel cells. *Electrochimica Acta*, 56(22):7541–7549, 2011.

[66] Jae-Hyun Park, Sung-Dae Yim, Taeyoung Kim, Seok-Hee Park, Young-Gi Yoon, Gu-Gon Park, Tae-Hyun Yang, and Eun-Duck Park. Understanding the mechanism of membrane electrode assembly degradation by carbon corrosion by analyzing the microstructural changes in the cathode catalyst layers and polarization losses in proton exchange membrane fuel cell. *Electrochimica acta*, 83:294–304, 2012.

[67] FN Buchi, M Inaba, and TJ Schmidt. Polymer electrolyte fuel cell durability. 2009.

[68] Hendrik Schulenburg, Bernhard Schwanitz, Nicolas Linse, Gunther G Scherer, Alexander Wokaun, Julijana Krbanjevic, Roman Grothausmann, and Ingo Manke. 3d imaging of catalyst support corrosion in polymer electrolyte fuel cells. *The Journal of Physical Chemistry C*, 115(29):14236–14243, 2011.

[69] C Lim, L Ghassemzadeh, F Van Hove, M Lauritzen, J Kolodziej, GG Wang, S Holdcroft, and E Kjeang. Membrane degradation during combined chemical and me-

chanical accelerated stress testing of polymer electrolyte fuel cells. *Journal of Power Sources*, 257:102–110, 2014.

[70] Soowhan Kim, Byung Ki Ahn, and MM Mench. Physical degradation of membrane electrode assemblies undergoing freeze/thaw cycling: Diffusion media effects. *Journal of Power Sources*, 179(1):140–146, 2008.

[71] Y Matsui, T Suzuki, P Deevanhxay, S Tsushima, and S Hirai. Crack generation in catalyst layer and micro porous layer by wet-dry cycles and its impact on pemfc performance. In *International Conference on Fuel Cell Science, Engineering and Technology*, volume 55522, page V001T01A005. American Society of Mechanical Engineers, 2013.

[72] Miguel A Modestino, Devproshad K Paul, Shudipto Dishari, Stephanie A Petrina, Frances I Allen, Michael A Hickner, Kunal Karan, Rachel A Segalman, and Adam Z Weber. Self-assembly and transport limitations in confined nafion films. *Macromolecules*, 46(3):867–873, 2013.

[73] Yongqiang Li, Jennifer K Quincy, Scott W Case, Michael W Ellis, David A Dillard, Yeh-Hung Lai, Michael K Budinski, and Craig S Gittleman. Characterizing the fracture resistance of proton exchange membranes. *Journal of Power Sources*, 185(1):374–380, 2008.

[74] E Moukheiber, C Bas, and L Flandin. Understanding the formation of pinholes in pfsa membranes with the essential work of fracture (ewf). *international journal of hydrogen energy*, 39(6):2717–2723, 2014.

[75] Ruiliang Jia, Binghong Han, Kemal Levi, Takuya Hasegawa, Jiping Ye, and Reinhold H Dauskardt. Effect of cation contamination and hydrated pressure loading on the mechanical properties of proton exchange membranes. *Journal of Power Sources*, 196(8):3803–3809, 2011.

[76] Ruiliang Jia, Binghong Han, Kemal Levi, Takuya Hasegawa, Jiping Ye, and Reinhold H Dauskardt. Mechanical durability of proton exchange membranes with catalyst platinum dispersion. *Journal of Power Sources*, 196(20):8234–8240, 2011.

[77] Pak Yan Yuen and Reinhold H Dauskardt. Effect of mechanical constraint on tearing energy of polymer membranes. *Macromolecular Materials and Engineering*, 301(9):1096–1103, 2016.

[78] Kshitish Patankar, David A Dillard, Scott W Case, Michael W Ellis, Yongqiang Li, Yeh-Hung Lai, Michael K Budinski, and Craig S Gittleman. Characterizing fracture energy of proton exchange membranes using a knife slit test. *Journal of Polymer Science Part B: Polymer Physics*, 48(3):333–343, 2010.

[79] Ruiliang Jia, Siming Dong, Takuya Hasegawa, Jiping Ye, and Reinhold H Dauskardt. Contamination and moisture absorption effects on the mechanical properties of catalyst coated membranes in pem fuel cells. *international journal of hydrogen energy*, 37(8):6790–6797, 2012.

[80] Jian Zhao, Samaneh Shahgaldi, Xianguo Li, and Zhongsheng Simon Liu. Experimental observations of microstructure changes in the catalyst layers of proton exchange membrane fuel cells under wet-dry cycles. *Journal of the Electrochemical Society*, 165(6):F3337, 2018.

[81] Yafei Chang, Jing Liu, Ruitao Li, Jian Zhao, Yanzhou Qin, Junfeng Zhang, Yan Yin, and Xianguo Li. Effect of humidity and thermal cycling on the catalyst layer structural changes in polymer electrolyte membrane fuel cells. *Energy Conversion and Management*, 189:24–32, 2019.

[82] Roshanak Banan, Aimy Bazylak, and Jean Zu. Effect of mechanical vibrations on damage propagation in polymer electrolyte membrane fuel cells. *International journal of hydrogen energy*, 38(34):14764–14772, 2013.

[83] Roshanak Banan, Aimy Bazylak, and Jean Zu. Combined effects of environmental vibrations and hygrothermal fatigue on mechanical damage in pem fuel cells. *International Journal of Hydrogen Energy*, 40(4):1911–1922, 2015.

[84] R Banan, J Zu, and A Bazylak. Humidity and temperature cycling effects on cracks and delaminations in pemfcs. *Fuel Cells*, 15(2):327–336, 2015.

[85] Guoliang Ding, Michael H Santare, Anette M Karlsson, and Ahmet Kusoglu. Numerical evaluation of crack growth in polymer electrolyte fuel cell membranes based on plastically dissipated energy. *Journal of Power Sources*, 316:114–123, 2016.

[86] Yanzhou Qin, Suhui Ma, Yafei Chang, Yuwen Liu, Yan Yin, Junfeng Zhang, Zhi Liu, Kui Jiao, and Qing Du. Modeling the membrane/cl delamination with the existence of cl crack under rh cycling conditions of pem fuel cell. *International Journal of Hydrogen Energy*, 46(12):8722–8735, 2021.

[87] Yixiang Zhang, Xianguo Li, and Anna Klinkova. Numerical investigation of delamination onset and propagation in catalyst layers of pem fuel cells under hygrothermal cycles. *International Journal of Hydrogen Energy*, 46(19):11071–11083, 2021.

[88] CLY Yeong and Salvatore Torquato. Reconstructing random media. *Physical review E*, 57(1):495, 1998.

[89] David A Coker and Salvatore Torquato. Extraction of morphological quantities from a digitized medium. *Journal of Applied Physics*, 77(12):6087–6099, 1995.

[90] R Byron Bird, Warren E Stewart, and Edwin N Lightfoot. *Transport phenomena*, volume 1. John Wiley & Sons, 2006.

[91] Francis AL Dullien. *Porous media: fluid transport and pore structure*. Academic press, 2012.

[92] MA Ioannidis, MJ Kwiecien, and I Chatzis. Statistical analysis of the porous microstructure as a method for estimating reservoir permeability. *Journal of petroleum science and engineering*, 16(4):251–261, 1996.

[93] Arganthaël Berson, Hae-Won Choi, and Jon G Pharoah. Determination of the effective gas diffusivity of a porous composite medium from the three-dimensional reconstruction of its microstructure. *Physical Review E*, 83(2):026310, 2011.

[94] James G Berryman. Measurement of spatial correlation functions using image processing techniques. *Journal of Applied Physics*, 57(7):2374–2384, 1985.

[95] S Torquato and G Stell. Microstructure of two-phase random media. iii. the n-point matrix probability functions for fully penetrable spheres. *The Journal of chemical physics*, 79(3):1505–1510, 1983.

[96] P Čapek, V Hejtmánek, L Brabec, A Zikánová, and M Kočiřík. Stochastic reconstruction of particulate media using simulated annealing: improving pore connectivity. *Transport in porous media*, 76(2):179–198, 2009.

[97] Gunter Dueck and Tobias Scheuer. Threshold accepting: A general purpose optimization algorithm appearing superior to simulated annealing. *Journal of computational physics*, 90(1):161–175, 1990.

[98] Nicholas Metropolis, Arianna W Rosenbluth, Marshall N Rosenbluth, Augusta H Teller, and Edward Teller. Equation of state calculations by fast computing machines. *The journal of chemical physics*, 21(6):1087–1092, 1953.

[99] D Cule and S Torquato. Generating random media from limited microstructural information via stochastic optimization. *Journal of applied physics*, 86(6):3428–3437, 1999.

[100] Stuart Geman and Donald Geman. Stochastic relaxation, gibbs distributions, and the bayesian restoration of images. *IEEE Transactions on pattern analysis and machine intelligence*, (6):721–741, 1984.

[101] Lester Ingber. Simulated annealing: Practice versus theory. *Mathematical and computer modelling*, 18(11):29–57, 1993.

[102] Ahmed Ouenes and Srinivasa Bhagavan. Application of simulated annealing and other global optimization methods to reservoir description: myths and realities. In *SPE Annual Technical Conference and Exhibition*. OnePetro, 1994.

[103] Patrick Siarry, Gérard Berthiau, François Durdin, and Jacques Haussy. Enhanced simulated annealing for globally minimizing functions of many-continuous variables. *ACM Transactions on Mathematical Software (TOMS)*, 23(2):209–228, 1997.

[104] MS Talukdar, O Torsaeter, MA Ioannidis, and JJ Howard. Stochastic reconstruction of chalk from 2d images. *Transport in porous media*, 48(1):101–123, 2002.

[105] MS Talukdar, O Torsaeter, MA Ioannidis, and JJ Howard. Stochastic reconstruction, 3d characterization and network modeling of chalk. *Journal of Petroleum Science and Engineering*, 35(1-2):1–21, 2002.

[106] Jacob Benesty, Jingdong Chen, Yiteng Huang, and Israel Cohen. Pearson correlation coefficient. In *Noise reduction in speech processing*, pages 1–4. Springer, 2009.

[107] Peter Deuflhard and Andreas Hohmann. *Numerical analysis in modern scientific computing: an introduction*, volume 43. Springer, 2003.

[108] Luke Mizzi, EM Mahdi, Kirill Titov, Ruben Gatt, Daphne Attard, Kenneth E Evans, Joseph N Grima, and Jin-Chong Tan. Mechanical metamaterials with star-shaped pores exhibiting negative and zero poisson's ratio. *Materials & Design*, 146:28–37, 2018.

[109] Hubert Jopek and Tomasz Strek. Thermal and structural dependence of auxetic properties of composite materials. *physica status solidi (b)*, 252(7):1551–1558, 2015.

[110] Luke Mizzi, Daphne Attard, Ruben Gatt, Krzysztof K Dudek, Brian Ellul, and Joseph N Grima. Implementation of periodic boundary conditions for loading of mechanical metamaterials and other complex geometric microstructures using finite element analysis. *Engineering with Computers*, pages 1–15, 2020.

[111] Zihui Xia, Yunfa Zhang, and Fernand Ellyin. A unified periodical boundary conditions for representative volume elements of composites and applications. *International journal of solids and structures*, 40(8):1907–1921, 2003.

[112] Kirt A Page, Ahmet Kusoglu, Christopher M Stafford, Sangcheol Kim, R Joseph Kline, and Adam Z Weber. Confinement-driven increase in ionomer thin-film modulus. *Nano letters*, 14(5):2299–2304, 2014.

[113] Anthony James Merrill Spencer. *Continuum mechanics*. Courier Corporation, 2004.

[114] Ted Belytschko, Wing Kam Liu, Brian Moran, and Khalil Elkhodary. *Nonlinear finite elements for continua and structures*. John wiley & sons, 2013.

[115] Narinder S Khattra, Anette M Karlsson, Michael H Santare, Peter Walsh, and F Colin Busby. Effect of time-dependent material properties on the mechanical behavior of pfsa membranes subjected to humidity cycling. *Journal of Power Sources*, 214:365–376, 2012.

[116] Zongwen Lu, Melissa Lugo, Michael H Santare, Anette M Karlsson, F Colin Busby, and Peter Walsh. An experimental investigation of strain rate, temperature and humidity effects on the mechanical behavior of a perfluorosulfonic acid membrane. *Journal of Power Sources*, 214:130–136, 2012.

[117] Narinder S Khattra, Zongwen Lu, Anette M Karlsson, Michael H Santare, F Colin Busby, and Thomas Schmiedel. Time-dependent mechanical response of a composite pfsa membrane. *Journal of power sources*, 228:256–269, 2013.

[118] Zongwen Lu, Michael H Santare, Anette M Karlsson, F Colin Busby, and Peter Walsh. Time-dependent mechanical behavior of proton exchange membrane fuel cell electrodes. *Journal of Power Sources*, 245:543–552, 2014.

[119] Ahmet Kusoglu, Anette M Karlsson, Michael H Santare, Simon Cleghorn, and William B Johnson. Mechanical response of fuel cell membranes subjected to a hygro-thermal cycle. *Journal of power sources*, 161(2):987–996, 2006.

[120] Piotr Perzyna. Fundamental problems in viscoplasticity. In *Advances in applied mechanics*, volume 9, pages 243–377. Elsevier, 1966.

[121] INC ANSYS. Ansys r19. 2 help (manual). *Ansys corp*, 2015.

[122] Rodney Hill. *The mathematical theory of plasticity*, volume 11. Oxford university press, 1998.

[123] Albert Turon, Carlos G Davila, Pedro Ponces Camanho, and J Costa. An engineering solution for mesh size effects in the simulation of delamination using cohesive zone models. *Engineering fracture mechanics*, 74(10):1665–1682, 2007.

[124] P Naghipour, M Bartsch, and H Voggenreiter. Simulation and experimental validation of mixed mode delamination in multidirectional cf/peek laminates under fatigue loading. *International Journal of Solids and Structures*, 48(6):1070–1081, 2011.

[125] AR Khoei, H Moslemi, and M Sharifi. Three-dimensional cohesive fracture modeling of non-planar crack growth using adaptive fe technique. *International Journal of Solids and Structures*, 49(17):2334–2348, 2012.

[126] Kenneth Langstreth Johnson and Kenneth Langstreth Johnson. *Contact mechanics*. Cambridge university press, 1987.

[127] Roham Solasi, Yue Zou, Xinyu Huang, and Kenneth Reifsnider. A time and hydration dependent viscoplastic model for polyelectrolyte membranes in fuel cells. *Mechanics of Time-Dependent Materials*, 12(1):15–30, 2008.

[128] A Turon, PP Camanho, J Costa, and J Renart. Accurate simulation of delamination growth under mixed-mode loading using cohesive elements: definition of interlaminar strengths and elastic stiffness. *Composite structures*, 92(8):1857–1864, 2010.

[129] MA Crisfield. A faster modified newton-raphson iteration. *Computer methods in applied mechanics and engineering*, 20(3):267–278, 1979.

[130] Mary Kathryn Thompson and John M Thompson. *ANSYS mechanical APDL for finite element analysis*. Butterworth-Heinemann, 2017.

[131] Klaus-Jürgen Bathe, Ekkehard Ramm, and Edward L Wilson. Finite element formulations for large deformation dynamic analysis. *International journal for numerical methods in engineering*, 9(2):353–386, 1975.

[132] Klaus-Jürgen Bathe and Haluk Ozdemir. Elastic-plastic large deformation static and dynamic analysis. *Computers & Structures*, 6(2):81–92, 1976.

[133] Javier Bonet and Richard D Wood. *Nonlinear continuum mechanics for finite element analysis*. Cambridge university press, 1997.

[134] Meredith N Silberstein and Mary C Boyce. Constitutive modeling of the rate, temperature, and hydration dependent deformation response of nafion to monotonic and cyclic loading. *Journal of Power Sources*, 195(17):5692–5706, 2010.

[135] American Society of Mechanical Engineers. Committee on Composite Materials. *Standard test method for mode I interlaminar fracture toughness of unidirectional fiber-reinforced polymer matrix composites*. ASTM International, 2013.

[136] Ted L Anderson and Ted L Anderson. *Fracture mechanics: fundamentals and applications*. CRC press, 2005.

[137] Pucheng Pei, Qianfei Chang, and Tian Tang. A quick evaluating method for automotive fuel cell lifetime. *International Journal of Hydrogen Energy*, 33(14):3829–3836, 2008.

[138] Tatsuhiro Okada, Hiroki Satou, and Makoto Yuasa. Effects of additives on oxygen reduction kinetics at the interface between platinum and perfluorinated ionomer. *Langmuir*, 19(6):2325–2332, 2003.

[139] Ted Belytschko, Wing Kam Liu, Brian Moran, and Khalil Elkhodary. *Nonlinear finite elements for continua and structures*. John wiley & sons, 2014.